Per Arne Slotte, and Carl Fredrik Berg

Department of Geoscience and Petroleum NTNU

Lecture notes in well-testing

Copyright notes:

These present lecture notes are © Per Arne Slotte 2017–2021
and are distributed under the "Creative Commons Attribution-ShareAlike 4.0 International" (CC BY-SA 4.0)
licence: https://creativecommons.org/licenses/by-sa/4.0

Note that the above mentioned license does not apply some of the figures and illustrations; these are marked with the copyright holder.

These notes were typeset using XeTeX version 0.999995
LaTeX class: A modified version of `tufte-book`
Main text font: PT Serif
Title font: PT Sans
`unicode-math` using math font: STIX Two Math
Print date: April 23, 2026

Preface

In June 2016 I was asked to lecture the well testing part of course *TPG4115 Reservoir Property Determination by Core Analysis and Well Testing* given to master students at NTNU. My knowledge of well testing at that point was very limited, as I have had no formal training in reservoir technology, and have mainly been working with reservoir modelling and data integration. Thus, the well known principle of *learning by teaching* did apply, and these notes does, to a certain degree, sum up what I have learnt during the fall-semester 2016.

In previous years students had mainly used the books "T.A. Jelmert: *Introductory well testing*" (bookboon 2013) and "J.W. Lee: *Well Testing*" (Society of Petroleum Engineers 1981) as their main study material. The first of these does not cover all of the material students are expected to learn in the course, and additional material is thus needed. The second covers most of the needed subjects, but it is old and the perspective is to a certain degree outdated. The book has the additional drawback that it uses *oilfield units* and merged numeric conversion factors throughout, which in my view only creates confusion. You can always derive the right numeric factors from an equation given consistent units.

While still mentioning the books of T.A. Jelmert and J.W. Lee as possible material for the students, I decided instead to use the book "*Well test design and analysis*" (PennWell Books 2011) by George Stewart as main reference material. This book covers everything the students are expected to learn, and has a more modern perspective. However, it covers a lot more than needed and it is totally out of the question that students should be required to buy this 1484 page monster. However, students have access to the book in electronic form through the NTNU library, so it was possible to run the course this way.

In order to give the students relevant reading material in a more compact form I decided to create lecture notes that was distributed incrementally. These notes only covered the material that was taught in lectures and homework assignments in the fall-semester 2016, and very little else. There is much to be said about a textbook with such a limited scope, but I believe it is useful for the students to have some extended material (in addition to lecture slides) that actually follow the progression of the lectures. I do, on the other hand, have no actual practical experience in well-testing, neither in operations nor in research, so writing a full-fledged textbook that could accompany the course was out of the question at the time. After the teaching of the well-testing course was taken over by Carl Fredrik Berg in 2017, the notes have been a constant work in progress. The present version is much improved and extended to a large extent due to contributions by Carl Fredrik, and now has a scope similar to other textbooks on the market.

Well testing theory is quite heavy on mathematics compared to what petroleum students tend to be exposed to in other courses. The notation that are used in these notes may also be unfamiliar to some, as derivations and equations for the most part is presented using coordinate free mathematical objects and operators. A chapter with mathematical notes have been included (page 147), and the reader is referred there whenever in doubt about the meaning of an equation.

Trondheim
August 14, 2020
Per Arne Slotte

Contents

1 Introduction 9

1.1 Measuring pressure and rates 11

1.2 Types of tests 12

1.3 Homogeneity and scales 13

1.4 Inverse problem 14

2 Basic theory 15

2.1 The diffusivity equation 15

2.2 Vertical fully penetrating well – Radial flow 18

2.3 Steady state solution 19

3 Drawdown test 25

3.1 Transient solution for drawdown test 25

3.2 Example 28

3.3 Logarithmic approximation 28

3.4 Dimensionless analysis 30

3.5 Permeability and skin 34

3.6 Wellbore storage effect 36

4 Buildup test 39

4.1 Superposition principle 39

4.2 Horner analysis 40

4.3 Example 43

4.4 Miller–Dyes–Hutchinson (MDH) analysis 45

4.5 Example 46

4.6 Slider analysis and desuperposition 47

4.7 Similarity between drawdown and buildup responses 48

5 Finite reservoir 51
5.1 Semi steady state 51
5.2 Example 54
5.3 Exact solution for cylindrical reservoir 55
5.4 Log–log derivative diagnostic plot 56
5.5 Reservoir monitoring with buildup tests 58
5.6 Drainage areas 61
5.7 Reservoir pressure vs. local pressure 62
6 Reservoir boundaries 65
6.1 Well close to a linear boundary 65
6.2 Flow regimes – Diagnostic plots 68
6.3 Channel sands and narrow fault blocks 72
6.4 Leaking boundaries 74
7 Horizontal wells 79
7.1 Flow regimes 79
7.2 Anisotropy 80
7.3 Quantitative analysis 80
7.4 Near well heterogeneities 83
7.5 Well tip effects 84
8 Fractured wells 87
8.1 Laplace transform in well testing 87
8.2 Vertical fractures 89
8.3 Flow periods and flow regimes 89
8.4 Formation radial flow 90
8.5 Formation linear flow 90
8.6 Bilinear flow 92
9 Naturally fractured reservoirs 93
9.1 Dual porosity model 93
9.2 The diffusivity equation for dual porosity 95
9.3 Flow periods 100
9.4 Analyzing a drawdown test 100
9.5 Skin in fractured reservoirs 103
9.6 Validity of model 104
9.7 Final comments 105

10 Gas reservoirs 107
10.1 Pseudo pressure 107
10.2 Analyzing tests using pseudo pressure 109
10.3 Pseudo time 113
11 Multiphase flow 115
11.1 Radial composite 116
11.2 Pseudo pressure and pseudo time 120
12 Numerical methods 123
12.1 Well tests simulators 123
12.2 Parameter estimation 130
12.3 Interference testing 133
13 Deconvolution 137
13.1 Spectral methods 138
13.2 Time domain methods 139
14 The role of well testing in reservoir characterization 143
14.1 Scenarios 143
14.2 Model elements 145
14.3 Measurements 146
14.4 Final words 146
15 Mathematical notes 147
15.1 Scalars, vectors, and tensors 147
15.2 Spatial derivatives and the gradient operator 148
15.3 The Gauss theorem, and the continuity equation 148
15.4 Laplace transform 149
Relevant literature 151
Nomenclature 153
References 157

1
Introduction

The well testing that is the subject matter of the current lectures are a number of methods wherein rates and pressures are manipulated and measured in one or more wells in order to obtain information about the *sub surface reservoir*. Thus it is, in spite of the name, not the well or well production that is tested, but the reservor. Note, however, that the term well test is also used in production technology for tests that actually test the well and the well production, but these tests are not of interest here. Well testing is also known as *pressure transient tests*, which arguably gives a better description of the test.

Well testing is important in many disciplines in addition to petroleum engineering. Examples are groundwater hydrology, geology, waste disposal, and pollution control. The theory and methods are in principle the same in all diciplines, although nomenclature may vary somewhat. In this course we will concentrate on petroleum engineering applications.

The purpose of reservoir characterisation in general is to provide data for describing and modelling the reservoir in order to estimate reserves, forecast future performance, and optimize production. The testing of wells is especially important in exploration when reservoir data is scarce. The data from well test contibute to reserve estimation and are used to determine if reservoirs and reservoir zones are ecomomic. Well testing is also used in reservoir monitoring, by providing average and local reservoir pressure. These pressure data are important input to production optimization, but also contribute indirectly to the reservoir characterization as input to model conditioning (history matching).

In production engineering well testing also contribute by providing data on the state of the near-well reservoir volume. These data are used to answer questions about near-well formation damage, and the need for and the effect of well stimulation treatments.

The basic concept of well testing is described in Fig. 1.1: A signal is sent into the reservoir from the well by changing well production rate or pressure, and the response (pressure/rate change) is measured at the well. The analysis of the response is used to estimate reservoir properties. Since the response is the result of a disturbance that travel away from the well, the early responses are determined by the property in the near well region, while later responses detect more distant

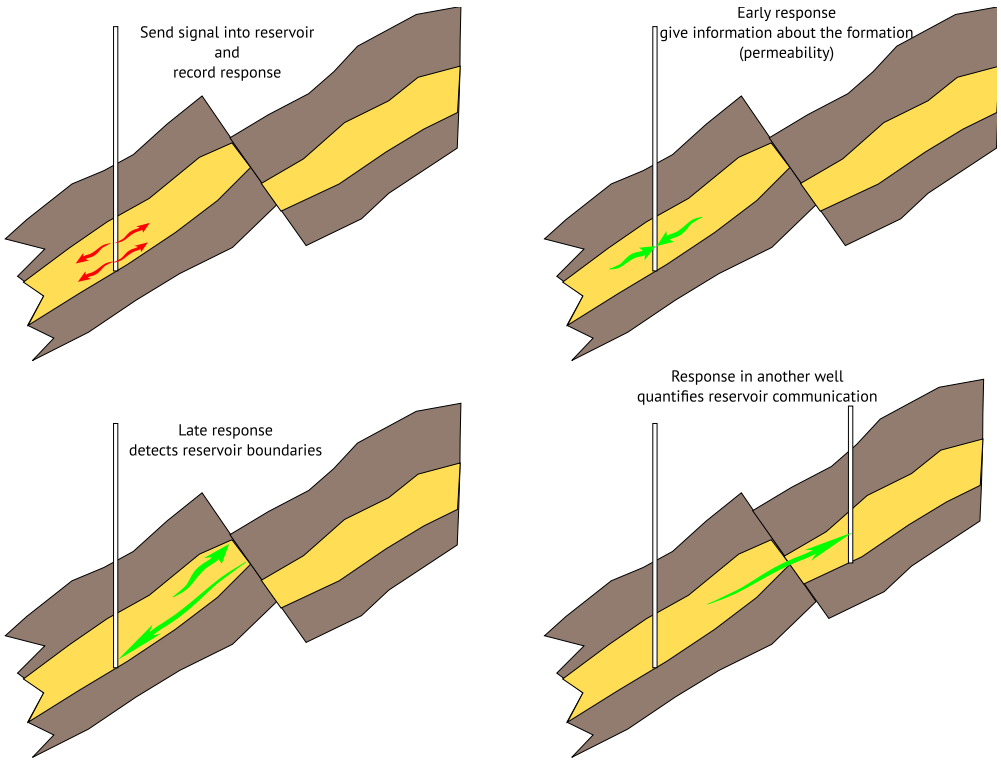


Figure 1.1: The well test concept: A signal is sent into the reservoir, and a response is recorded. Early response give information about the formation, later responses detect reservoir boundaries, and responses in observation wells depend on reservoir communication.

reservoir features. The response may also be recorded in another well in order to investigate reservoir communication, this type of test is called an interference test,

Typical information derived from well tests include permeability, distance to boundaries and faults, size and shape of sand bodies, near wellbore damage or stimulation (Skin), and length of induced fractures. An example of a well test interpretation procedure (Horner analysis, see page 40) used to estimate the permeability of the formation is shown in Fig. 1.2.

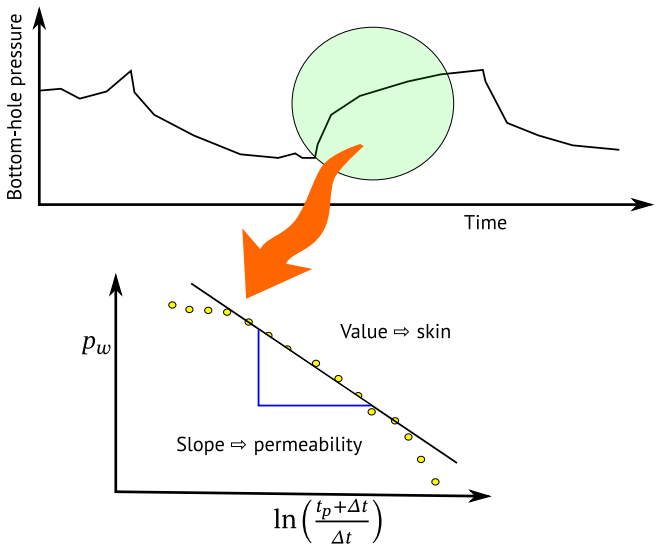


Figure 1.2: Horner analysis, an example of well test interpretation: The bottom hole pressure record from build-up is plotted and used for estimating permeability and skin.

1.1 Measuring pressure and rates

For well testing it is the pressure and the production rate (equivalently, injection rate) that are the most important measured quantities. The pressure measured at the bottom of the well is referred to as the *bottom-hole pressure* (BHP). This is the preferred pressure measurement, as it is closest to the formation. Using the wellhead pressure involves back-calculating the BHP based on a well flow model, and this typically introduces too much uncertainty to be reliable for well test analysis.

In modern wells, the pressure sensor is typically connected to the surface by cable. This enables continuous (~every second) surface readout of the BHP. When several reservoir zones are produced at different bottom hole pressures, it is common to have a pressure transducer in each zone. It is also common with pressure sensors both inside the tubing and in the annulus.



Figure 1.3: The cable connections from two down-hole gauges coming out of the Christmas tree.

The pressure sensor is normally placed at the top of the perforated zone, thus a hydrostatic correction is required to obtain the reservoir pressure at different heights in the reservoir (e.g. the depth at the middle of the perforation). Transient pressure tests utilize the relative change in pressure, thus a constant correction factor will not influence the well test analysis. However, if the fluids between the pressure sensor and the height of interest is changing, this will influence the hydrostatic correction. As an example, consider a gas-liquid interface slowly moving up the tubing. This could severely influence the pressure readings, and thereby the well test analysis.

Earlier pressure gauges included mechanical gauges (based on changes in strain of a metal due to pressure changes, e.g. a Bourdon gauge) and strain gauges (based on the change in resistance of an conductor due to pressure changes). While mechanical gauges might be preferred for extreme well conditions, present-day pressure gauges are mostly quartz gauges. A quartz gauge employs that the resonant frequency of a quartz crystal changes with pressure. As the resonant frequency is sensitive to temperature in addition to pressure, it is common to run two quartz pressure gauges in parallel. Only one of them is exposed to the surrounding pressure, while both are exposed to the temperature. The temperature is measured by the gauge solely exposed to temperature, and this temperature is used to correct the pressure reading from the gauge exposed to pressure.

The flow rate is controlled either at surface or down-hole. For surface control it is important to distinguish the flow rates observed at the surface from the flow rates experienced by the reservoir downhole. Typical flow gauges are turbines, Coriolis meters and multiphase flow meters applying gamma ray attenuation at different energy levels. In general, rate measurements has much lower quality than pressure measurements.

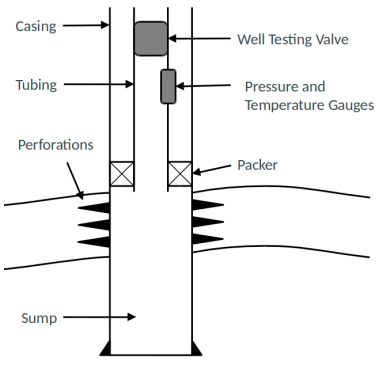


Figure 1.4: A schematic of the placement of down hole pressure gauge and flow gauge.

1.2 Types of tests

The main classes of well tests are drawdown test, buildup test, and interference test. In addition we have injection tests and falloff tests, which are the equivalents of drawdown and buildup tests for injectors. The Dill Stem Test (DST), is a special drawdown test that is often performed in exploration wells and newly drilled wells.

Drawdown test

In a drawdown test, a static, stable and shut-in well is opened to flow. For traditional analysis, the flow rate should be constant. Typical objectives for a drawdown test are to obtain an average permeability (k) of the drainage area, to estimate the skin (S), to obtain pore volume of the reservoir, and to detect reservoir heterogeneity.

Buildup test

During a buildup test, a well which is already flowing (ideally constant rate) is shut in, and the downhole pressure is measured as the pressure builds up. The objectives includes obtaining average permeability k and skin S, as with the drawdown test. In addition, the buildup test is conducted to obtain initial reservoir pressure during the transient state (p_i), and to obtain the average reservoir pressure ($\overline{p}$) over the drainage area during pseudo-steady state.

Injection test

In an injection test, a static, stable and shut-in well is opened to (water-)injection. Thus, an injection test is conceptually similar to a drawdown test, except flow is into the well rather than out of it. In most cases the objectives of the injection test is the same as those of a production test (e.g. k,S), but the test can also be used to map the injected water.

Falloff test

For a pressure falloff test, a well already injection (ideally at at a constant rate) is shut in, and the pressure drop during the falloff period is measured as the pressure declines. Thus, the pressure falloff test is similar to the pressure buildup test. A pressure falloff test is usually proceeded by an injectivity test of a long duration.

1.2.1 Obtained properties and time

Due to the transient nature of a pressure front moving through the reservoir, the different classes of obtained reservoir properties are intrinsically linked to the time after the change in well rates. The different reservoir properties are organized according to time in Table 1.1.

Early time	Middle time	Late time
Near wellbore	Reservoir	Reservoir boundaries
Skin	Permeability	Reservoir volume
Wellbore storage	Heterogeneity	Faults
Fractures	Dual porosity	(sealing/non-sealing)
	Dual permeability	Boundary pressure

Table 1.1: Time of measurement versus type of measurements

1.2.2 Other well tests

Interference test

In an interference test, one well is produced (rate change) and pressure (response) is observed in a different well. The main objective of an interference test is to investigate reservoir communication and continuity, including communication over faults and barriers.

Drill stem test

The specialised drill stem test (DST) is commonly used to test a newly drilled well. The well is opened to flow by a valve at the base of the test tool, and reservoir fluid flows up the drill string. Analysis of the DST requires special techniques, since the flow rate is not constant as the fluid rises in the drill string. This is a severe example of a wellbore storage effect (see page 36).

1.3 Homogeneity and scales

All reservoir modelling assumes that the sub surface can be described in terms of model elements.[1] Each element have homogenous (constant) or slowly varying properties, a characteristic size and shape, and a corresponding length scale, or representative elementary volume (REV), over whitch property variations are averaged. Well testing provides data for determining the properties of these model elements. The relation between reservoir characterisatin and geological reservoir modelling is discussed in the corresponding chapter on pages 143–147.

[1] Mark Bentley Philip Ringrose. *Reservoir Model Design. A Practitioner's Guide*. Springer, 2015. DOI: 10.1007/978-94-007-5497-3.

Model elements are three-dimensional rock bodies which are petrophysically and/or geometrically distinct from each other in the specific context of the reservoir fluid system.

In general each measurement type probes a certain reservoir volume, and is associated with a corresponding measurement scale. Some measurement types and their corresponding scales (depth of investigation) are shown in Table 1.2. The investigation scales may or may

Measurement type	Approximate length scale (m)
Core	0.1
Well log	0.5
DST/RFT	1–10
Well test	0.1–500
Production data	100–1000

Table 1.2: Some measurement types and their corresponding measurement length scales

not correspond to geological modeling scales, that is representative elementary volumes of model elements. In contrast to most other methods, a well test does not probe properties at a fixed length scale: The early time part of the test probe small scale properties near the well, and later part of the test probe larger scale properties further away from the well. Note also that, apart from the production data itself, well testing is the only mesurement type that supply data on the scales that are directly relevant for reservoir simulation.

1.4 Inverse problem

It should be noted that well test interpretation in isolation is actually an *ill-posed* inverse problem [2]. Well testing tries to describe an unknown system by matching parameters in a model to measurement. The model parameters hopefully correspond to a reality in the subsurface, but the solution is generally non-unique both in terms of model and model parameters. Severe simplifications/assumptions are often made to obtain a unique solution, and a requirement for any useful well test analysis is that it is consistent with realistic geological concepts for the reservoir at hand.

[2] An inverse problem starts with the results and then calculates the causes. A well-posed problem has an unique solution that changes continuously with the initial conditions.

2
Basic theory

In this chapter we will derive the linear hydraulic diffusivity equation, which is *the* fundamental equation in well test analysis. There are a number of important approximations and assumptions involved when deriving this equation. These assumptions includes that flow is isothermal and single phase, permeability is isotropic and independent of pressure, the fluid viscosity and compressibility is pressure independent, the fluid compressibility is low, and that the well is completed across the full formation thickness.

2.1 The diffusivity equation

The starting point for deriving the diffusivity equation is is the continuity equation for single phase flow which is an expression of conservation of mass in a volume element: [1]

"mass in" – "mass out" = "change in mass"

$$-\nabla \cdot (\rho q) = \frac{\partial}{\partial t}(\phi \rho) \quad . \tag{2.1}$$

Here ρ is the fluid density, ϕ is the porosity, and q is the volumetric fluid flux[2]. The volumetric flux is related to the gradient in pore pressure via Darcys law:

$$q = -\frac{k}{\mu}\nabla p \tag{2.2}$$

Inserting (2.2) into (2.1), and assuming constant permeability, k, and pressure independent viscosity, μ, we get

$$\frac{k}{\mu}\nabla \cdot (\rho \nabla p) = \frac{\partial}{\partial t}(\phi \rho) \quad . \tag{2.3}$$

We may expand the derivatives of the product on both sides of Eq. (2.3), which gives:

$$\frac{k}{\mu}\left(\nabla \rho \cdot \nabla p + \rho \nabla^2 p\right) = \rho \frac{\partial}{\partial t}\phi + \phi \frac{\partial}{\partial t}\rho \quad . \tag{2.4}$$

We will first investigate the left hand side of Eq. (2.4): Compressibility c is a measure of the relative volume change as a response to a pressure change:

$$c = -\frac{1}{V}\frac{\partial V}{\partial p}, \tag{2.5}$$

[1] For a general introduction to the mathematical notation, see the mathematical notes at page 147. The nabla symbol ∇ represents the del operator $\nabla = \left(\frac{\partial}{\partial x}, \frac{\partial}{\partial y}, \frac{\partial}{\partial z}\right)$. The Gauss theorem, which is used in the derivation of the continuity equation (2.1) is discussed on page 148.

[2] Volumetric flux has the dimension of a velocity, and is often called Darcy velocity. Note that the Darcy velocity is always lower than the (interstitial) velocity of the fluid flowing through the pores.

where V is the volume, and the liquid compressibility may be used to convert derivatives of density into derivatives of pressure. For a liquid the density $\rho = m/V_l$ is the fraction of mass m divided by the volume of the liquid V_l. Rewriting, we also have $V_l = m/\rho$. We can then derive the liquid compressibility c_l as:

Liquid compressibility: $c_l = \frac{1}{\rho}\frac{\partial \rho}{\partial p}$.

$$c_l = -\frac{1}{V_l}\frac{\partial V_l}{\partial p} = -\frac{\rho}{m}\frac{\partial m/\rho}{\partial \rho}\frac{\partial \rho}{\partial p} = -\rho\frac{-1}{\rho^2}\frac{\partial \rho}{\partial p} = \frac{1}{\rho}\frac{\partial \rho}{\partial p}. \tag{2.6}$$

Thus, we see that the first term on the left hand side of Eq. (2.4) is

$$\nabla\rho\cdot\nabla p = \frac{\partial \rho}{\partial p}\nabla p\cdot\nabla p = \rho c_l|\nabla p|^2 \propto c_l \quad , \tag{2.7}$$

and since this term is proportional to the compressibility it may be ignored in the low compressibility limit. The left hand side of Eq. (2.4) is then simply

Low compressibility limit: $c_l \to 0$

$$\rho\frac{k}{\mu}\nabla^2 p \quad . \tag{2.8}$$

The right hand side of Eq. (2.4) can be expressed in terms of the time derivative of pressure by applying the chain rule,

$$\begin{aligned}\rho\frac{\partial}{\partial t}\phi + \phi\frac{\partial}{\partial t}\rho &= \rho\frac{\partial \phi}{\partial p}\frac{\partial}{\partial t}p + \phi\frac{\partial \rho}{\partial p}\frac{\partial}{\partial t}p \\ &= \rho\phi\left(\frac{1}{\phi}\frac{\partial \phi}{\partial p} + \frac{1}{\rho}\frac{\partial \rho}{\partial p}\right)\frac{\partial}{\partial t}p\end{aligned} \quad . \tag{2.9}$$

The formation compressibility, c_ϕ, is defined[3] as

Formation compressibility: $c_\phi = \frac{1}{\phi}\frac{\partial \phi}{\partial p}$

$$c_\phi = \frac{1}{\phi}\frac{\partial \phi}{\partial p} \quad , \tag{2.10}$$

[3] It is left to the reader to show, assuming that the sand grains themselves are incompressible, that the formation compressibility as defined here is also equal to the compressibility of a porous rock sample with total volume V subject to an increased pore pressure: $c_\phi = \frac{1}{V}\frac{\partial V}{\partial p}$.

and

$$c_t = c_l + c_\phi \quad . \tag{2.11}$$

is called total compressibility, so Eq. (2.9) is simply

Total compressibility: $c_t = c_l + c_\phi$

$$\rho\frac{\partial}{\partial t}\phi + \phi\frac{\partial}{\partial t}\rho = \rho\phi c_t\frac{\partial}{\partial t}p \quad . \tag{2.12}$$

Equating left (2.8) and right hand side (2.12), and dividing by $\rho\phi c_t$ we get

$$\frac{k}{\mu\phi c_t}\nabla^2 p = \frac{\partial}{\partial t}p \quad . \tag{2.13}$$

This is the (hydraulic) diffusivity equation which is *the* fundamental equation in well testing, and the quantity

$$\boxed{\eta = \frac{k}{\mu\phi c_t}} \tag{2.14}$$

Hydraulic diffusivity

is called the (hydraulic) diffusivity. The unit for hydraulic diffusivity η is

$$[\eta] = \frac{[k]}{[\mu][\phi][c_t]} = \frac{m^2}{(Pa\cdot s)(Pa^{-1})} = \frac{m^2}{s} \quad , \tag{2.15}$$

where we use that porosity ϕ is dimensionless. Using the η notation for the diffusivity, we get the following simplified diffusivity equation:

$$\boxed{\eta\nabla^2 p = \frac{\partial}{\partial t}p} \quad . \tag{2.16}$$

The (hydraulic) diffusivity equation

The diffusivity η determines how fast pressure signals move through the reservoir, but it is important to note that the signal moves in a diffusion process, where the actual speed decreases as it spreads. This is very different from a seismic pressure wave which move at constant velocity.

By investigating the different elements of the diffusivity η in Eq. (2.14), we observe that a pressure disturbance moves faster in a high permeable reservoir than in a low permeable reservoir. On the other hand, increased porosity, viscosity or compressibility reduces the speed of the pressure signal.

2.1.1 Diffusivity equation in oil reservoirs

The diffusivity equation (2.13) was derived under the following assumptions:

- Isothermal flow
- A single fluid phase
- Constant isotropic permeability
- Fluid viscosity independent of pressure
- Compressibility independent of pressure
- Low fluid compressibility

As derived, the equation is thus only valid for reservoirs that contain a single low-compressible fluid phase, that is for water reservoirs. However, the validity of the equation may be extended to oil reservoirs at irreducible water saturation, S_{wi}. The irreducible water does not flow, but it influences the total compressibility, so the diffusivity equation is valid for oil reservoirs at S_{wi} provided the following:

[4] The oil permeability at irreducible water saturation S_{wi} is typically very close to the absolute permeability, $k_o \simeq k$, and can thus be interchanged.

- Permeability, k, is replaced by oil permeability[4], $k_o = k_{ro}(S_{wi})k$.
- Viscosity, μ, is the oil viscosity, μ_o
- Total compressibility is defined as:
  $c_t = c_\phi + S_o c_o + S_w c_w$

In this case the equation takes the form

$$\frac{k_o}{\mu_o \phi c_t} \nabla^2 p = \frac{\partial}{\partial t} p \tag{2.17}$$

Gas reservoirs, which may contain a highly compressible fluid, and reservoirs with several flowing fluids, can not be analyzed based on the simple hydraulic diffusivity equation. Well test analysis in these reservoirs will be discussed in separate chapters (see page 107 and 115)

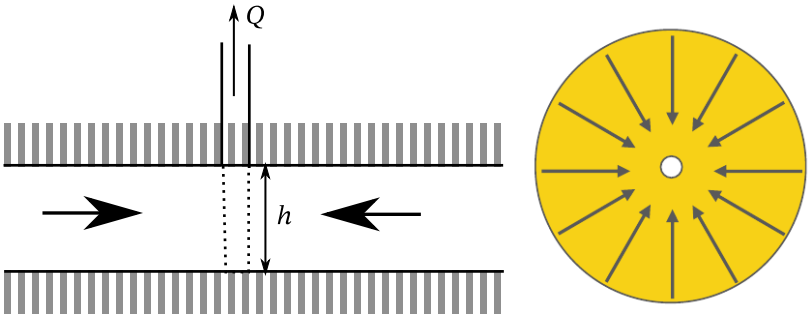


Figure 2.1: Vertical fully penetrating well in a reservoir of constant thickness

2.2 Vertical fully penetrating well – Radial flow

We will consider a vertical fully penetrating well in a reservoir of constant thickness, as illustrated in Fig. 2.1. In this case it is natural to use cylinder coordinates.

The general form of the Laplace operator on the pressure field $\nabla^2 p$ in cylinder coordinates is

$$\nabla^2 p = \left[\frac{1}{r}\frac{\partial}{\partial r}\left(r\frac{\partial}{\partial r}\right) + \frac{1}{r^2}\frac{\partial^2}{\partial\theta^2} + \frac{\partial^2}{\partial z^2}\right] p \quad , \tag{2.18}$$

where r is the radius, θ is the angle, and z is the height. For a fully penetrating well in an isotropic medium flow is independent of angle and height so that we have $\frac{\partial p}{\partial \theta} = 0$ and $\frac{\partial p}{\partial z} = 0$. The diffusivity equation (2.16) is then

The radial diffusivity equation. That is the diffusivity equation for a vertical fully penetrating well in cylinder coordinates

$$\boxed{\eta\frac{1}{r}\frac{\partial}{\partial r}\left(r\frac{\partial p}{\partial r}\right) = \frac{\partial p}{\partial t}} \quad . \tag{2.19}$$

Alternatively, it is illustrative to derive the radial diffusivity equation (2.19) starting from the radial form of the continuity equation (2.1):

$$-\frac{\partial}{\partial r}(A\rho q) = \frac{\partial}{\partial t}(A\rho\phi) \quad , \tag{2.20}$$

where $A = 2\pi rh$ is the cylinder area. Employing Darcy's law (2.2), we obtain

$$\frac{\partial}{\partial r}\left(2\pi rh\rho\frac{k}{\mu}\frac{\partial p}{\partial r}\right) = \frac{\partial}{\partial t}(2\pi rh\rho\phi) \tag{2.21}$$

$$\frac{k}{r\mu}\frac{\partial}{\partial r}\left(r\rho\frac{\partial p}{\partial r}\right) = \frac{\partial}{\partial t}(\rho\phi) \quad , \tag{2.22}$$

where we have used that k, μ, and h are constants. From Eq. (2.12) we have

$$\frac{\partial}{\partial t}(\rho\phi) = \rho\phi c_t\frac{\partial p}{\partial t} \quad . \tag{2.23}$$

For the left hand side we obtain

$$\frac{\partial}{\partial r}\left(r\rho\frac{\partial p}{\partial r}\right) = \rho\frac{\partial}{\partial r}\left(r\frac{\partial p}{\partial r}\right) + r\frac{\partial p}{\partial r}\frac{\partial\rho}{\partial r} = \rho\frac{\partial}{\partial r}\left(r\frac{\partial p}{\partial r}\right) + r\frac{\partial p}{\partial r}\frac{\partial\rho}{\partial p}\frac{\partial p}{\partial r} \tag{2.24}$$

$$= \rho\frac{\partial}{\partial r}\left(r\frac{\partial p}{\partial r}\right) + r\left(\frac{\partial p}{\partial r}\right)^2 c_l\rho \simeq \rho\frac{\partial}{\partial r}\left(r\frac{\partial p}{\partial r}\right) \quad . \tag{2.25}$$

Here we used Eq. (2.6) for the third equality, and applied the low compressibility limit (small liquid compressibility c_l) for the last similarity. Combining these results, we get the equation for radial flow:

$$\eta \frac{1}{r}\frac{\partial}{\partial r}\left(r\frac{\partial p}{\partial r}\right) = \frac{\partial p}{\partial t} \quad . \tag{2.26}$$

2.2.1 Flow regimes

At different times in a well test the solution of the diffusivity will be in one of three possible stages of flow regimes:

Initially we have a general unsteady state, or transient, flow situation where pressure change differently with time dependent on position:

Transient flow

$$\frac{\partial}{\partial t}p(r,t) = f(r,t) \tag{2.27}$$

Analysis of the transient flow period is the main concern of well testing.

Very late in the test the reservoir reaches a semi steady state where the pressure profile is constant and pressure changes at the same rate everywhere[5]:

Semi steady state flow

$$\frac{\partial}{\partial t}p(r,t) = C \tag{2.28}$$

[5] In some contexts the term pseudo steady state is used for semi steady state flow.

Analysis of the time to reach semi steady state and the rate of pressure change in this period give information about the reservoir shape, area, and volume.

In the case that the reservoir pressure is supported by a strong aquifer, or by pressure maintenance operations (water or gas injection), pseudo steady state is replaced by true steady state flow:

Steady state flow

$$\frac{\partial}{\partial t}p(r,t) = 0 \quad . \tag{2.29}$$

2.3 Steady state solution

We will first investigate the steady state solution of radial flow (2.19). Except for early times in a well test, this solution describes the pressure profile around a vertical fully penetrating well. Steady state means that the right hand side of is zero, so the steady state pressure profile can be found by solving

$$\frac{\partial}{\partial r}\left(r\frac{\partial}{\partial r}p\right) = 0 \quad . \tag{2.30}$$

We may integrate Eq. (2.30) and get

$$\frac{\partial}{\partial r}p = C_1\frac{1}{r} \quad , \tag{2.31}$$

where C_1 is an integration constant. Furthermore, using integration by substitution to integrate both sides from the well radius r_w to r, we get

$$p - p_w = C_1 \ln\left(\frac{r}{r_w}\right) \quad . \tag{2.32}$$

where p_w is the well pressure.

Darcys law tells us that the volumetric flux is proportional to the pressure gradient:

$$q = -\frac{k}{\mu}\nabla p \quad . \tag{2.33}$$

The volumetric fluid flux, q, is defined as volumetric rate per area, so given the total *down hole (reservoir) well production rate* [6], Q, we have

$$q = \frac{Q}{2\pi r h} \quad , \tag{2.34}$$

where h is the perforation height (which in our case equals the height of the reservoir). The integration constant is determined by inserting the flux from Eq. (2.34) and the pressure derivative, $\nabla p = \frac{1}{r}C_1$, from Eq. (2.31) into Darcys law (2.33):

$$C_1 = \frac{Q\mu}{2\pi k h} \quad , \tag{2.35}$$

which when inserted into Eq. (2.32) gives the general steady state solution for radial flow:

$$\boxed{p = p_w + \frac{Q\mu}{2\pi k h}\ln\left(\frac{r}{r_w}\right)} \quad . \tag{2.36}$$

[6] In well testing literature it is most common to derive equations in terms of surface rates. In the present text all equations are derived using down hole (reservoir) rates. The apparent only difference between the two approaches is that Q here is replaced by $Q_s B$, where B is the formation volume factor and Q_s is the surface well production rate, in those other texts. However, representing the relation between a reservoir rate and a surface rate, which involves for instance equipment such as test separators, in general by a simple constant factor B underplays the non-triviality of the conversion.

The integration constant is determined by production rate via Darcys law

General steady state solution for radial flow

We will now discuss some of the characteristics of the solution (2.36). First observe that $p(r_w) = p_w$, since $\ln(1) = 0$. The pressure changes fast close to the well and very slowly at larger distances. This means that most of the pressure drop from the reservoir into the well is located in the near well region, and any changes in the permeability in this region will have a significant influence on well productivity. In general, the difference in pressure (pressure drop) from r_1 to r_2 is given by

$$p(r_1) - p(r_2) = \frac{Q\mu}{2\pi k h}\ln\left(\frac{r_1}{r_2}\right) \quad . \tag{2.37}$$

The pressure profile, $p(r) - p_w$, scales with the logarithm of r by a characteristic pressure p_c:

Characteristic pressure scale

$$p_c = \frac{Q\mu}{2\pi k h} \quad . \tag{2.38}$$

Note that p_c is proportional to the rate and inversely proportional to permeability.

2.3.1 Skin

The formation volume close to the wellbore typically has altered properties compared to the surrounding reservoir. Of highest importance for well productivity is an altered permeability, and the effect of this alteration on productivity is called skin.

Skin is typically caused by formation damage as a result of drilling and production, but can also be the result of reduced mobility due multiphase flow. Intentional improved permeability due to well treatments and hydraulic fracturing also contribute to skin, but the positive results of these treatments result in a negative skin in contrast

Skin is typically caused by formation damage.

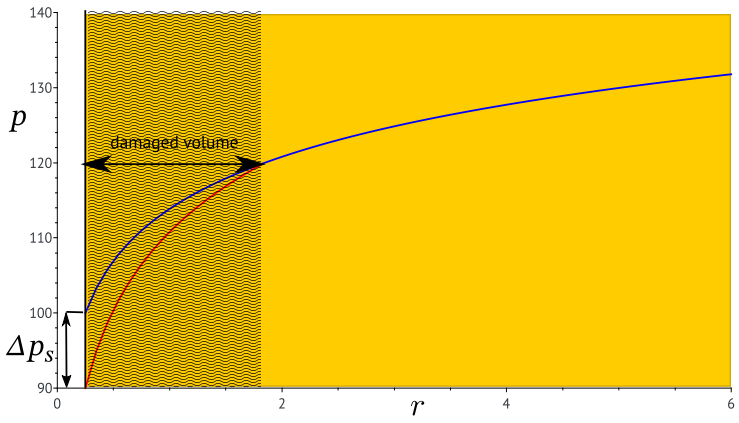


Figure 2.2: Pressure profile around a well with skin. Actual pressure profile in red, ideal profile without skin in blue.

to the normal positive skin due to formation damage. Flow restrictions in the wellbore itself including scale buildup, wax, and asphaltene deposits are not referred to as formation damage, but are quite often included as part of the skin. Examples of factors that contribute to skin are given below:

- Formation damage due to drilling
  - Solids plugging from mud filtrate invasion
  - Clay-particle swelling or dispersion
  - Emulsion blockage
- Formation damage due to production
  - Fines migration
  - Deposition of paraffins or asphaltenes
  - Deposition of scale minerals
- Reduced mobility due to phase behavior
  - Condensate banking (Production below dewpoint)
  - Free gas (Production below bubble point)

As shown in Fig. 2.2, the effect of the skin is an additional pressure drop compared to a well without skin. The effect can be described quantitatively by the dimensionless skin factor, S

Skin factor, S.

$$\boxed{\Delta p_s = \frac{Q\mu}{2\pi kh} S = p_c S} \quad , \tag{2.39}$$

and adding the extra pressure drop to the steady state solution (2.36) gives

Note: $p_c = \frac{Q\mu}{2\pi kh}$

$$\boxed{p = p_w + p_c \left[\ln\left(\frac{r}{r_w}\right) + S \right]} \quad . \tag{2.40}$$

Typically skin factors $S > 5$ are considered bad and factors $S < -3.5$ are viewed as excellent.

The effect of skin can alternatively be described in terms of the equivalent (or effective) wellbore radius, r_{we}. The concept is illustrated in Fig. 2.3: The additional pressure drop due to skin can be

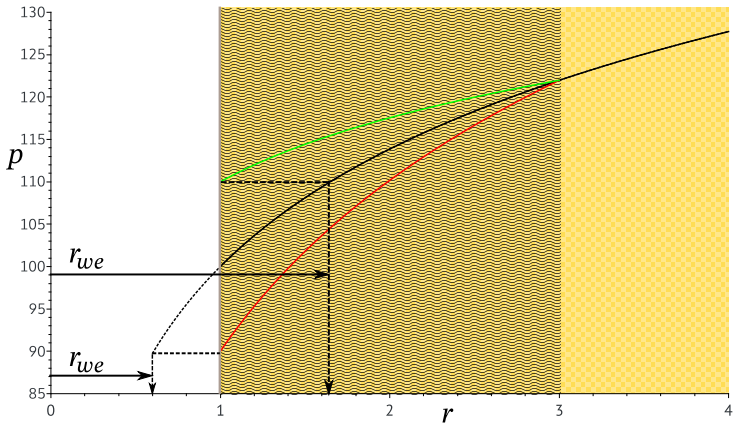


Figure 2.3: The concept of effective wellbore radius: The red curve shows the pressure profile with a positive skin (formation damage), corresponding to a reduced effective wellbore radius. The green curve shows the pressure profile with negative skin, corresponding to an increased effective radius. The radius is scaled by the well radius r_w.

expressed in terms of the effective wellbore radius by noting that the ideal pressure profile is

$$p_{\text{ideal}}(r) = p_w + \Delta p_s + p_c \ln\left(\frac{r}{r_w}\right) \quad , \tag{2.41}$$

and that by definition we have

$$p_{\text{ideal}}(r_{we}) = p_w \quad . \tag{2.42}$$

Effective wellbore radius, r_{we}.

The extra pressure drop due to skin is then found by combining equations (2.41) and (2.42):

$$\Delta p_s = p_c \ln\left(\frac{r_w}{r_{we}}\right) \tag{2.43}$$

By comparing equations (2.39) and (2.43) we see that the equivalent wellbore radius can be expressed in terms of the skin factor:

$$\boxed{r_{we} = r_w e^{-S}} \quad . \tag{2.44}$$

2.3.2 Productivity index

The productivity index, PI, is a measure of well productivity, and is conceptually defined through [7]

$$Q_s = \text{PI} \cdot (p_r - p_w) \quad , \tag{2.45}$$

[7] The pressure difference $(p_r - p_w)$ is the driving force, and is called *drawdown*. Note that the definition of the productivity index vary in the literature, and some text alternatively define PI based on the pressure at the outer boundary or the reservoir.

where Q_s is the *surface* production rate, and p_r is the reservoir pressure. Since the the pressure is not constant throughout the reservoir, Eq. (2.45) does not uniquely define *PI* as it depends on how and where the reservoir pressure is defined. For steady state, and semi steady state flow, the productivity index will be constant if the reservoir pressure is identified as the *average* reservoir pressure, so a natural choice is

$$p_r = \overline{p} = \frac{1}{V}\int p(x,y,z)\,dxdydz \quad , \tag{2.46}$$

where V is the reservoir volume

Equivalent radius

We define the *equivalent radius*, r_e, as the radius where the reservoir

pressure equals the average reservoir pressure, $p(r_e) = \overline{p}$. Inserting this into Eq. (2.40), and solving for the production rate gives

$$Q = \frac{2\pi kh}{\mu\left(\ln\left(\frac{r_e}{r_w}\right) + S\right)}\left(\overline{p} - p_w\right) \quad . \tag{2.47}$$

Thus, production is proportional to the difference between reservoir pressure and well pressure, and introducing the formation volume factor

$$B = Q/Q_s \tag{2.48}$$

we have

$$\boxed{\mathrm{PI} = \frac{2\pi kh}{\mu B}\frac{1}{\ln\left(\frac{r_e}{r_w}\right) + S}} \quad . \tag{2.49}$$

As would be expected, we see that long wells, with a large radius and small skin, in a high permeability formation, have high productivity.

For transient non-steady state flow, the equivalent radius increase with time, corresponding to a decline in productivity, while for steady and semi steady state flow r_e, and consequently PI, is constant. To get a measure for how r_e depend on reservoir size, we will investigate the semi steady state solution for a finite circular reservoir with an outer radius r_o. This will also allow us to quantify the relative importance of skin on productivity.

Get average pressure by integrating the pressure profile.

The average reservoir pressure $\overline{p}$ is given by the integral

$$\overline{p} = \frac{1}{\pi r_o^2}\int_{r_w}^{r_o} 2\pi r p(r)\, dr = p_w + p_c S + \frac{2p_c}{r_o^2}\int_{r_w}^{r_o} r\ln\left(\frac{r}{r_w}\right) dr \quad , \tag{2.50}$$

that is

$$\overline{p} = p_w + p_c\left(\ln\left(\frac{r_o}{r_w}\right) - \frac{1}{2} + S\right) \quad , \tag{2.51}$$

where we have ignored the small terms proportional to $\left(\frac{r_w}{r_o}\right)^2$ that originate from the lower integration limit. Comparing equations (2.51) and (2.40) we see that

$$\ln\left(\frac{r_e}{r_w}\right) = \ln\left(\frac{r_o}{r_w}\right) - \frac{1}{2} \quad , \tag{2.52}$$

or

$$r_e = e^{-\frac{1}{2}} r_o \approx 0.6 r_o \quad . \tag{2.53}$$

We can insert (2.52) into (2.49) to get

$$\mathrm{PI} = \frac{2\pi kh}{\mu B}\frac{1}{\ln\left(\frac{r_o}{r_w}\right) - \frac{1}{2} + S} \quad , \tag{2.54}$$

and we see that we may ignore the effect of skin on productivity when

$$|S| \ll \ln\left(\frac{r_o}{r_w}\right) - \frac{1}{2} \quad . \tag{2.55}$$

As an example; if we have $r_o = 500\,\mathrm{m}$ and $r_w = 0.1\,\mathrm{m}$, we get

$$\ln\left(\frac{r_o}{r_w}\right) - \frac{1}{2} \approx 8 \quad ,$$

which can also be compared to the criterion for bad skin ($S > 5$) mentioned on page 21.

3
Drawdown test

In a drawdown test a non-producing well is opened for production at an ideally constant rate, and the flowing bottom hole pressure is recorded. An ideal drawdown rate schedule, with corresponding pressure response, is shown in Fig. 3.1.

In this chapter, a special case of the solution to the diffusivity equation will be derived. This solution, known as the *infinitely acting line source fundamental solution,* is directly relevant for analyzing a drawdown test, and the inspection of this solution gives important insight into how pressure signals move in the reservoir. Further, we will show how a drawdown test can be used to derive reservoir and well properties such as permeability and skin factor.

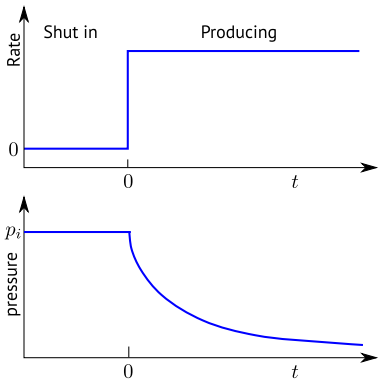


Figure 3.1: The ideal drawdown schedule.

3.1 Transient solution for drawdown test

In this section we will derive a solution to the transient behavior of a drawdown test in an infinite reservoir. Since this solution is not influenced by any boundaries it is called an infinite acting solution. In the derivation we will treat the well as a line source, i.e. we will ignore any effects due to the finite well radius. The infinite acting line-source solution is the most fundamental solution in well testing. and the analysis of the spatial and temporal behavior of this solution gives valuable insights. The line source solution is accurate for distances far away from the well at all times, but is not accurate for the well pressure at short times. At the end of this subsection we will compare well pressures from the approximate solution to the exact finite wellbore solution to establish its range of validity.

The diffusivity equation in cylinder coordinates was given by Eq. (2.19). Using the product rule for differentiation, we can write out Eq. (2.19) as

$$\frac{1}{r}\frac{\partial}{\partial r}\left(r\frac{\partial p}{\partial r}\right) = \frac{1}{r}\frac{\partial}{\partial r}p + \frac{\partial^2}{\partial r^2}p = \frac{1}{\eta}\frac{\partial}{\partial t}p \quad , \tag{3.1}$$

Note: $\eta = \frac{k}{\mu\phi c_t}$ (hydraulic diffusivity).

and rearranging the terms, this gives the following equation:

$$\left[\frac{1}{r}\frac{\partial}{\partial r} + \frac{\partial^2}{\partial r^2} - \frac{1}{\eta}\frac{\partial}{\partial t}\right]p = 0 \quad . \tag{3.2}$$

We are searching the transient solution for a constant rate drawdown test in an infinite reservoir. This solution will also be valid for the

early times of a test in a finite reservoir, i.e. for times shorter than the time needed for the pressure signal to travel to the outer (nearest) boundary. We will assume a line source, which means that we will take the inner constant flow boundary condition at $r = 0$ and not at r_w. This is equivalent to the correct boundary condition as long as we consider large distances. Since a semi steady state pressure profile is established in the near well area after a relatively short time, the line source solution will also be valid for times larger than a characteristic time, and the skin effect will amount to an additional constant pressure drop, Δp_s, except for short times.

The source at the well is approximated by a line source.

In order to derive the solution we will assume that it has a special form and then proceed to show that this form satisfies the differential equation and the boundary conditions. The assumption is that the solution is on the form

$$p(r,t) = p\left(\frac{r^2}{4\eta t}\right) = p(\xi) \quad . \tag{3.3}$$

As the hydraulic diffusivity η has unit m^2/s, we see that ξ is a dimensionless variable. We will now perform a change of variable from r and t to $\xi = r^2/(4\eta t)$ in the diffusivity equation (3.2). Observing that

$$\begin{aligned}
\frac{\partial \xi}{\partial r} &= \frac{\partial}{\partial r}\left(\frac{r^2}{4\eta t}\right) = \frac{2r}{4\eta t} &&= \frac{2\xi}{r} \\
\frac{\partial^2 \xi}{\partial r^2} &= \frac{\partial^2}{\partial r^2}\left(\frac{r^2}{4\eta t}\right) = \frac{2}{4\eta t} &&= \frac{2\xi}{r^2} \quad , \\
\frac{\partial \xi}{\partial t} &= \frac{\partial}{\partial t}\left(\frac{r^2}{4\eta t}\right) = -\frac{r^2}{4\eta t^2} &&= -\frac{\xi}{t}
\end{aligned} \tag{3.4}$$

we get the following equalities:

$$\begin{aligned}
\frac{1}{r}\frac{\partial}{\partial r} &= \frac{1}{r}\frac{\partial \xi}{\partial r}\frac{\partial}{\partial \xi} &&= \frac{2\xi}{r^2}\frac{\partial}{\partial \xi} \\
\frac{\partial^2}{\partial r^2} &= \frac{\partial^2 \xi}{\partial r^2}\frac{\partial}{\partial \xi} + \left(\frac{\partial \xi}{\partial r}\right)^2 \frac{\partial^2}{\partial \xi^2} &&= \frac{2\xi}{r^2}\frac{\partial}{\partial \xi} + \left(\frac{2\xi}{r}\right)^2 \frac{\partial^2}{\partial \xi^2} \quad . \\
-\frac{1}{\eta}\frac{\partial}{\partial t} &= -\frac{1}{\eta}\frac{\partial \xi}{\partial t}\frac{\partial}{\partial \xi} = \frac{\xi}{t\eta}\frac{\partial}{\partial \xi} &&= \frac{4\xi^2}{r^2}\frac{\partial}{\partial \xi}
\end{aligned} \tag{3.5}$$

Collecting these terms, the diffusivity equation (3.2) has the form

$$\left[\left(\frac{4\xi}{r^2} + \frac{4\xi^2}{r^2}\right)\frac{\partial}{\partial \xi} + \frac{4\xi^2}{r^2}\frac{\partial^2}{\partial \xi^2}\right] p = 0 \quad , \tag{3.6}$$

which can be simplified to

$$\left[(1+\xi)\frac{\partial}{\partial \xi} + \xi\frac{\partial^2}{\partial \xi^2}\right] p = 0 \quad . \tag{3.7}$$

Since (3.7) is an equation of ξ only, the assumed form $\xi = r^2/(4\eta t)$ is a possible solution.

Given this form of ξ, a boundary condition at $r = 0$ (line source) corresponds to an inner boundary condition at $\xi = 0$. We also have a specified initial pressure in the whole reservoir and a constant pressure at infinity,

$$p(r,0) = p(\infty,t) = p_i \quad , \tag{3.8}$$

where the constant pressure at infinity corresponds to an outer boundary condition at $\xi = \infty$.

It can be shown, by back substitution, that the solution to Eq. (3.7) has the form

$$p(\xi) = A + BX(\xi) \quad , \tag{3.9}$$

where $X(\xi)$ is a function that satisfy the condition

$$\frac{\partial X}{\partial \xi} = -\frac{e^{-\xi}}{\xi} \quad , \tag{3.10}$$

and A and B are constants to be determined by the boundary conditions. The function

$$X(\xi) = \mathrm{E}_1(\xi) = \int_\xi^\infty \frac{e^{-t}}{t} dt \tag{3.11}$$

is an exponential integral, which is tabulated and available as a special function in math packages.[1] Since

$$\int_\xi^\infty \frac{e^{-t}}{t} dt = \int_\infty^\xi -\frac{e^{-t}}{t} dt \quad , \tag{3.12}$$

we can apply the first fundamental theorem of calculus to obtain Eq. (3.10).

The exponential integral function $\mathrm{E}_1(\xi)$ is plotted in Fig. 3.2. The plot indicates that $\mathrm{E}_1(\infty) = 0$, which we will use to determine the constant A: Since $X(\infty) = \mathrm{E}_1(\infty) = 0$, the outer boundary condition $p(\infty) = p_i$ implies

$$A = p_i \quad , \tag{3.13}$$

so $p(\xi) = p_i + BX(\xi)$. The inner boundary condition is used to determine the constant B. We first note that

$$\frac{\partial p}{\partial \xi} = \frac{\partial}{\partial \xi}\left(p_i + BX(\xi)\right) = B\frac{\partial X}{\partial \xi} = -B\frac{e^{-\xi}}{\xi} \quad . \tag{3.14}$$

A constant total rate Q at $r = 0$ then translates to a condition on the pressure gradient via Darcys law:

$$\begin{aligned} \frac{Q}{2\pi r h} = q &= \frac{k}{\mu}\frac{\partial p}{\partial r} \\ &= \frac{k}{\mu}\frac{\partial p}{\partial \xi}\frac{\partial \xi}{\partial r} \\ &= -\frac{k}{\mu}B\frac{e^{-\xi}}{\xi}\frac{\partial \xi}{\partial r} \\ &= -\frac{k}{\mu}B\frac{2}{r}e^{-\xi} \end{aligned} \tag{3.15}$$

In the last equality we invoke the first equality in Eq. (3.4). The inner boundary condition is at $\xi = 0$, so Eq. (3.15) gives

$$B = -\frac{Q\mu}{4\pi k h} \quad . \tag{3.16}$$

Substituting the integration constants from Eqs. (3.13) and (3.16) into Eq. (3.9) gives the final expression for the infinite acting line

[1] The exponential integral $\mathrm{E}_1(x)$ is available as `expint` in Matlab, `scipy.special.exp1(x)` in Python, and `Ei(1,x)` in Maple.
Note that traditionally the function

$$\mathrm{Ei}(\xi) = -\int_{-\xi}^{\infty} \frac{e^{-t}}{t} dt$$

is used in well testing literature. Using this function we have

$$X(\xi) = -\mathrm{Ei}(-\xi) \quad ,$$

which gives gives a rather awkward notation. The two functions give identical results for positive real values of ξ, so tabulated values for $-\mathrm{Ei}(-\xi)$ found in the literature may be used for $\mathrm{E}_1(\xi)$.

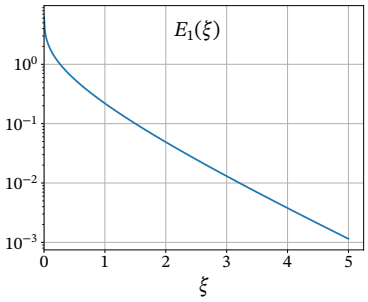


Figure 3.2: The exponential integral

source solution for a constant rate drawdown test:

$$\boxed{p = p_i - \frac{Q\mu}{4\pi kh}\,\mathrm{E}_1\left(\frac{\mu\phi c_t}{4k}\frac{r^2}{t}\right)} \quad . \tag{3.17}$$

Infinite acting line source solution.

Using the η notation for hydraulic diffusivity and p_c for the characteristic pressure, this equation simplifies to:

$$p = p_i - \frac{1}{2}p_c\,\mathrm{E}_1\left(\frac{1}{4\eta}\frac{r^2}{t}\right) \quad . \tag{3.18}$$

After a small example, we will investigate some of the properties of this solution.

3.2 Example

We will employ Eq. (3.17) using the reservoir data in Table 3.1. In Fig. 3.3 we have plotted Eq. (3.17) after 1 to 4 days. As we see from the left figure, the first days witness a large change in the pressure profile, while the subsequent days yields subsequently smaller changes from the previous day. We also observe that the pressure profile at a radius of 1000 m begins to significantly deviate from the initial pressure after approximately 4 days. Thus, if the distance from the well to the nearest reservoir boundary is 1000 m the infinite acting solution will be invalid after 4 days.

In the right figure we have plotted the same graphs in a logarithmic plot. This plot shows clearly that the change in the pressure profile diminish with time. It also indicates that the pressure profile is close to linear when plotted on a logarithmic scale. This will be investigated further in the next section.

	SPE Metric	SI
k	0.1 mD	9.869×10^{-14} m^2
h	10 m	10 m
Q	100 m^3/d	1.16×10^{-3} m^3/s
r_w	0.12 m	0.12 m
μ	1 cP	1×10^{-3} Pa s
ϕ	0.2	0.2
c_t	1×10^{-4} bar^{-1}	1×10^{-9} Pa^{-1}
p_i	200 bar	2×10^7 Pa

Table 3.1: Basic data for example.

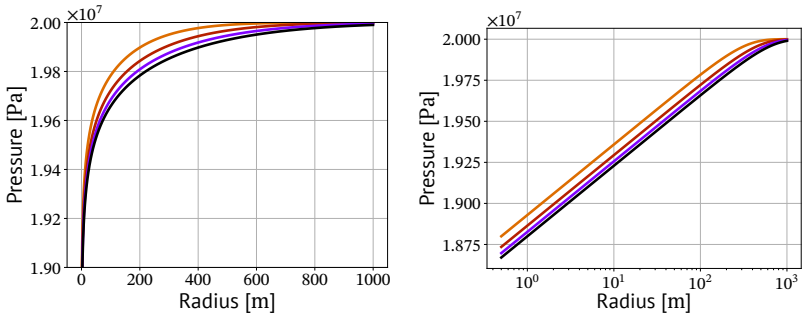


Figure 3.3: Vertical fully penetrating well in a reservoir of constant thickness. Pressure profile after 1, 2, 3, and 4 days.

3.3 Logarithmic approximation

The exponential integral $\mathrm{E}_1(\xi)$ has a logarithmic singularity at $\xi = 0$, and for small ξ it can be approximated by a logarithm:

$$\mathrm{E}_1(\xi) \approx \ln\left(\frac{1}{\xi}\right) - \gamma \quad , \tag{3.19}$$

where $\gamma = 0.5772\ldots$ is the Euler(–Mascheroni) constant.

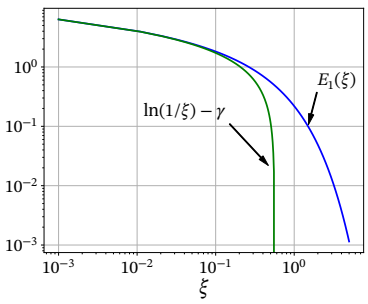


Figure 3.4: A plot comparing the exponential integral $\mathrm{E}_1(\xi)$ in blue and $\ln(1/\xi) - \gamma$ in green.

A comparison between $\mathrm{E}_1(\xi)$ and $\ln(1/\xi) - \gamma$ is shown in Fig. 3.4. In this plot, the functions are similar for values smaller than $10^{-2} = 0.01$. This indicates that the logarithmic approximation is fair for

$$\frac{1}{4\eta}\frac{r^2}{t} < 0.01 \quad , \tag{3.20}$$

thus the approximation is fair for small radii r and late times t.

Employing the approximation given by Eq. (3.19) we obtain

$$\boxed{p(r,t) = p_i - \frac{p_c}{2}\left(\ln\left(4\eta\frac{t}{r^2}\right) - \gamma\right)} \quad . \tag{3.21}$$

The exponantial integral is replaced by the logarithmic approximation for small ξ (large t or small r)

By subtracting the pressure given by Eq. (3.21) at two different distances, r_1 and r_2 we see that

$$p(r_1) - p(r_2) = p_c \ln\left(\frac{r_1}{r_2}\right) \quad . \tag{3.22}$$

independent of time. This is identical to the expression for steady state (2.37), which means that a logarithmic semi steady state pressure profile has developed around the well.

The exponential integral is exponentially small for large values of ξ, and we have the approximation:

$$\mathrm{E}_1(\xi) \approx \frac{e^{-\xi}}{\xi} \quad . \tag{3.23}$$

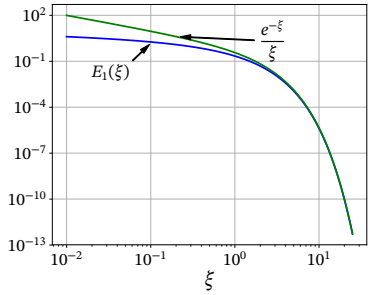


Figure 3.5: A plot comparing the exponential integral $\mathrm{E}_1(\xi)$ in blue and $e^{-\xi}/\xi$ in green.

Fig. 3.5 is a comparison between $\mathrm{E}_1(\xi)$ and $e^{-\xi}/\xi$, and this plot shows that the functions are similar for values larger than 10. As $\mathrm{E}_1(\xi) \simeq 0$ for large values of ξ, the pressure is undisturbed ($p = p_i$) at large distances or short times.

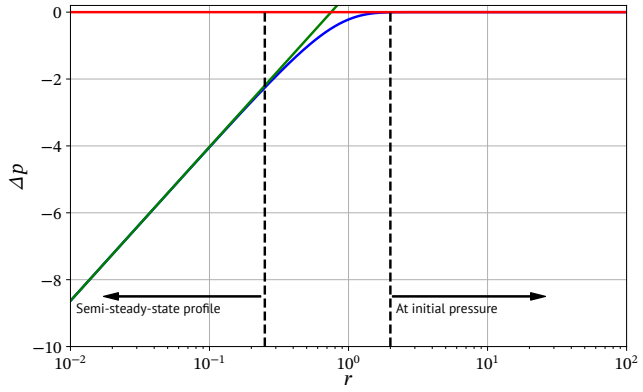


Figure 3.6: Pressure profile at a fixed time (blue line). A logarithmic semi steady state pressure profile has developed around the well, and pressure beyond a certain distance is essentially unchanged. (In this figure Δp is given in units of $\frac{Q\mu}{4\pi kh}$, and r is given in units of $\sqrt{\frac{\mu\phi c_t}{4kt}}$)

The pressure profile at a fixed time is illustrated in Fig. 3.6. For small distances the pressure profile is matched by the logarithmic approximated given by Eq. (3.21). For large distances the pressure is essentially unchanged and still at initial pressure.

The time–space dependency of the pressure is given by $\mathrm{E}_1(\xi)$, shown in Fig. 3.7. We see that the pressure is essentially unchanged ($\mathrm{E}_1(\xi) < 0.01$) wherever $\xi > 3$, which corresponds to a distance $r > r_p$:

$$r_p = \sqrt{12\eta t} \quad . \tag{3.24}$$

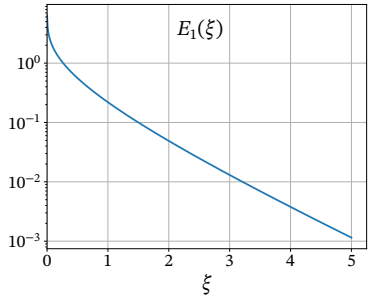


Figure 3.7: The exponential integral

The speed at which the pressure front is moving, v_p, is given by

$$v_p = \frac{dr_p}{dt} = \sqrt{\frac{3\eta}{t}} \quad , \tag{3.25}$$

The speed of the pressure front is diverging at early times, and is diminishing as the front moves away from the well. As mentioned earlier the line source solution is not valid for early times close to the wellbore, so the divergence at $t \to 0$ is unproblematic.

In addition to the location of the pressure front (Eq. (3.24)), we are interested in the radius within which the pressure is *significantly influenced* by the test. This radius is called radius of investigation, r_{inv}, and is somewhat arbitrarily defined as the radius where $\xi = 1$:

Radius of investigation

$$\boxed{r_{\text{inv}} = \sqrt{4\eta t}} \quad . \tag{3.26}$$

Eq. (3.26) can be inverted in order to determine the time needed to investigate reservoir features at a given distance from the well:

$$t_{\text{inv}} = \frac{r_{\text{inv}}^2}{4\eta} \quad . \tag{3.27}$$

3.3.1 Well pressure

The primary measurement in a well test is the bottom hole well pressure. The line source solution is not valid at the well radius for short times, but for late times we can get the well pressure by inserting the well radius in Eq. (3.21). Additionally, the effect of skin must be accounted for. Since a steady state pressure profile develops in the near well area, the skin effect amounts to an additional constant pressure drop Δp_s except for very short times. From the steady state solution (2.39) we have

$$\Delta p_s = p_c S \quad , \tag{3.28}$$

which gives

$$\boxed{p_w(t) = p_i - \frac{p_c}{2}\left(\ln\left(4\eta\frac{t}{r_w^2}\right) - \gamma + 2S\right)} \quad . \tag{3.29}$$

3.4 Dimensionless analysis

Dimensionless variables simplify our equations by embodying well and reservoir parameters that are assumed constant, e.g. well radius, permeability, viscosity, porosity, compressibility, perforation height etc. Using dimensionless variables then yields solutions that are independent of such well and reservoir parameters, which enables comparisons of pressure behavior from different wells. Additionally, dimensionless variables yields solution that are independent of the unit system.

We have already seen that the infinitely acting solution is characterized by the dimensionless group

$$\xi = \frac{r^2}{4\eta t} \quad . \tag{3.30}$$

The diffusivity equation itself can also be expressed on dimensionless form using dimensionless variables for space, time, and pressure. Dimensionless variables are variables measured in terms of a characteristic scale for that variable. In the well testing context the characteristic length is the well radius r_w with corresponding dimensionless radius

In well testing, the well radius is a characteristic length.

$$r_D = \frac{r}{r_w} \quad . \tag{3.31}$$

We introduce a similar dimensionless time variable $t_D = t/t_c$, where t_c is a characteristic time. Using a general direction $x_D = x/r_w$, we have the following equality's:

$$\begin{aligned} \frac{\partial}{\partial x} &= \frac{\partial x_D}{\partial x}\frac{\partial}{\partial x_D} = \frac{1}{r_w}\frac{\partial}{\partial x_D} \\ \frac{\partial}{\partial t} &= \frac{\partial t_D}{\partial t}\frac{\partial}{\partial t_D} = \frac{1}{t_c}\frac{\partial}{\partial t_D} \end{aligned} \quad . \tag{3.32}$$

If we use the dimensionless space variables into the diffusivity equation (2.16),

$$\eta\nabla^2 p = \frac{\partial}{\partial t}p \quad , \tag{3.33}$$

we obtain

$$\eta\frac{1}{r_w^2}\nabla_D^2 p = \frac{1}{t_c}\frac{\partial}{\partial t_D}p \quad , \tag{3.34}$$

where ∇_D use derivation with respect to the dimensionless variable (e.g. $\frac{\partial}{\partial x_D}$). From Eq. (3.34) we see that the diffusivity equation can be written on a simple form, the dimensionless diffusivity equation:

$$\nabla_D^2 p = \frac{\partial}{\partial t_D}p \quad , \tag{3.35}$$

The characteristic time is defined such that the dimensionless diffusivity equation has a simple form.

if the characteristic time is defined as

$$t_c = \frac{r_w^2}{\eta} \quad . \tag{3.36}$$

From Eq. (2.15) we have that the unit for the hydraulic diffusivity is m^2/s, thus we observer that t_D is actually dimensionless.

We see from the general steady state solution for radial flow (2.36), that the characteristic scale for pressure is

$$p_c = \frac{Q\mu}{2\pi kh} \quad , \tag{3.37}$$

and we may also use use the initial reservoir pressure, p_i, as a datum pressure. The dimensionless pressure is then

Dimensionless pressure is measured relative to a datum pressure p_i.

$$p_D = \frac{p_i - p}{p_c} = (p_i - p)\frac{2\pi kh}{Q\mu} \quad . \tag{3.38}$$

Note that the derivative of the dimensionless pressure and the true pressure have opposite sign.

Summing up Eqs. (3.31)), (3.36), and (3.38), we have the following dimensionless variables:

$$\boxed{r_D = \frac{r}{r_w} \qquad t_D = \frac{\eta}{r_w^2}t \qquad p_D = \frac{p_i - p}{p_c}} \quad . \tag{3.39}$$

These are the dimensionless variables most commonly used in the well testing context.

The general steady state solution for radial flow (2.36),

$$p = p_w + p_c \ln\left(\frac{r}{r_w}\right) \quad , \tag{3.40}$$

can be rearranged as:

$$\frac{p_i - p}{p_c} = \frac{p_i - p_w}{p_c} - \ln\left(\frac{r}{r_w}\right) \quad . \tag{3.41}$$

Substituting with dimensionless variables, we then obtain the dimensionless form of the general steady state solution for radial flow:

$$\boxed{p_D = p_{Dw} + \ln(r_D)} \quad . \tag{3.42}$$

To translate equations with partial derivatives into the dimensionless variables given above, we need to replace the partial derivatives with their dimensionless versions:

$$\frac{\partial r_D}{\partial r} = \frac{1}{r_w} \qquad \frac{\partial t_D}{\partial t} = \frac{\eta}{r_w^2} \qquad \frac{\partial p}{\partial p_D} = -p_c \quad . \tag{3.43}$$

From the diffusivity equation using dimensionless radius and time (3.35), we can change of variable to dimensionless pressure:

$$\begin{aligned} \nabla_D^2 p &= \frac{\partial p}{\partial t_D} \\ \nabla_D \cdot \frac{\partial p}{\partial p_D} \nabla_D p_D &= \frac{\partial p}{\partial p_D} \frac{\partial p_D}{\partial t_D} \\ \nabla_D \cdot (-p_c) \nabla_D p_D &= -p_c \frac{\partial p_D}{\partial t_D} \quad . \end{aligned} \tag{3.44}$$

By dividing out the (scalar) characteristic pressure on both sides, we obtain the dimensionless diffusivity equation as

$$\boxed{\nabla_D^2 p_D = \frac{\partial}{\partial t_D} p_D} \quad . \tag{3.45}$$

Substituting Eq. (3.44) into the diffusivity equation in cylindrical coordinates we obtain

$$\begin{aligned} \frac{\eta}{r} \frac{\partial}{\partial r}\left(r \frac{\partial p}{\partial r}\right) &= \frac{\partial}{\partial t} p \\ \frac{\eta}{r} \frac{\partial r_D}{\partial r} \frac{\partial}{\partial r_D}\left(r \frac{\partial p}{\partial p_D} \frac{\partial r_D}{\partial r} \frac{\partial p_D}{\partial r_D}\right) &= \frac{\partial p}{\partial p_D} \frac{\partial t_D}{\partial t} \frac{\partial p_D}{\partial t_D} \\ \frac{\eta}{r} \frac{1}{r_w} \frac{\partial}{\partial r_D}\left(r(-p_c) \frac{1}{r_w} \frac{\partial p_D}{\partial r_D}\right) &= -p_c \frac{\eta}{r_w^2} \frac{\partial p_D}{\partial t_D} \quad . \end{aligned} \tag{3.46}$$

By rearranging this equation, we obtain the dimensionless diffusivity equation with cylindrical coordinates:

$$\boxed{\frac{1}{r_D} \frac{\partial}{\partial r_D}\left(r_D \frac{\partial p_D}{\partial r_D}\right) = \frac{\partial p_D}{\partial t_D}} \quad . \tag{3.47}$$

Similarly, the infinite acting line source solution for the pressure in the reservoir (3.17) is:

$$\boxed{p_D(r_D, t_D) = \frac{1}{2} \mathrm{E}_1\left(\frac{r_D^2}{4 t_D}\right)} \quad , \tag{3.48}$$

and the logarithmic approximation for well pressure in the infinitely acting drawdown test (3.29) is

$$\boxed{p_{Dw}(t_D) = \frac{1}{2}\left(\ln\left(4t_D\right) - \gamma + 2S\right)} \quad . \tag{3.49}$$

Note that dimensionless variables are not unique, and the ones defined in Eq. (3.39) are not the only set used even in the context of well testing. When setting up the characteristic dimensionless equations for detecting the distance to a sealing fault it is for instance more natural to use the distance to the fault as a characteristic length than the well radius.

3.4.1 Validity of equations for well pressure

The logarithmic expression for the well pressure given by Eq. (3.49) is only valid for times longer than some characteristic time, dependent on the wellbore radius, r_w. The error has two sources: first, the logarithm is an approximation to the exponential integral, $\mathrm{E}_1(\cdot)$, and second, the constant rate boundary condition is incorrectly placed at $r = 0$ instead of at the sand face, $r = r_w$. We will show below that the requirement that the effect of these two approximations shall be negligible essentially lead to the same criterion for selecting the characteristic time.

The exact infinite acting solution (with the constant rate boundary condition at $r = r_w$) for the pressure in the well is[2]

$$p_{Dw}(t_D) = \frac{2}{\pi^2}\int_0^\infty \frac{1-\exp(-u^2 t_D)}{u^2\left(\mathrm{J}_1(u)^2 + \mathrm{Y}_1(u)^2\right)}du \quad , \tag{3.50}$$

where $J_1(\cdot)$ and $Y_1(\cdot)$ are Bessel functions[3].

In Fig. 3.8 we have plotted the infinite acting solution for well pressure (3.48) (red line), together with the expressions logarithmic approximation (3.49) (blue line), and the exact solution (3.50).

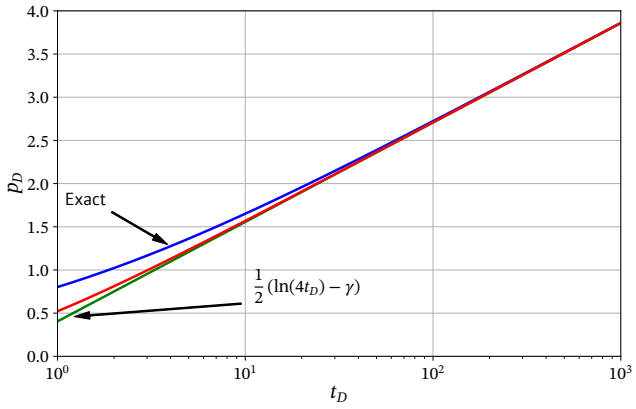


Figure 3.8: Comparing the exact solution for well pressure (blue line) with the line source solution (red line) and the logarithmic approximation (green line). p_D and t_D are dimensionless pressure and time as defined in Eq. (3.39).

The infinite acting solution for well pressure (3.48) is accurate within 1% for

$$\boxed{t_D > 100} \quad , \tag{3.51}$$

[2] A. F. Van Everdingen and W. Hurst. "The Application of the Laplace Transformation to Flow Problems in Reservoirs." In: *Petroleum Transactions, AIME* (Dec. 1949), pp. 305–324. DOI: 10.2118/949305-G.

[3] The integral in Eq. (3.50) is well behaved and can be evaluated using a standard integration routine in most math packages. It should be noted, however, that a the more general expression for $r > r_w$ that appear in A. F. Van Everdingen and W. Hurst is not that well behaved.

which corresponds to

$$t > 100 \cdot \frac{r_w^2}{\eta} \quad . \tag{3.52}$$

This is reflected in the plot in Fig. 3.8. This validity range is in good agreement with the validity range obtained for the logarithmic approximation (3.20), which for $r = r_w$ gives

$$t > 100 \cdot \frac{r_w^2}{4\eta} \quad , \tag{3.53}$$

which corresponds to

$$t_D > 25 \quad . \tag{3.54}$$

We observe from the plots in Fig. 3.8 that the validity range for the logarithmic approximation is in fair agreement with the validity range of the infinite acting solution.

Note that the early time behavior is also influenced by skin and wellbore-effects, and it will be shown (see page 38) that the so called wellbore storage effect in most cases last for times longer that the time defined by Eq. (3.52).

Having determined the lower time limit for the validity of Eq. (3.29), we now turn to the upper time for its validity. The well pressure behaves as if the reservoir were infinite as long as the pressure signal is not yet reflected back from the outer (nearest) boundary. Let the distance to the outer boundary be r_o, then the *reflected pressure change* must travel $2r_o$ to influence pressures near the wellbore. The time–space dependency of the pressure is given by $\mathrm{E}_1(\xi)$, and the infinite acting solution is valid to within 1% as long as $\mathrm{E}_1(\xi(2r_o)) < 0.01$, that is for $\xi > 4$ or

Validity of infinite acting solution

$$\boxed{t < \frac{r_o^2}{4\eta}} \tag{3.55}$$

Eq. (3.49) is valid (eqs. (3.52) and (3.55)) for dimensionless times

$$\boxed{100 < t_D < \frac{r_{Do}^2}{4}} \quad , \tag{3.56}$$

where r_{Do} is the dimensionless distance to the outer boundary.

3.5 Permeability and skin

In this section we will describe how the reservoir permeability and the skin factor of the well can be found by analyzing the well test data.

The pressure response in an ideal drawdown test was derived in the previous section (Eq. (3.29));

$$p_w(t) = p_i - \frac{p_c}{2}\left(\ln\left(\frac{4\eta t}{r_w^2}\right) - \gamma + 2S\right) \quad . \tag{3.57}$$

Rearranging this equation and writing out the characteristic pressure $p_c = Q\mu/(2\pi kh)$, we get

$$\begin{aligned} p_w(t) &= -\frac{Q\mu}{4\pi kh}\ln(t) + \left[p_i - \frac{Q\mu}{4\pi kh}\left(\ln\left(\frac{4\eta}{r_w^2}\right) - \gamma + 2S\right)\right] \\ &= m\ln(t) + C \quad , \end{aligned} \tag{3.58}$$

where $m = -Q\mu/(4\pi kh)$ and C are constants independent of time. We see from Eq. (3.58) that if we plot the well pressure as a function of $\ln(t)$ (semilog plot), we should see a straight line with slope m.

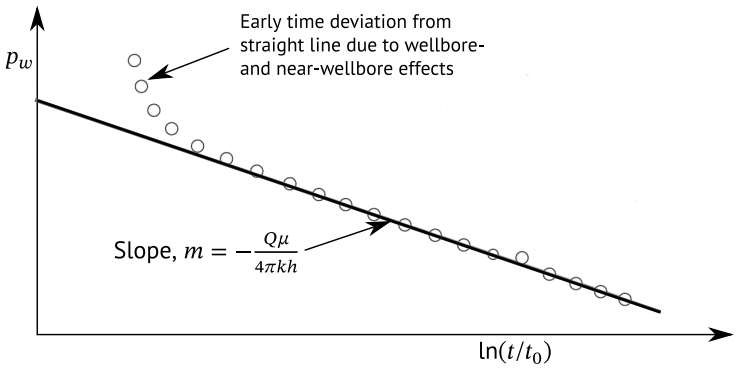


Figure 3.9: Semilog plot of a drawdown test

The early part of the data will deviate from the straight line due to wellbore and near wellbore effects, and the late time part of the data will deviate due to the effect of boundaries or large scale heterogeneities, but permeability and skin may be estimated using Eq.(3.57) based on the part of the data that fall on a straight line.

Permeability may be estimated based on the slope, of the line, m. As illustrated in Fig. 3.9:

$$\boxed{k = -\frac{Q\mu}{4\pi h}\frac{1}{m}} \quad . \tag{3.59}$$

Once the permeability is known, the skin can be estimated from the fitted straight line intercept or value on the straight line at any other point in time t_s:

$$\boxed{S = \frac{1}{2}\left(\frac{p(t_s) - p_i}{m} - \ln\left(\frac{4\eta t_s}{r_w^2}\right) + \gamma\right)} \quad . \tag{3.60}$$

3.5.1 Example

We will go through an example to illustrate the procedure. Basic data for the well test are given in Table 3.2.

A semilog plot of the data are shown in Fig. 3.10. The time between 0.1 and 10 h can be fitted to a straight line. Based on the slope, m, of this line, the permeability can be estimated using Eq. (3.59). We have

$$\frac{Q\mu}{4\pi h} = 9.23 \times 10^{-9}\ \mathrm{m^2/Pa} \tag{3.61}$$

Ideally we should estimate the slope by fitting all points in the linear interval to a straight line (linear regression), but we may also estimate the slope by using the endpoints of interval:

$$\begin{aligned} m &= \frac{\Delta p}{\Delta \ln(t)} = \frac{p(t_1) - p(t_2)}{\ln\left(\frac{t_1}{t_2}\right)} \\ &= -\frac{8.66 \times 10^6 - 8.24 \times 10^6}{\ln(100)}\mathrm{Pa}^{-1} \\ &= 9.12 \times 10^4\ \mathrm{Pa}^{-1} \end{aligned} \tag{3.62}$$

	SPE Metric	SI
h	10 m	10 m
Q	100 m^3/d	1.16×10^{-3} m^3/s
r_w	0.12 m	0.12 m
μ	1 cP	1×10^{-3} Pa s
ϕ	0.2	0.2
c_t	1×10^{-4} bar^{-1}	1×10^{-9} Pa^{-1}

Table 3.2: Basic data for the example well test.

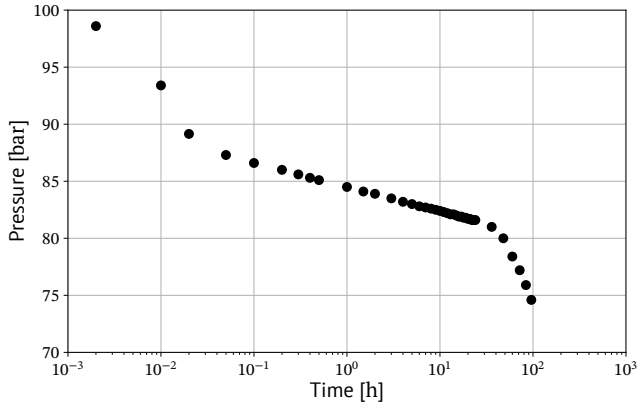


Figure 3.10: Plot of example data

Inserting Eqs. (3.61) and (3.62) into Eq. (3.59) gives the permeability estimate:

$$\begin{aligned} k &= \frac{9.23 \times 10^{-9}}{9.12 \times 10^{4}} \mathrm{m}^2 = 1.01 \times 10^{-13}\,\mathrm{m}^2 \\ &= 101\,\mathrm{mD} \end{aligned} \tag{3.63}$$

The skin can be estimated based on the initial pressure at $p_i = 100\,\mathrm{bar} = 100 \times 10^5\,\mathrm{Pa}$ and any pressure on the straight line. We will use the pressure at $t_s = 1\,\mathrm{h}$:

$$\ln\left(\frac{4k}{\mu\phi c_t r_w^2} \cdot (3600\,\mathrm{s})\right) = 13.1 \quad , \tag{3.64}$$

and the pressure difference is

$$(p_i - p_w(t_s)) = 100 \times 10^5\,\mathrm{Pa} - 84.5 \times 10^5\,\mathrm{Pa} = 15.5 \times 10^5\,\mathrm{Pa} \quad . \tag{3.65}$$

We get a skin factor estimate by inserting Eqs. (3.64) and (3.65) into Eq. (3.60):

$$S = \frac{1}{2}\left(\frac{15.5 \times 10^5}{9.12 \times 10^4} - 13.1 + 0.5772\right) = 2.2 \tag{3.66}$$

3.6 Wellbore storage effect

Due to the presence of the wellbore, the ideal constant flow boundary conditions are never obtained. The effect is especially important for the early time part of surface controlled well tests, and it is crucial to distinguish the effects of wellbore storage from the interpretable reservoir response. Actual down hole boundary conditions are illustrated in Fig. 3.11.

When a well is opened there is a lag time before the flow through to sand face reach a constant rate, and when a well is shut in, the sand face flow rate does not go to zero instantaneously.

In the following a simple model for the wellbore storage effect will be presented. The model is based on the assumption of a wellbore filled with a liquid with constant compressibility, c_l . The initial production at constant surface rate is due to expansion of liquid in the wellbore. The situation is illustrated in Fig. 3.12.

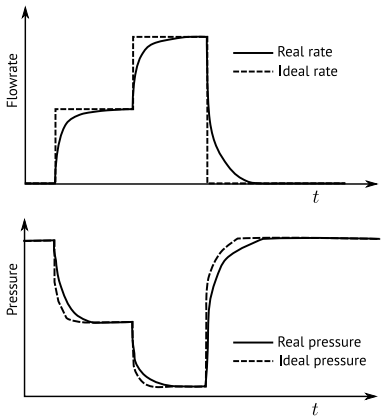


Figure 3.11: Non-ideal flow schedule due to wellbore storage

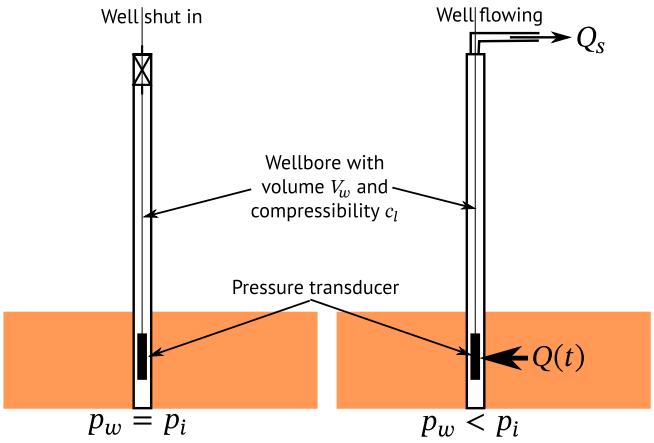


Figure 3.12: The liquid filled wellbore and the corresponding model for the wellbore storage effect

If $Q(t)$ is the production rate from the reservoir, and Q_s is the controlled production rate at the surface, we may express the mass balance in the wellbore volume,

"Mass in" - "Mass out" = "Change in mass" ,

as

Note: $B = Q/Q_s$ is the formation volume factor

$$\begin{aligned}\rho(Q(t) - Q_s B) &= \frac{\partial}{\partial t}(\rho V_w) \\ &= V_w \frac{\partial \rho}{\partial p_w}\frac{\partial p_w}{\partial t} \quad , \\ &= V_w c_l \rho \frac{\partial}{\partial t} p_w\end{aligned} \tag{3.67}$$

where the total wellbore volume V_w is assumed constant, and $c_l = \frac{1}{\rho}\frac{\partial \rho}{\partial p_w}$ is the liquid compressibility as defined in Eq. (2.6).

Wellbore storage constant.

The equation governing the well pressure is

$$\boxed{Q(t) - Q_s B = C_s \frac{d}{dt} p_w}, \quad C_s = c_l V_w \quad . \tag{3.68}$$

Here C_s is defined as the wellbore storage constant.

The reservoir production rate $Q(t)$ serve as a boundary condition for the diffusivity equation that governs the pressure in the reservoir. We have a set of coupled equations for reservoir and well. However, for small t most of the production is due to the expansion of the fluid in the wellbore, and we have $Q(t) \approx 0$:

$$p_w = p_i - \frac{Q_s B}{C_s} t \tag{3.69}$$

Initially, the well pressure varies linearly with time due to wellbore storage.

This early time wellbore storage equation can be utilized to estimate the wellbore storage constant coefficient from a time versus pressure plot. When the liquid compressibility c_l is known, this would then give an estimate of the wellbore volume V_w. A large mismatch between the tubing and casing volume below the test valve and the estimated wellbore volume from the early time wellbore storage equation could be an indication of e.g. fractures around the well, as such fractures would effectively contribute to the wellbore volume V_w in our equations.

We may introduce the dimensionless time and well pressure variables (Eq. (3.39))

$$t_D = \frac{k}{\mu\phi c_t r_w^2} t \qquad p_{Dw} = (p_i - p_w)\frac{2\pi kh}{Q\mu} \quad ,$$

to express Eq. (3.69) as

$$p_{Dw} = \frac{1}{C_{sD}} t_D \quad , \tag{3.70}$$

where C_{sD} is a dimensionless wellbore storage constant. We see by inserting the dimensionless variables into Eq. (3.69) that the dimensionless storage constant is

Dimensionless wellbore storage constant.

$$\begin{aligned} C_{sD} &= \frac{1}{2\pi\phi c_t h r_w^2} C_s \\ &= \frac{1}{2\phi}\frac{c_l}{c_t}\left(\frac{V_w}{\pi r_w^2 h}\right) \end{aligned} \quad . \tag{3.71}$$

From Eq. (3.71) we observe that the C_{sD} is proportional to the ratio of total wellbore volume to the wellbore volume in the completed interval. The dimensionless wellbore storage constant C_{sD} is therefore always larger than one, and can be very large in long and deep wells. Values close to one can only be obtained in a test controlled by downhole rates and build up tests controlled by downhole valves.

Downhole control valves minimize wellbore storage.

Inspection of the solution to the fully coupled wellbore–reservoir system have shown[4] that the wellbore storage effect must be taken into account for times

$$t_D < 60 C_{sD} \quad . \tag{3.72}$$

Since typically $C_{sD} \gg 1$, wellbore storage tend to obscure the region where we need to take into account the difference between a finite wellbore solution and the line-source solution (3.52).

The model for wellbore storage that has been presented in this chapter is very simplified, and the validity of the model in real world situations may be questioned. The main complication may be that oil wells tend to produce two phase at surface, and that prior to a buildup the wellbore usually contains a two-phase mixture which segregate after shutdown. In a drawdown test the situation is reversed, and in an appraisal well test drawdown there is a period of rising liquid level until fluid reaches the wellhead.

[4] R. Agarwal R. G. Al-Hussainy and H. J Ramey. "An Investigation of Wellbore Storage and Skin in Unsteady Liquid Flow - I. Analytical Treatment." In: *SPE Journal* 10.3 (Sept. 1970), pp. 279–290. DOI: 10.2118/2466-PA.

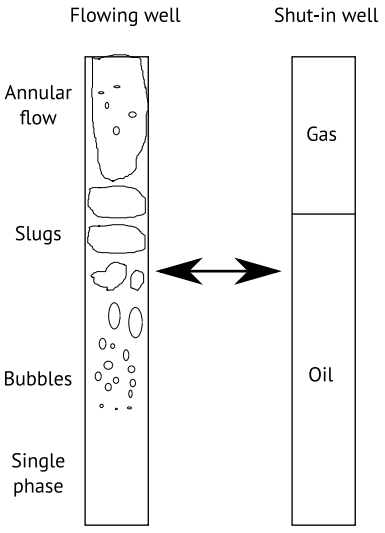


Figure 3.13: Segregating two-phase mixture in well-bore

4
Buildup test

In a buildup test, a well that ideally have been producing at a constant rate is shut, and the bottom hole pressure is recorded. Well tests in exploration wells and new wells are often performed as a drawdown–buildup sequence as shown in Fig. 4.1.

In addition to providing data for reservoir characterization, such as permeability and skin, buildup tests can also provide data for reservoir monitoring, in particular reservoir pressure data.

Planned buildup tests have a cost in terms of lost production, and this will limit the amount of available late time shut in data. However, production wells normally do not produce at 100% efficiency, and in wells with permanent downhole pressure gauges the periods of unplanned shut-in may provide valuable well test data at no extra cost.

It is easier to get high quality data from buildup than from drawdown since maintaining zero rate is trivial compared to maintaining a fixed rate, and the effect of wellbore storage is minimized by using a dowhhole valve.

Ideally rates should be stable before shut-in, and the determination of the effective production time, which is used in the analysis, can be challenging.

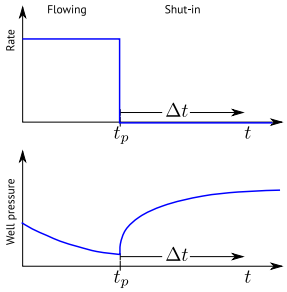


Figure 4.1: Ideal drawdown–buildup sequence

4.1 Superposition principle

In this section we will present the superposition principle. Let $\mathscr{L}$ be a partial differential operator, such that

$$\mathscr{L}p = 0 \quad , \tag{4.1}$$

is a partial differential equation for functions p. Further, let

$$\mathscr{G}p = f \tag{4.2}$$

be a operator giving the boundary conditions. In our case, $\mathscr{L}$ would be the diffusivity equation in the region given by the reservoir, while $\mathscr{G}$ would be an operator that restricts p to the boundary of the reservoir (e.g. the boundary given by $r = r_w$), and f would be the function that $\mathscr{G}p$ is required to equal on the boundary of the reservoir (e.g. a constant rate in the well).

We say that an operator $\mathcal{L}$ is *linear* if

$$\begin{aligned} \mathcal{L}(p_1 + p_2) &= \mathcal{L}p_1 + \mathcal{L}p_2 \\ \mathcal{L}(cp) &= c\mathcal{L}p \quad , \end{aligned} \tag{4.3}$$

where c is a scalar. The linearity of an operator $\mathcal{L}$ makes it impossible to do operations such as taking the square of the function p, but it allows for taking the second derivative. Thus, the diffusivity equation (2.13) is a linear partial differential equation.

The *superposition principle* states that for all linear systems, the net response caused by two or more stimuli is the sum of the responses that would have been caused by each stimulus individually.

Superposition can be used to add solutions to linear differential equations with linear boundary conditions.

We observe that solutions to linear differential equations with linear boundary conditions obey superposition: Given two functions $p_1(x,t)$ and $p_2(x,t)$ that are solutions to $\mathcal{L}p_i = 0$ with boundary conditions

$$\mathcal{G}p_1 = f_1(x,t) \quad \text{and} \quad \mathcal{G}p_2 = f_2(x,t) \quad , \tag{4.4}$$

where both $\mathcal{L}$ and $\mathcal{G}$ is linear operators. Then $p = p_1 + p_2$ is a solution to

$$\mathcal{L}p = 0 \tag{4.5}$$

with boundary condition

$$\mathcal{G}p = f_1(x,t) + f_2(x,t) \quad . \tag{4.6}$$

In this chapter we will use the superposition principle in time to obtain solutions to buildup in terms of the fundamental solution to drawdown derived in the previous chapter (Eq. (3.17)). In later chapters we will show how the superposition principle can be used in space to obtain solutions that take into account the effect of reservoir boundaries (See page 65).

The pressure solution for a drawdown-buildup sequence in a well is the same as the sum of the solutions for two wells in the same location that is started at different times. Note that due to the outer boundary condition, $p(\infty,t) = p_i$, it is the pressure $p - p_i$ that has this property.

An ideal buildup test has the rate history (boundary condition) shown in Fig. 4.2. By superposition, this can be replaced by *two wells* in the same location that is started at different times with opposite rates as shown in Fig. 4.3.

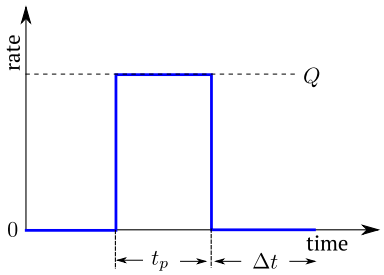


Figure 4.2: Buildup test rate history with production time t_p and buildup time Δt

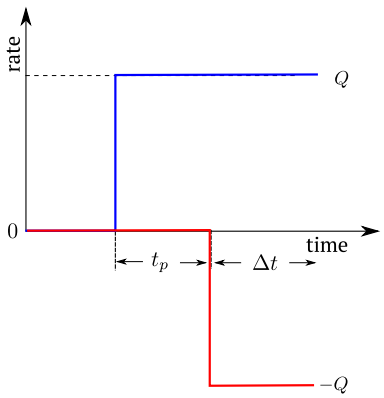


Figure 4.3: Equivalent two-well rate history for build up using superposition. One well (in blue) has rate Q and the other well (in red) has the opposite rate $-Q$. The sum of the rates is the same as the buildup test rate in Fig. 4.2

4.2 Horner analysis

We will now derive the well pressure for a well test where both the production time t_p and buildup time Δt is short enough to employ the transient infinitely acting solution. Due to superposition, the expression for well pressure during buildup will contain two terms: One for a well with constant rate Q starting at time $t = 0$, and one for a well with constant rate $-Q$ starting at time $t = t_p$. Apart from the period dominated by wellbore storage and skin effects just after start of shut-in,

we can use the logarithmic approximation (3.29) for both terms:

$$\begin{aligned} p_1 - p_i &= -\frac{Q\mu}{4\pi kh}\left[\ln\left(4\eta\frac{(t_p+\Delta t)}{r_w^2}\right) - \gamma + 2S\right] \\ p_2 - p_i &= \frac{Q\mu}{4\pi kh}\left[\ln\left(4\eta\frac{\Delta t}{r_w^2}\right) - \gamma + 2S\right] \quad , \end{aligned} \tag{4.7}$$

where the well with pressure p_1 has rate Q and the well with pressure $p_2$has rate $-Q$. Note that when we superposition two solutions to the partial differential operator $\mathscr{L}$, we also add the boundary conditions $\mathscr{G}p = f$. Since $\mathscr{L}p_i = 0$ for any scalar p_i when $\mathscr{L}$ is the operator for the diffusivity equation, we can use $p - p_i$ to ensure that the outer boundary condition stays zero, thus $p(\infty, t) = p_i$ for all solutions.

Applying the superposition principle, where we note that any effect of skin is equal in both terms and cancel out, we obtain:

$$\begin{aligned} p_w - p_i &= (p_1 - p_i) + (p_2 - p_i) \\ &= -\frac{Q\mu}{4\pi kh}\left[\ln\left(\frac{4\eta(t_p+\Delta t)}{r_w^2}\right) - \ln\left(\frac{4\eta\Delta t}{r_w^2}\right)\right] \\ &= -\frac{p_c}{2}\ln\left(\frac{t_p+\Delta t}{\Delta t}\right) \quad . \end{aligned} \tag{4.8}$$

Characteristic pressure $p_c = \frac{Q\mu}{2\pi kh}$

This can be rearranged as

$$\begin{aligned} p_w &= p_i - \frac{p_c}{2}\ln\left(\frac{t_p+\Delta t}{\Delta t}\right) \\ &= m\ln\left(\frac{t_p+\Delta t}{\Delta t}\right) + C, \end{aligned} \tag{4.9}$$

where $m = -p_c/2$ and C are constants independent of time. Note that m equals the constant in Eq. (3.58) for the drawdown test. However, while the pressure was a function of $\ln(t)$ in the drawdown test, we observe that pressure is a function of $\ln\left[(t_p + \Delta t)/\Delta t\right]$ in this buildup test. The corresponding plot of p_w versus is $\ln\left[(t_p + \Delta t)/\Delta t\right]$ is called the Horner plot (see Fig. 4.4).

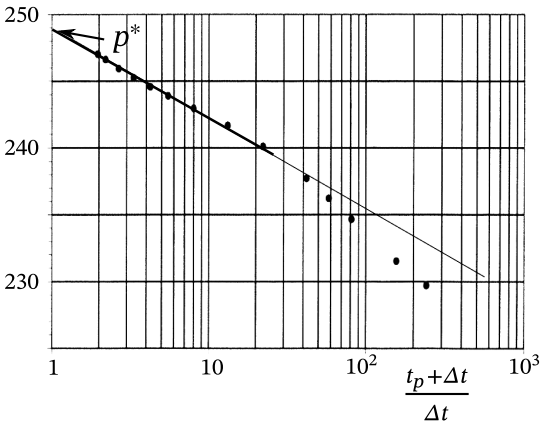


Figure 4.4: An example of a Horner plot, where pressure is plotted as a function of $\ln\left[(t_p + \Delta t)/\Delta t\right]$. Permeability and skin is estimated from the straight line fit. Note that increasing time goes from right to left on the x-axis.

The time $(t_p + \Delta t)/\Delta t$ is sometimes referred to as Horner time. Observe that $(t_p + \Delta t)/\Delta t$ decreases when Δt increases. Further, infinite time $\Delta t \to \infty$ corresponds to $(t_p + \Delta t)/\Delta t \to 1$.

Similar to the drawdown test, the *permeability* can be estimated based on the derivative of well pressure as a function of $\ln\left(\frac{t_p+\Delta t}{\Delta t}\right)$. The slope, m, of the straight line on the Horner plot (Eq. (4.8)) is

$$m = \frac{dp_w}{d\ln\left(\frac{t_p+\Delta t}{\Delta t}\right)} = -\frac{p_c}{2} = -\frac{Q\mu}{4\pi kh} \quad , \tag{4.10}$$

which gives the permeability

Permeability

$$\boxed{k = -\frac{Q\mu}{4\pi h}\frac{1}{m}} \quad . \tag{4.11}$$

The slope should be determined by fitting a straight line to the pressure points in the linear region. If we, for simplicity, use two points on the straight line corresponding to Δt_1 and Δt_2, where $\Delta t_1 < \Delta t_2$. Then $(t_p + \Delta t_1)/\Delta t > (t_p + \Delta t_2)/\Delta t_2$, so

$$\begin{aligned} m &= \frac{p_w(\Delta t_1) - p_w(\Delta t_2)}{\ln\left(\frac{t_p+\Delta t_1}{\Delta t_1}\right) - \ln\left(\frac{t_p+\Delta t_2}{\Delta t_2}\right)} \\ &= \frac{p_w(\Delta t_1) - p_w(\Delta t_2)}{\ln\left(\frac{t_p+\Delta t_1}{\Delta t_1}\frac{\Delta t_2}{t_p+\Delta t_2}\right)} \quad . \end{aligned} \tag{4.12}$$

We then have

$$\begin{aligned} k &= -\frac{Q\mu}{4\pi h}\frac{1}{m} = \frac{Q\mu}{4\pi h}\frac{1}{-m} \\ &= \frac{Q\mu}{4\pi h}\left[\frac{\ln\left(\frac{\Delta t_1}{t_p+\Delta t_1}\frac{t_p+\Delta t_2}{\Delta t_2}\right)}{p_w(\Delta t_1) - p_w(\Delta t_2)}\right] \quad . \end{aligned} \tag{4.13}$$

Plots are often $\log_{10}$ based, and it is natural to select $\frac{t+\Delta t_1}{\Delta t_1}$ and $\frac{t+\Delta t_2}{\Delta t_2}$ one decade apart. Since $\frac{\ln(10)}{4\pi} \approx 0.183$ we then have

$$k = 0.183\frac{Q\mu}{h\left(p_w(\Delta t_1) - p_w(\Delta t_2)\right)} \quad . \tag{4.14}$$

The Horner analysis also provide an estimate for the skin. The pressure after shut-in (Eq. (4.8)),

$$p_w(t_p + \Delta t) = p_i - \frac{p_c}{2}\ln\left(\frac{t_p + \Delta t}{\Delta t}\right) \quad , \tag{4.15}$$

is independent of skin, while the pressure just before shut-in,

$$p_w(t_p) = p_i - \frac{p_c}{2}\left(\ln\left(\frac{4\eta}{r_w^2}t_p\right) - \gamma + 2S\right) \quad , \tag{4.16}$$

is skin dependent. By subtracting Eqs. (4.15) and (4.16) we get

$$p_w(t_p + \Delta t) - p_w(t_p) = \frac{p_c}{2}\left[\ln\left(\frac{4\eta}{r_w^2}\frac{t_p\Delta t}{t_p + \Delta t}\right) - \gamma + 2S\right] \quad . \tag{4.17}$$

Thus, when the permeability and pressure at start of shut in is known, the skin factor may me estimated based on the pressure at a specific time Δt after shut in.

$$\begin{aligned} S &= \frac{1}{p_c}\left(p_w(t_p + \Delta t) - p_w(t_p)\right) - \frac{1}{2}\ln\left(\frac{4\eta}{r_w^2}\frac{t_p\Delta t}{t_p + \Delta t}\right) + \frac{\gamma}{2} \\ &= -\frac{1}{2m}\left(p_w(t_p + \Delta t) - p_w(t_p)\right) - \frac{1}{2}\ln\left(\frac{4\eta}{r_w^2}\frac{t_p\Delta t}{t_p + \Delta t}\right) + \frac{\gamma}{2} \quad . \end{aligned} \tag{4.18}$$

Typically the straight line extrapolated pressure at $\frac{t_p+\Delta t}{\Delta t} = 1$ (i.e. infinite time), p^*, (see Fig. 4.4) is used:

Skin

$$\boxed{S = -\frac{1}{2m}\left(p^* - p_w(t_p)\right) - \frac{1}{2}\ln\left(\frac{4\eta t_p}{r_w^2}\right) + \frac{\gamma}{2}} \quad . \tag{4.19}$$

In the derivations above we have assumed a constant production rate in the whole production period. This may not always be possible to obtain, especially for unplanned shut down periods. In these cases we may use the effective production time (also known as equivalent constant rate drawdown time), defined as

Effective production time

$$t_{ep} = \frac{\int_0^{t_p} Q(\tau)d\tau}{Q(t_p)} \quad . \tag{4.20}$$

The basis for the approximation is not rigorous, but it is adequate if the most recent flow rate is reasonably stable and maintained long enough.

The Horner analysis is based on the infinite acting solution, so it is only valid if the production and drawdown period is short (Eq. (3.55)):

$$t_p + \Delta t_{\max} < \frac{r_o^2}{4\eta} = \frac{\mu\phi c_t r_o^2}{4k} \quad , \tag{4.21}$$

where r_o is the outer radius of the reservoir (distance to closest barrier). Note, however, that the Horner analysis can be *approximately* extended so that it may be used for analyzing transient buildups outside of this strict area of validity (see page 49). When Δt goes to infinity, we have

$$\Delta t \to \infty \Rightarrow \frac{t_p + \Delta t}{\Delta t} \to 1 \Rightarrow \ln\left(\frac{t_p + \Delta t}{\Delta t}\right) \to 0 \quad . \tag{4.22}$$

We thus see from Eq. (4.8) that the extrapolated pressure at infinite time p^* should equal p_i whenever the Horner approximation is strictly valid. Any deviation from this is an indication of depletion, and we will see later (page 58) that p^* plays a role when estimating reservoir pressure in the generalized Horner analysis.

When $t_p \gg \Delta t$ we have $t_p + \Delta t \simeq t_p$. Using this approximation for long production times t_p, then Eq. (4.9) simplifies to

$$\begin{aligned} p_w &= m\ln\left(\frac{t_p + \Delta t}{\Delta t}\right) + C \simeq m\ln\left(\frac{t_p}{\Delta t}\right) + C \\ &= -m\ln(\Delta t) + C' \quad , \end{aligned} \tag{4.23}$$

thus a plot of pressure versus Δt would yield a straight line from which one could estimate permeability and skin. However, a large t_p might violate the validity range of the infinite acting solution. In the next section will will consider a more general treatment of long production periods.

4.3 Example

In this example section we will employ Horner analysis on a buildup test. We assume that a vertical discovery well is produced at a reservoir rate of 100.0 m^3/d for a period of 12 hours prior to a closure for an

initial pressure buildup survey. The production data and estimated reservoir and fluid properties are summarized in Table 4.1. We assume that the well is completed across the entire formation.

The plot of the pressure development is shown in Fig. 4.5. We can now estimate the permeability and skin based on Eq. (4.11) and Eq. (4.19), respectively. We start with the permeability.

	SPE Metric	SI
h	10 m	10 m
Q	100 m^3/d	1.16×10^{-3} m^3/s
r_w	0.12 m	0.12 m
μ	0.6 cP	6×10^{-4} Pa s
ϕ	0.2	0.2
c_t	2.6×10^{-4} bar^{-1}	2.6×10^{-9} Pa^{-1}

Table 4.1: Basic data for example.

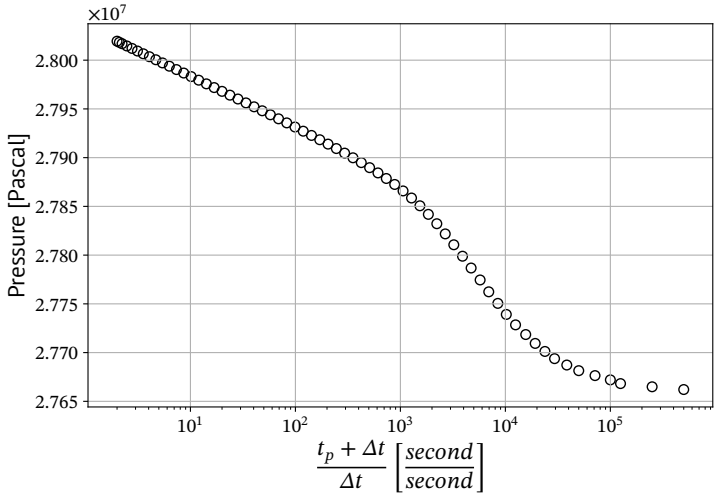


Figure 4.5: The pressure data from the buildup test in a Horner plot.

For estimating the permeability we need the slope of the straight part of the pressure curve in the Horner plot. We observe that the curve is approximately straight between 10^1 and 10^2, which corresponds to pressures of approximately 2.798×10^7 Pa and 2.793×10^7 Pa, respectively. We can then calculate the slope m of the straight part as

$$m \simeq \frac{2.793 \times 10^7 \text{ Pa} - 2.798 \times 10^7 \text{ Pa}}{\ln(10^2) - \ln 10^1} = -2.17 \times 10^4 \text{ Pa} \quad . \tag{4.24}$$

Employing Eq. (4.11) we can then estimate the permeability as

$$\begin{aligned} k &= -\frac{Q\mu}{4\pi h m} \\ &= \frac{100.0 \text{ m}^3/\text{d} \cdot 6.0 \times 10^{-4} \text{ Pa s}}{8.64 \times 10^4 \text{ s/d} \cdot 4\pi \cdot 10.0 \text{ m} \cdot 2.17 \times 10^4 \text{ Pa}} = 2.55 \times 10^{-13} \text{ m}^2 \end{aligned} \tag{4.25}$$

This corresponds to approximately 255 mD.

For Eq. (4.19) we need the pressure at shut in, $p_w(t_p)$, and the pressure at $\frac{t_p+\Delta t}{\Delta t} = 1$ (i.e. infinite time), p^*, (see Fig. 4.4). By extrapolating the curve in Fig. 4.5 to high values, we estimate the pressure at shut in to be $p_w(t_p) \simeq 2.766 \times 10^7$ Pa. The pressure p^* at $(t_p + \Delta t)/\Delta t = 1$ is estimated as $p^* = 2.804 \times 10^7$ Pa. This yields the following estimate

for the skin from Eq. (4.19):

$$\begin{aligned} S &= -\frac{1}{2m}\left(p^* - p_w(t_p)\right) - \frac{1}{2}\ln\left(\frac{4kt_p}{\mu\phi c_t r_w^2}\right) + \frac{\gamma}{2} \\ &= \frac{1}{2\cdot 2.24\times 10^4\ \text{Pa}}(2.804\times 10^7\ \text{Pa} - 2.766\times 10^7\ \text{Pa}) \\ &\quad - 0.5 * \ln\left(\frac{4\cdot 2.47\times 10^{-13}\ \text{m}^2\cdot 12\ \text{h}\cdot 3.6\times 10^3\ \text{s/h}}{6.0\times 10^{-4}\ \text{Pa s}\cdot 0.2\cdot 2.6\times 10^{-9}\ 1/\text{Pa}\cdot(0.07\ \text{m})^2}\right) + \frac{\gamma}{2} \\ &= 0.46 \end{aligned} \tag{4.26}$$

Thus the well appears to have little skin.

4.4 Miller–Dyes–Hutchinson (MDH) analysis

The Horner analysis assumes infinite acting flow at shut-in, that is a short production period. The Miller–Dyes–Hutchinson (MDH) analysis is based on the opposite assumption: That the stable production period before shut-in is very long, so that pressure changes which originates from production can be ignored compared to the pressure changes due to shut-in.

Rates for a general buildup test are presented in Fig. 4.6. Based on the superposition principle, this rate history may be replaced by two wells with the rate history shown in Fig. 4.7 The well pressure before shut in ($t \le T$) is

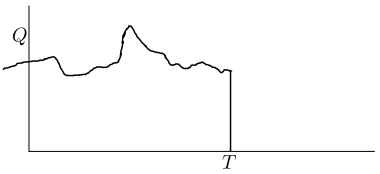


Figure 4.6: Rate history for a general buildup test

$$p_1(t) - p_i = -\frac{Q(t)\mu}{4\pi kh}\left[F(t) + 2S\right] \quad , \tag{4.27}$$

where $F(t)$ is some function. If we assume infinite acting transient solution for the second well producing at a constant rate $-Q$, the well pressure is given by

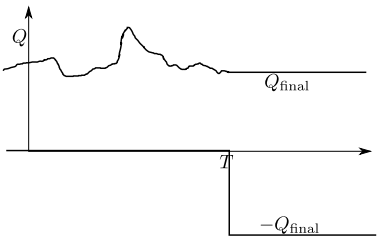


Figure 4.7: Equivalent rate history for two wells in the same location

$$p_2(t) - p_i = \frac{Q\mu}{4\pi kh}\left[\ln\left(\frac{4\eta}{r_w^2}\Delta t\right) - \gamma + 2S\right] \quad . \tag{4.28}$$

Using the superposition principle, then the well pressure after shut in ($t > T$) is

$$p_w(\Delta t) = p_i - \frac{Q\mu}{4\pi kh}\left[F(T+\Delta t) - \ln\left(\frac{4\eta}{r_w^2}\Delta t\right) + \gamma\right] \quad . \tag{4.29}$$

Note that, just as in the Horner case, the well pressure after shut-in is independent of skin. Subtracting Eqs. (4.27) and (4.29), and assuming that pressure changes which originates from production can be ignored compared to the pressure changes due to shut in (that is $F(T+\Delta t) \approx F(t)$, thus $p_1(T+\Delta t) \simeq p_1(T) = p_w(T)$), we get

$$p_w(\Delta t) - p_w(T) = \frac{Q\mu}{4\pi kh}\left(\ln\left(\frac{4\eta}{r_w^2}\Delta t\right) - \gamma + 2S\right) \quad . \tag{4.30}$$

We see that the pressure is linear in $\ln(\Delta t)$, as illustrated in Fig. 4.8. The permeability can be estimated based on the slope, m, of a fitted straight line

$$\boxed{k = \frac{Q\mu}{4\pi h}\frac{1}{m}} \quad . \tag{4.31}$$

Permeability

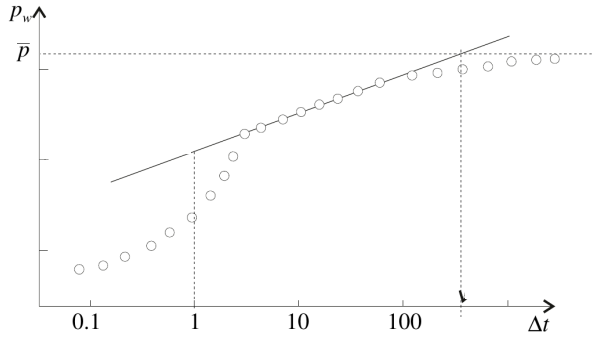


Figure 4.8: A plot of pressure versus the logarithm of time (semilog plot), commonly denoted a MDH plot. The pressure is linear in $\ln(\Delta t)$.

We may alternatively select data at two times Δt_1 and Δt_2 on the line

$$k = \frac{Q\mu}{4\pi h} \frac{\ln\left(\frac{\Delta t_2}{\Delta t_1}\right)}{p_w(\Delta t_2) - p_w(\Delta t_1)} \quad . \tag{4.32}$$

By solving for S in Eq. (4.30), we see that the skin factor can be estimated based on the well pressure at a specific time Δt_s after shut-in:

Skin

$$\boxed{S = \frac{1}{2m}\left(p_w(\Delta t_s) - p_w(T)\right) - \frac{1}{2}\left(\ln\left(\frac{4k}{\mu\phi c_t r_w^2}\Delta t_s\right) - \gamma\right)} \quad . \tag{4.33}$$

4.5 Example

In this example section we will employ MDH-analysis on a buildup test. We assume that a vertical discovery well is produced at a reservoir rate of 100.0 m^3/d for a period of 50 days before closure for a pressure buildup survey. The production data and estimated reservoir and fluid properties are summarized in Table 4.2. We assume that the well is completed across the entire formation.

A semi-log plot of the pressure development is shown in Fig. 4.9. We can now estimate the permeability and skin based on Eq. (4.31) and Eq. (4.33), respectively. We start with the permeability.

	SPE Metric	SI
h	10 m	10 m
Q	100 m^3/d	1.16×10^{-3} m^3/s
r_w	0.07 m	0.07 m
μ	0.6 cP	6×10^{-4} Pa s
ϕ	0.2	0.2
c_t	2.6×10^{-4} bar^{-1}	2.6×10^{-9} Pa^{-1}

Table 4.2: Basic data for example.

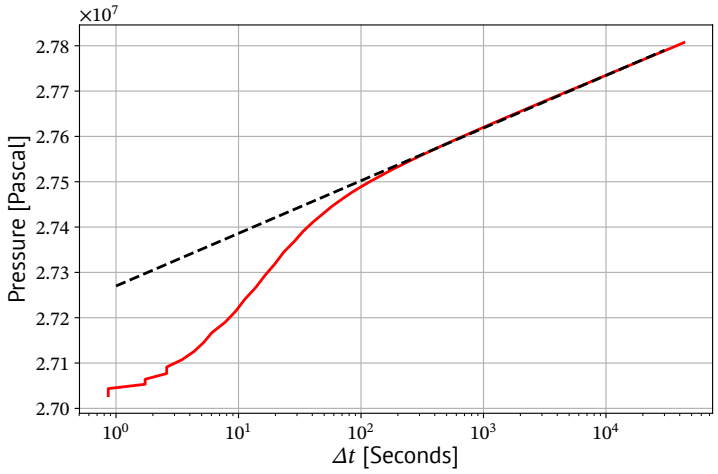


Figure 4.9: The pressure data from the buildup test in a semi-log plot. The plot includes a stapled line indicating the linear section of the pressure plot.

For estimating the permeability we need the slope of the straight part of the pressure curve in the semi-log plot. We observe that the curve is approximately straight from 10^3 and on-wards. The extrapolated line in Fig. 4.9 goes through the points $(1 \times 10^1\,\text{s}, 2.74 \times 10^7\,\text{Pa})$ and $(1 \times 10^3\,\text{s}, 2.76 \times 10^7\,\text{Pa})$. This gives a slope of

$$m = \frac{2.76 \times 10^7\,\text{Pa} - 2.74 \times 10^7\,\text{Pa}}{\ln(10^3) - \ln(10^1)} = 4.34 \times 10^4\,\text{Pa} \quad . \tag{4.34}$$

From Eq. (4.31) we can then estimate the permeability as

$$\begin{aligned} k &= \frac{Q\mu}{m4\pi h} \\ &= \frac{1.16 \times 10^{-3}\,\text{m}^3/\text{s} \cdot 6.0 \times 10^{-4}\,\text{Pa s}}{4.34 \times 10^4\,\text{Pa} \cdot 4\pi \cdot 10.0\,\text{m}} \\ &= 1.28 \times 10^{-13}\,\text{m}^2 \simeq 129\,\text{mD} \quad . \end{aligned} \tag{4.35}$$

For Eq. (4.33) we need the pressure at shut in, $p_w(t_p)$. By extrapolating the plot in Fig. 4.9 to a low value, we can estimate the pressure at shut in to approximately $p_w(t_p) = 2.705 \times 10^7$ Pa. Using the point $(\Delta t_s, p_w(\Delta t_s)) = (1 \times 10^1\,\text{s}, 2.74 \times 10^7\,\text{Pa})$ we can then estimate the skin as:

$$\begin{aligned} S &= \frac{1}{2}\left(\frac{p_w(\Delta t_s) - p_w(t_p)}{m} - \ln\left(\frac{4k}{\mu\phi c_t r_w^2}\Delta t_s\right) + \gamma\right) \\ &= \frac{1}{2}\left(\frac{2.74 \times 10^7 - 2.705 \times 10^7}{4.34 \times 10^4} - 5.68 - \ln(10^1) + 0.57721\right) \\ &= 0.33 \end{aligned} \tag{4.36}$$

Thus the well appears to have little skin.

4.6 Slider analysis and desuperposition

As shown in Fig. 4.7, a buildup test is analyzed in terms of superposition of the contribution from two wells: One well has the real production history up to shut-in, and a constant rate at later times, and another well has a constant negative rate after shut-in. In MDH analysis we are assuming that the contribution from the first well is zero, so the shut-in period that can be analyzed using MDH is limited. Any rate changes just prior to shut-in, which will contribute to the transient behavior are also ignored. In this section we will first discuss how the investigation period can be extended by taking into account the projected (semi steady state) contribution from the first well (Slider analysis), and secondly possible strategies for taking rate changes into account will be discussed. In both cases, the effects from the first well is incorporated into an effective pressure, and the analysis is performed in terms of Δt. This approach is called desuperposition.

In the next chapter we will see that pressure falls linearly in semi steady state (Eq. (5.14)), and in Slider analysis the pressure difference in Eq. (4.30) is replaced by the linearly projected pressure development as shown in Fig. 4.10. If we expand the pressure contribu-

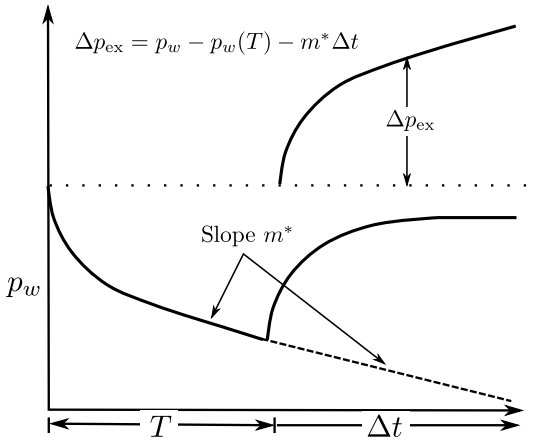


Figure 4.10: Slider analysis

tion from the first well ($F(T+\Delta t)$) to first order in Δt, and subtract Eqs. (4.27) and (4.29), we get

$$p_w(\Delta t) - p_w(T) - m^*\Delta t = \frac{Q\mu}{4\pi kh}\left(\ln\left(\frac{4\eta}{r_w^2}\Delta t\right) - \gamma + 2S\right) \quad , \qquad (4.37)$$

where the pressure derivative m^* at time T is

$$m^* = -\left.\frac{dp_w}{dt}\right|_{t=T} \quad . \qquad (4.38)$$

So by defining the effective pressure difference,

$$\boxed{\Delta p_{\rm ex}(\Delta t) = p_w(\Delta t) - p_w(T) - m^*\Delta t} \quad , \qquad (4.39)$$

Effective pressure difference by desuperposition.

we may extend the applicability of MDH type analysis. This effective pressure can also be used in the diagnostic plots that will be introduced on page 56, and used in several context thereafter.

Note that permanent dowhhole gauges are needed for obtaining the pressure derivative. Alternatively the derivative can be provided by reservoir simulation, however extreme caution should be observed if doing so since it is very easy to end up with self confirming assumptions (circle arguments). The projected pressure will also compensate for the effect of aquifer, communication with neighboring compartments, and injection/production in neighboring wells.

Desuperposition based on the overall pressure derivative, m^*, assumes that the well has a stable rate before shut-in. This may be difficult to achieve, in particular for producing wells experiencing an unplanned shut-in, and in this case the transients resulting from rate variations just prior to shut-in, $\Delta p_{w\rm sim}(\Delta t)$, may be calculated numerically, or based on analytical models. The pressure difference used in the analysis is then

$$\boxed{\Delta p_{\rm ex}(\Delta t) = p_w(\Delta t) - p_w(T) + \Delta p_{w\rm sim}(\Delta t) - m^*\Delta t} \quad , \qquad (4.40)$$

Numerical desuperposition

where m^* is the overall pressure trend measured by downhole gauges.

4.7 Similarity between drawdown and buildup responses

In this section we will discuss in what sense the pressure responses in buildup are mirror images of the corresponding drawdown responses,

and how this enables the use of drawdown analysis tools, such as the semilog plot, for buildup analysis.

For short production and buildup (infinitely acting) the buildup response is (see Eq. (4.17))

$$p_w(\Delta t) - p_w(t_p) = \frac{Q\mu}{4\pi kh}\left[\ln\left(\frac{4\eta}{r_w^2}\frac{t_p\Delta t}{t_p+\Delta t}\right) - \gamma + 2S\right] \quad , \tag{4.41}$$

and the corresponding drawdown test response is (see Eq. (3.57))

$$p_w(t) - p_w(0) = -\frac{Q\mu}{4\pi kh}\left[\ln\left(\frac{4\eta}{r_w^2}t\right) - \gamma + 2S\right] \quad . \tag{4.42}$$

Thus, *buildup is the mirror image of drawdown* when expressed in terms of an effective time (Agarwal time)

$$t_e = \frac{t_p\Delta t}{t_p+\Delta t} \quad . \tag{4.43}$$

For a long production period and short buildup the buildup response is (see Eq. (4.30))

$$p_w(\Delta t) - p_w(t_p) = \frac{Q\mu}{4\pi kh}\left[\ln\left(\frac{4\eta}{r_w^2}\Delta t\right) - \gamma + 2S\right] \quad . \tag{4.44}$$

And the corresponding short time drawdown test response is again given by Eq. (4.42). Thus, that in this case *buildup is the mirror image of drawdown* in terms of real time, but also with respect to Agarwal time, since

$$t_e = \frac{t_p\Delta t}{t_p+\Delta t} = \Delta t\frac{1}{1+\frac{\Delta t}{t_p}} \approx \Delta t \quad , \tag{4.45}$$

in this case. We may conclude that, at least approximately, the radial transient buildup is the mirror image of drawdown, Irrespective of the length of the production time, t_p, provided that drawdown time t is replaced by the Agarwal time.

$$\boxed{t_e = \frac{t_p\Delta t}{t_p+\Delta t}} \quad . \tag{4.46}$$

When analyzed in terms of Agarwal time, the radial infinite acting transient buildup is equivalent to drawdown.

Based on this we also see that approximately we may employ an extended Horner analysis to long production periods where the infinite acting solution is not applicable.

Horner analysis may be extended to long production periods.

The Agarwal time transformation includes wellbore storage and skin effects, but non radial flow data (as in wells with hydraulic fractures) will not be transformed accurately. Similarly, late time behavior for drawdown and buildup are not similar under the transformation.

As will be show in the next two chapters, the late time behavior of a well test is used to infer information related to reservoir boundaries and heterogeneities. The theory and procedures will be discussed in terms of drawdown. Since the Agarwal time transformation is not applicable, some sort of desuperposition is needed if buildup data is to be used in this context. Examples of desuperposition is Eqs. (4.39) and (4.40). The most general form of desuperposition is a method called deconvolution, which is discussed in a separate chapter (page 137). Correct desuperposition includes all effects, so that the late time behavior for drawdown and buildup are similar.

5
Finite reservoir

Real reservoirs are not infinite, and in this chapter we will discuss how the finite size of the reservoir influence a well test and which properties may be inferred. We will also discuss how well testing may be used in reservoir monitoring by giving information related to the pressure in the reservoir at the time of the test.

5.1 Semi steady state

Late in a drawdown test, the flow reaches semi steady state in a closed reservoir. At semi steady state the pressure profile is constant over time, while the average reservoir pressure falls due to production. The situation is illustrated in Fig. 5.1

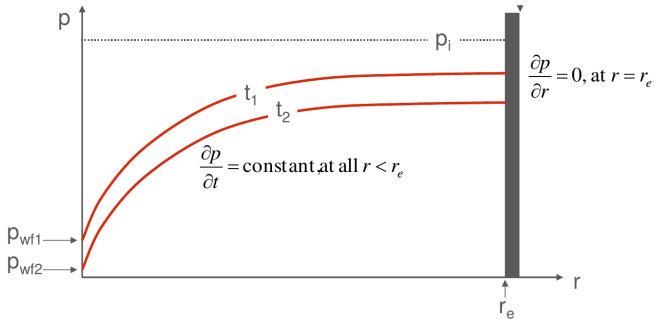


Figure 5.1: Semi steady state pressure profile

In the following we will discuss semi steady state flow in a cylindrical reservoir. First, the steady state profile will be derived, and by adding the condition that the average pressure falls linearly with time we will derive the equation for well pressure as a function of time.

The criterion for semi steady state is that pressure falls with a constant rate in the whole drainage area. This gives the following equation for the pressure profile, $p(r)$ (see Eqs. (2.19) and (2.28)):

$$\frac{1}{r}\frac{\partial}{\partial r}\left(r\frac{\partial p}{\partial r}\right) = \frac{1}{\eta}\frac{\partial p}{\partial t} = C_1 \quad . \tag{5.1}$$

The inner boundary condition on Eq. (5.1) is given by Darcys law,

$$\frac{Q}{h2\pi r} = \frac{k}{\mu}\left(\frac{\partial p}{\partial r}\right) \quad , \tag{5.2}$$

that is

$$\left(r\frac{\partial p}{\partial r}\right)_{r=r_w} = \frac{Q\mu}{2\pi kh} = p_c \quad , \tag{5.3}$$

while the outer boundary condition is no flow, which using Darcys law transform to zero pressure gradient:

$$\left(r\frac{\partial p}{\partial r}\right)_{r=r_o} = 0 \quad \Rightarrow \quad \left(\frac{\partial p}{\partial r}\right)_{r=r_o} = 0 \quad , \tag{5.4}$$

where r_o is the outer radius of the reservoir.

Integrating Eq. (5.1) with respect to r gives

$$r\frac{\partial p}{\partial r} = \frac{C_1}{2}r^2 + C_2 \quad . \tag{5.5}$$

We may apply the outer boundary condition (5.4) to to eliminate the integration constant C_2 from Eq. (5.5) ($C_2 = -\frac{r_o^2}{2}C_1$) which gives

$$r\frac{\partial p}{\partial r} = \frac{C_1}{2}\left(r^2 - r_o^2\right) \quad . \tag{5.6}$$

The constant C_1 is found by applying the inner boundary condition (5.3) to Eq. (5.6):

$$p_c = \left(r\frac{\partial p}{\partial r}\right)_{r=r_w} = \frac{C_1}{2}\left(r_w^2 - r_o^2\right) \tag{5.7}$$

$$C_1 = -\frac{2p_c}{r_o^2 - r_w^2} \approx -\frac{2p_c}{r_o^2} \quad . \tag{5.8}$$

In the last similarity we us that $r_o \gg r_w$, thus $r_o^2 - r_w^2 \simeq r_o^2$. Inserting Eq. (5.8) into Eq. (5.6) gives

$$\frac{\partial p}{\partial r} = -\frac{p_c}{r_o^2}\left(r - \frac{r_o^2}{r}\right) \quad . \tag{5.9}$$

We may now integrate both sides of Eq. (5.9) from r_w to r to get the pressure profile:

Pressure profile

$$p(r,t) - p_w(t) = p_c\left(\ln\left(\frac{r}{r_w}\right) - \frac{r^2 - r_w^2}{2r_o^2}\right) \quad . \tag{5.10}$$

As long as $r \ll r_o$ the last term in Eq. (5.10) can be ignored, so the pressure profile near the well has the familiar general steady state logarithmic form (2.36).

In a well test we are primarily interested in the well pressure, and p_w remains an arbitrary integration constant in Eq. (5.10). We may however integrate the pressure profile over the entire reservoir in order to get an expression for the average reservoir pressure, and by equating this pressure with the average pressure found by applying material balance, an expression for well pressure can be found.

The average reservoir pressure is given by the integral

Get average pressure by integrating the pressure profile.

$$\overline{p} = \frac{1}{\pi r_o^2}\int_{r_w}^{r_o} 2\pi r p(r)\, dr \quad . \tag{5.11}$$

Substituting the reservoir pressure profile (5.10) into Eq. (5.11), and integrating[1] gives the average pressure

[1] For the integration yielding Eq. (5.12) we use that

$$\int r\ln\left(\frac{r}{r_w}\right)dr = r^2\left(\frac{1}{2}\ln\left(\frac{r}{r_w}\right) - \frac{1}{4}\right)$$

$$\overline{p}(t) = p_w(t) + p_c\left(\ln\left(\frac{r_o}{r_w}\right) - \frac{3}{4}\right) \quad , \tag{5.12}$$

where again the condition $r_o \gg r_w$ has been used to eliminate small terms. Since the compressibility is constant, we may also calculate the average reservoir pressure from material balance:

Get average pressure from material balance.

$$\overline{p}(t) = p_i - \frac{Q}{c_t \phi V} t \quad , \tag{5.13}$$

where V is bulk volume, and c_t is total compressibility. The average pressure $\overline{p}$ in the two expressions (Eqs. (5.12) and (5.13)) should be the same, so we may eliminate it and solve for the semi steady state well pressure:

Semi steady state well pressure

$$\boxed{p_w(t) = p_i - \frac{Q}{c_t \phi V} t - p_c\left(\ln\left(\frac{r_o}{r_w}\right) - \frac{3}{4}\right)} \quad . \tag{5.14}$$

The well pressure (5.14) has two contributions: The average reservoir pressure, which decrease linearly with time, and a geometric correction, which depend logarithmically on reservoir size. The geometric correction is determined by the pressure profile and will vary with reservoir geometry and well placement. Eq. (5.14) for the well pressure is valid for a cylindrical reservoir with a well at the center.

Reservoir limit test

A reservoir limit test is a test that is run for a time long enough for the test to investigate the whole reservoir (see Eqs. (3.27) and (5.34)). The purpose of the test is to get information on reservoir size and shape.

Reservoir pore volume can be estimated from the derivative of pressure at semi steady state. In semi steady state (Eq. (5.14)) the derivative of well pressure is

$$\frac{d}{dt} p_w = -\frac{Q}{c_t \phi V} \quad , \tag{5.15}$$

so, if total compressibility is known, the reservoir pore volume is

Reservoir pore volume

$$\boxed{\phi V = -\frac{Q}{c_t \frac{d}{dt} p_w}} \quad . \tag{5.16}$$

Our Eq. (5.14) is valid for a very special (cylindrical) reservoir never seen in real life, and we have ignored the effect of skin. We will now derive a generalization of Eq. (5.14) valid for reservoirs of constant thickness of any shape. For a cylindrical reservoir the spatial correction depend on reservoir size through the outer radius r_o. It is not obvious what the corresponding characteristic length should be in a reservoir of general shape so we will use the reservoir area, A, instead:

$$\frac{r_o}{r_w} = \sqrt{\frac{\pi r_o^2}{\pi r_w^2}} = \sqrt{\frac{A}{\pi r_w^2}} \quad . \tag{5.17}$$

It is most convenient to work with dimensionless variables:

$$\begin{aligned} r_D &= \frac{1}{r_w} r \qquad t_D = \frac{\eta}{r_w^2} t \qquad p_D = \frac{p_i - p}{p_c} \\ h_D &= \frac{1}{r_w} h \quad A_D = \frac{1}{r_w^2} A \quad V_D = \frac{1}{r_w^3} V \end{aligned} \tag{5.18}$$

The semi steady state solution for a cylindrical reservoir on dimensionless form is then

$$p_{Dw} = \frac{2\pi}{A_D} t_D + \frac{1}{2}\left(\ln\left(\frac{A_D}{\pi}\right) - \frac{3}{2}\right) \quad . \tag{5.19}$$

Since the near well pressure profile has the familiar time independent logarithmic form, the effect of skin can be represented by the dimensionless skin factor. We may also incorporate the effect of reservoir shape and relative well placement into a dimensionless shape factor, C_A, with a corresponding contribution to the pressure[2]. Introducing skin and shape factor, the general semi steady state solution is written

[2] The shape factor C_A is called the Dietz shape factor.

General semi steady state well pressure

$$\boxed{p_{Dw} = \frac{2\pi}{A_D} t_D + \frac{1}{2}\left(\ln\left(\frac{4A_D}{C_A}\right) - \gamma + 2S\right)} \quad , \tag{5.20}$$

and we see that the shape factor is defined such that the spatial pressure correction is similar to the temporal infinitely acting solution (3.49)

$$p_{Dw} = \frac{1}{2}\left(\ln\left(4t_D\right) - \gamma + 2S\right) \quad . \tag{5.21}$$

By comparing Eqs. (5.19) and (5.20), we see that the shape factor for a cylindrical reservoir with a central well is

$$C_A = 4\pi \exp(3/2 - \gamma) = 31.6\ldots \quad . \tag{5.22}$$

For any other geometry we have

$$C_A < 31.6\ldots \quad . \tag{5.23}$$

5.2 Example

In this example we will estimate the reservoir volume by employing Eq. (5.16) on a drawdown test. We assume that a vertical well is produced at a reservoir rate of $100.0\,\mathrm{m^3/d}$ for a prolonged period. The relevant production data and estimated reservoir and fluid properties are summarized in Table 5.1.

The plot of the pressure development is shown in Fig. 5.2. We can then estimate the reservoir volume based on Eq. (5.16). We then need to estimate the slope of the linear part of the plot.

We observe that the curve is approximately straight between the times 1×10^7 s and 6×10^7 s. At 1×10^7 s the pressure is approximately 2.01×10^7 Pa, while the pressure is approximately 1.65×10^7 Pa at time 6×10^7 s. This gives a slope of

$$\frac{dp_w}{dt} = \frac{1.65\times10^7\,\mathrm{Pa} - 2.01\times10^7\,\mathrm{Pa}}{6\times10^7\,\mathrm{s} - 1\times10^7\,\mathrm{s}} = -0.072\,\mathrm{Pas}^{-1} \quad . \tag{5.24}$$

Then, employing Eq. (5.16), we get estimate the reservoir pore volume as

$$\phi V = -\frac{Q}{c_t \frac{dp_w}{dt}} = -\frac{1.16\times10^{-3}\,\mathrm{m^3/s}}{2.6\times10^{-9}\,\mathrm{Pa}^{-1}\cdot -0.072\,\mathrm{Pas}^{-1}} = 6.2\times10^6\,\mathrm{m^3} \quad . \tag{5.25}$$

	SPE Metric	SI
Q	$100\,\mathrm{m^3/d}$	$1.16\times10^{-3}\,\mathrm{m^3/s}$
h	10 m	10 m
ϕ	0.2	0.2
c_t	$2.6\times10^{-4}\,\mathrm{bar}^{-1}$	$2.6\times10^{-9}\,\mathrm{Pa}^{-1}$

Table 5.1: Basic data for example.

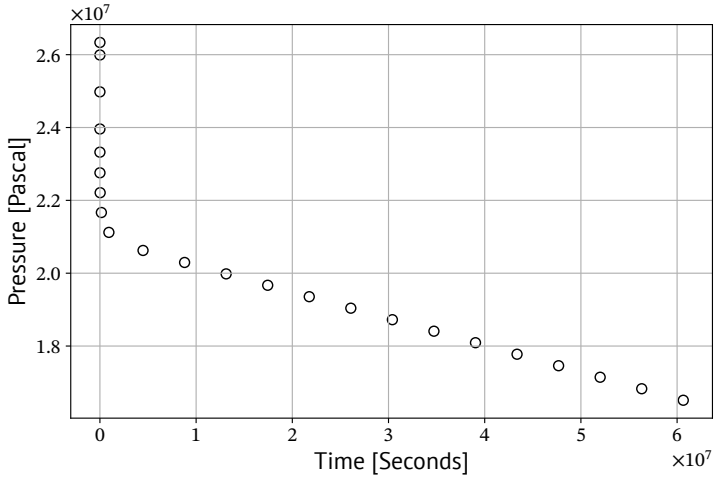


Figure 5.2: The pressure data from the drawdown test in a plot with Cartesian scales.

With the given porosity, this yields a reservoir volume of $V = 6.2 \times 10^6\,\mathrm{m}^3/0.2 = 3.1 \times 10^7\,\mathrm{m}^3$. For a cylindrical reservoir, were $V = \pi r_o^2 h$, this corresponds to an outer radius of

$$r_o = \sqrt{\frac{V}{\pi h}} = \sqrt{\frac{3.1 \times 10^7\,\mathrm{m}^3}{\pi 10\,\mathrm{m}}} \simeq 1000\,\mathrm{m} \quad . \tag{5.26}$$

5.3 Exact solution for cylindrical reservoir

There exist an exact expression for the well pressure in a cylindrical reservoir.[3] That is, a solution to the diffusivity equation with constant rate boundary conditions on inner radius r_w

$$\left.\frac{\partial p}{\partial r}\right|_{r=r_w} = \frac{p_c}{r_w} \quad , \tag{5.27}$$

and no flow on outer radius r_o

$$\left.\frac{\partial p}{\partial r}\right|_{r=r_o} = 0 \quad . \tag{5.28}$$

The late-time behavior of this solution may be analyzed to get the semi steady state well pressure (Eq. (5.14)):

Expressed in dimensionless variables ($r_{Do} = r_o/r_w$ and $t_D = \eta t/r_w^2$) the exact solution for the well pressure $p(r_w)$ when $r_o \gg r_w$ is

$$p_w = p_i - p_c\left(\frac{2t_D}{r_{Do}^2} + \ln(r_{Do}) - \frac{3}{4} + F(r_{Do}, t_D)\right) \quad , \tag{5.29}$$

where

$$F(r_{Do}, t_D) = 2\sum_{n=1}^{\infty} \frac{J_1^2(\alpha_n r_{Do})}{\alpha_n^2 (J_1^2(\alpha_n r_{Do}) - J_1^2(\alpha_n))} e^{-\alpha_n^2 t_D} \quad , \tag{5.30}$$

and α_n are roots of the equation

$$J_1(\alpha_n r_{Do}) Y_1(\alpha_n) - J_1(\alpha_n) Y_1(\alpha_n r_{Do}) = 0 \quad . \tag{5.31}$$

Inspecting the exact solution (5.29), we see that it is equal to the semi steady state solution (5.14) plus a time dependent correction, F.

[3] Everdingen and Hurst, "The Application of the Laplace Transformation to Flow Problems in Reservoirs."

Exact expression for the well pressure in a cylindrical reservoir

The correction is a sum over terms (modes) that fall off exponentially with time, so the late time behavior is described by the semi steady state solution as derived earlier. The longest living mode has time dependency $\exp(-\alpha_1^2 t_D)$, where α_1 is the smallest root. In Fig. 5.3 are plots of the function

The correction to semi steady state fall off exponentially with time.

$$f(x) = J_1(xr_{Do})Y_1(x) - J_1(x)Y_1(xr_{Do}) \tag{5.32}$$

(Eq. (5.31)) for different values of r_{Do}, and we we see that the smallest root is

$$\alpha_1 \approx \frac{4}{r_{Do}} \quad . \tag{5.33}$$

The time constant for the longest living mode is thus

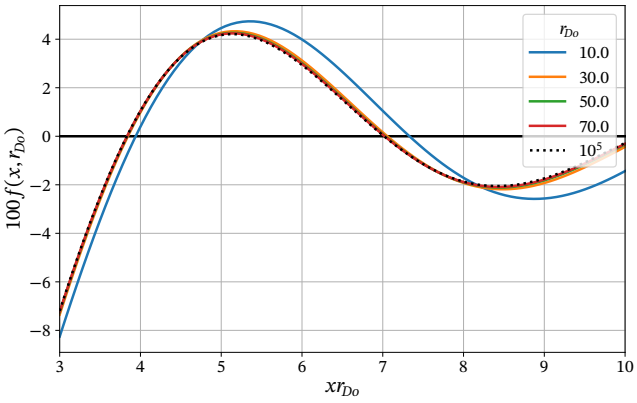


Figure 5.3: The function $f(x) = J_1(xr_{Do})Y_1(x) - J_1(x)Y_1(xr_{Do})$ for different values of r_{Do}. we see that the smallest root is $\alpha_1 \approx \frac{4}{r_{Do}}$.

$$\boxed{t_0 = \frac{r_o^2}{16\eta}} \quad . \tag{5.34}$$

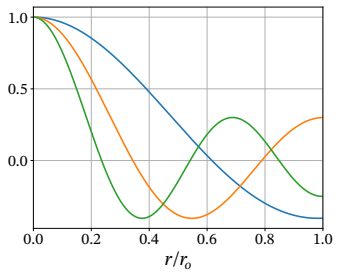


Figure 5.4: Spatial shape of the three longest living modes of correction to SSS solution,

Note the similarity with "time of investigation" and "radius of investigation" (Eq. (3.27)).

Figure 5.4 shows the spatial shape of the three longest living modes of the correction to the semi steady state profile. We see that the sum in Eq. (5.30) is similar to a Fourier expansion, and that the "high frequency" modes die off first.

5.4 Log–log derivative diagnostic plot

In well test analysis, the log–log plot of the logarithmic derivative, p', versus time, t, is extensively used for diagnostic purposes. This log–log derivative diagnostic plot is used in general to find flow regimes, and it will be discussed and used extensively in the following chapters. The plot has

$$\ln(p') = \ln\left(\frac{dp}{d\ln(t)}\right) \tag{5.35}$$

on the y–axis, and

$$\ln(t)$$

on the x–axis. An example diagnostic plot is shown in Fig. 5.5.

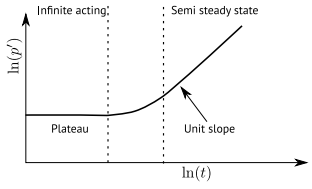


Figure 5.5: Log–log derivative diagnostic plot, showing infinite acting and semi steady state flow regimes.

Since details and variability are hidden, log–log plots can be deceptive, and it is often said that any data can be fitted to anything on a log–log plot. However, as will be demonstrated below, this removal of detail can also be set to good use.

From Eq. (3.58), the infinitely acting transient has the form

$$p_w = m\ln(t) + C \quad , \tag{5.36}$$

so the logarithmic derivative is a constant. Thus, the time interval for infinitely acting flow can be identified as a period with zero slope or a plateau value. Such a plateau is indicated in Fig. 5.5.

In semi steady state, the well pressure is linear in time (Eq. (5.14)),

$$p_w = mt + C \quad , \tag{5.37}$$

so the logarithmic derivative is

$\frac{dp}{d\ln(t)} = t\frac{dp}{dt}$

$$\ln(p') = \ln\left(\frac{dp}{d\ln(t)}\right) = \ln\left(t\frac{dp}{dt}\right) \tag{5.38}$$

$$= \ln(mt) = \ln(t) + \ln(m) \quad , \tag{5.39}$$

and the plot ($\ln(p')$ vs. $\ln(t)$) has unit slope. Thus, the the time interval for semi steady state flow can be can be identified as a period with unit slope. Such a unit slope period is indicated in Fig. 5.5.

In general, if a flow regime is characterized by by an exponent, α,

$$p_w = mt^\alpha + C \quad , \tag{5.40}$$

we have

$$\ln(p') = \alpha\ln(t) + \ln(\alpha m) \quad . \tag{5.41}$$

Thus, the time interval for a flow regime with characteristic exponent α can be identified as a period on the log–log diagnostic plot with slope $= \alpha$.

If we ignore the early time effects of wellbore storage and skin, the reservoir limit test has two flow regimes: infinitely acting radial flow and semi steady state flow. The first will be characterized by a time interval with zero slope, and the second will be characterized by an interval with unit slope. This is illustrated in Fig. 5.5.

As has been discussed in the previous chapters, permeability and skin are estimated based on fitting a straight line to the infinitely acting flow period on a a semilog plot (p_w vs. $\ln(t)$) as shown in Fig. 5.6.

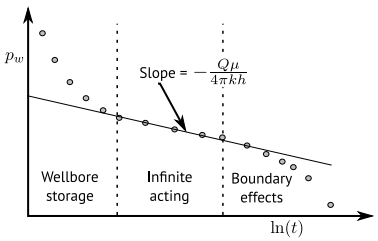


Figure 5.6: When analyzing a reservoir limit test a semilog plot (p_w vs. $\ln(t)$) is used to find permeability and skin

Reservoir pore volume and shape factor is found from the semi steady state flow period using a Cartesian plot (p_w vs. t). This is illustrated in Fig. 5.7. If the straight line fit is

$$p_w = p_0 - mt \quad , \tag{5.42}$$

then the reservoir volume is estimated from the slope m:

Estimating reservoir volume

$$\boxed{\phi V = -\frac{Q}{c_t m}} \quad . \tag{5.43}$$

In a reservoir with constant thickness, the reservoir area is

$$A = \frac{V}{h} \quad , \tag{5.44}$$

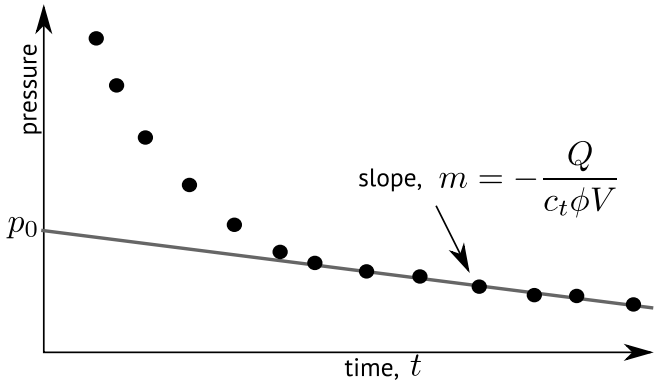


Figure 5.7: A cartesian plot (p_w vs. t) is used to find reservoir volume and shape factor

so, if permeability and skin is known, the Dietz shape factor may be found by extrapolating the straight line (Eq. (5.42)) to $t = 0$ and solving Eq. (5.20) for C_A:

Estimating the shape factor

$$\boxed{\ln(C_A) = \ln\left(\frac{4A}{r_w^2}\right) - \gamma + 2S - 2\frac{p_i - p_0}{p_c}} \quad . \tag{5.45}$$

5.5 Reservoir monitoring with buildup tests

In this section we will show that the buildup test can be used for monitoring reservoir pressure by employing an extended version of the Horner analysis. In the strict Horner analysis (page 40), valid for short production times, t_p, the extrapolated pressure at $\frac{t_p+\Delta t}{\Delta t} = 1$, p^*, corresponds to the initial pressure. Due to the short production time, the initial pressure is approximately equal the average reservoir pressure. For longer production times, p^* is no longer equal to the average reservoir pressure, but the straight line extrapolation can still be used for estimating this pressure.

There are two methods for estimating the average reservoir pressure for buildup tests: In the Ramey–Cobb method, which is applicable for long production times (semi steady state), a time is found where the pressure on the straight line correspond to the average pressure, and in the Matthews-Brons-Hazebroek method, which is universally applicable, a correction to p^* is found. Both methods require knowledge of the reservoir shape.

We have seen (page 48) that irrespective of the length of the production time, t_p, the radial transient buildup is approximately the mirror image of drawdown provided that drawdown time t is replaced by the effective (Agarwal) time

$$t_e = \frac{t_p \Delta t}{t_p + \Delta t} = \frac{t_p}{\tau} \quad . \tag{5.46}$$

Here $\tau = (t_p + \Delta t)/\Delta t$ is the Horner time. Remember that infinite time $\Delta t \to \infty$ yields $\tau \to 1$, thus $\ln(\tau) \to 0$.

Using dimensionless variables, the buildup response (4.17) is then

$$p_{Dw}(t_p) - p_{Dw}(t_p + \Delta t) = \frac{1}{2}\left(\ln(4t_{Dp}) - \ln(\tau) - \gamma + 2S\right) \quad . \tag{5.47}$$

This implies that the Horner analysis can be extended to long production periods to get estimates for permeability (from the slope) and skin as shown in Fig. 5.8. Permeability is estimated from the slope, m:

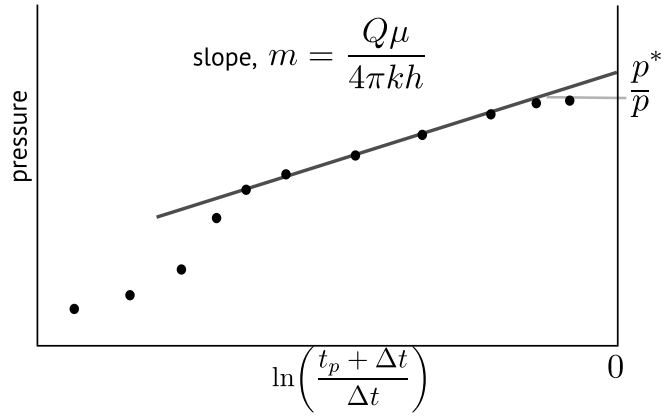


Figure 5.8: Extending the Horner analysis. Note that the x-axis is reversed in this plot, this is often the case for Horner plots as it makes time run from left to right.

$$\boxed{k = \frac{Q\mu}{4\pi h}\frac{1}{m}} \quad . \tag{5.48}$$

Extrapolation of the straight line to $\tau = 1$ defines the pressure p^*. And, with known permeability, skin can be found using pressure difference at any point on the straight line. If we use the extrapolated pressure the expression is

$$\boxed{S = \frac{1}{2}\left[\frac{p^* - p(t_p)}{m} - \ln(4t_{Dp}) + \gamma\right]} \quad . \tag{5.49}$$

We will now derive the Ramey–Cobb method for estimating average reservoir pressure: First, remember from Eq. (5.13) that $\overline{p}(t) = p_i - Qt/(c_t\phi V)$. Then the dimensionless average reservoir pressure $\overline{p}_D$ is

$$\overline{p}_D(t) = \frac{p_i - \overline{p}(t)}{p_c} = \frac{Q}{c_t\phi V}\frac{2\pi kh}{Q\mu}t = \frac{2\pi\eta}{A}t = \frac{2\pi}{A_D}t_D \tag{5.50}$$

If flow is in semi-steady-state at end of the production period (see Eq. (5.20)) we have

$$p_{Dw}(t_p) = \frac{2\pi}{A_D}t_{Dp} + \frac{1}{2}\left[\ln\left(\frac{4A_D}{C_A}\right) - \gamma + 2S\right] \tag{5.51}$$

$$= \overline{p}_D(t_p) + \frac{1}{2}\left[\ln\left(\frac{4A_D}{C_A}\right) - \gamma + 2S\right] \quad . \tag{5.52}$$

Due to shut in after t_p, we have $\overline{p}_D(t) = \overline{p}_D(t_p)$ for $t > t_p$, and can thus write just $\overline{p}_D$ for all $t > t_p$. If we insert Eq. (5.52) into the expression for the linear region of the Horner plot (Eq. (5.47)) and solve for $\overline{p}_D$ we get

$$\overline{p}_D = p_{Dw}(t_p + \Delta t) - \frac{1}{2}\ln\left(\frac{A_D}{C_A t_{Dp}}\tau\right) \tag{5.53}$$

We see that by selecting a time such that

$$\tau = C_A\frac{t_{Dp}}{A_D} = C_A t_{Da} \tag{5.54}$$

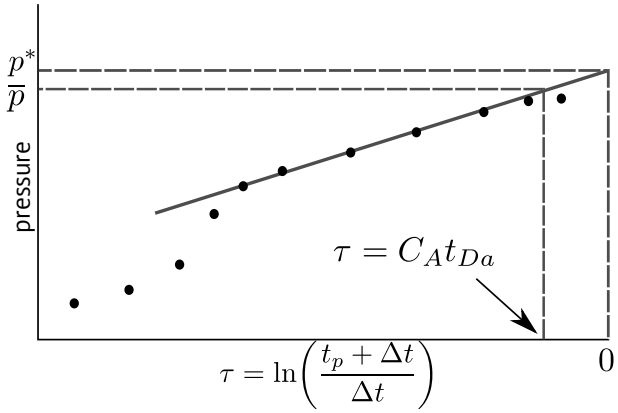


Figure 5.9: Ramey–Cobb method: A time is selected on the straight line such that the corresponding pressure is $\overline{p}$.

the logarithmic term vanish and the corresponding pressure is the average reservoir pressure.

The Ramey–Cobb method is illustrated in Fig. 5.9, and can be summarized as follows: First fit a straight line to the infinitely acting radial transient part of the Horner plot

$$p = p^* - m \ln(\tau) \quad .$$

Then, using the Dietz shape factor that correspond to the actual reservoir shape, determine

$$\tau^* = \frac{C_A}{A_D} t_{Dp} \quad . \tag{5.55}$$

The corresponding pressure on the straight line is the average reservoir pressure:

$$p(\tau^*) = p^* - m \ln(\tau^*) = \overline{p} \quad . \tag{5.56}$$

Note that in order to apply this method, permeability, and reservoir area and shape, must be known from a separate analysis.

The Ramey–Cobb method is only applicable if the reservoir has reached semi steady state before shut in. We see from Eq. (5.56) that the Ramey–Cobb method alternatively may be expressed as a correction to p^*, and in the Matthews–Brons–Hazebroek (MBH) method, an expression for this correction is sought that is valid also for production times shorter than the time needed to reach steady state. A general explicit expression for the correction does not exist, but if the reservoir shape and area is known, the correction can be found by solving drawdown–buildup in dimensionless form for a given geometry. The correction has been tabulated for a number of simple geometries, and may be found by solving the flow numerically for more complex geometries. Fig. 5.10 shows four examples. The correction is a function of dimensionless time and area through the time variable $t_{Da} = \frac{t_{Dp}}{A_D}$.

Since both the Ramey–Cobb and the MBH method can be expressed as a correction to the extrapolated pressure, there should be a connection between the two. We see from Fig. 5.10 that the MBH correction is linear in $\ln(t_{Da})$ for large production times. Large times correspond

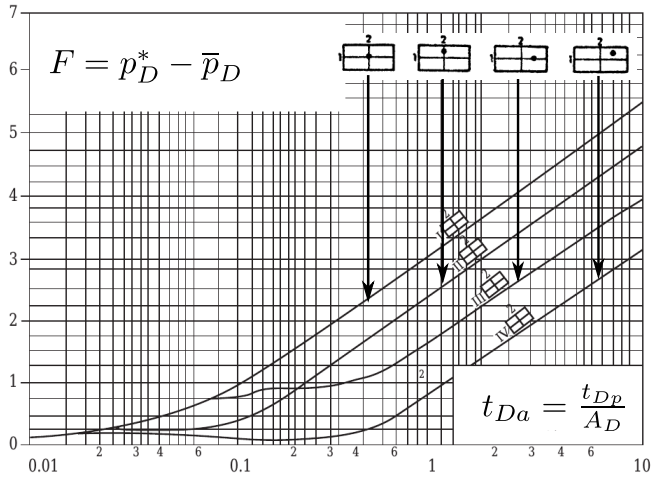


Figure 5.10: Matthews-Brons-Hazebroek correction. (© SPE, 1977, after Earlougher, R. Advances in Well Test Analysis)

to semi steady state, which is where the Ramey–Cobb method is applicable, and we see from Eqs. (5.55) and (5.56) that this linear behavior is consistent when the MBH correction for large t_p is

MBH correction for large t_p is a function of C_A

$$\begin{aligned} F &= \frac{1}{2}\ln\left(\frac{C_A}{A_D}t_{Dp}\right) \\ &= \frac{1}{2}\ln(C_A) + \frac{1}{2}\ln\left(\frac{t_{Dp}}{A_D}\right) \end{aligned} \tag{5.57}$$

We see from Eq. (5.57) that all MBH correction curves have the same slope (1/2), and that the offset is half the logarithm of the Dietz shape factor, C_A[4].

[4] In the paper where the Dietz shape factor were first introduced, it was actually defined from Eq. (5.57).

The Horner analysis is based on a constant production rate over a certain time, and all results are expressed in terms of this production time t_p. For cases where the production has been varying, we have seen earlier that we may use an effective production time (Eq. (4.20)) instead, as long as there is a stable period just before shut in. Another complication is that for long production times we will in Eqs. (5.49) and (5.57) need to subtract two large numbers; this will introduce an increasingly large numeric error for increasing t_p. Luckily, it can be shown that for times larger than the time needed to reach semi steady state, t_{SSS}, the results are independent of the choice of t_p as long as $t_p \geq t_{SSS}$. This is due to the fact that p^* depends linearly on the choice of t_p when $\Delta t \ll t_p$. We should therefore preferably use $t_p = t_{SSS}$ whenever the production time is longer than the time to reach semi steady state.

For long production times: use $t_p = t_{SSS}$.

5.6 Drainage areas

In our analysis we have assumed that there is only one well in the reservoir, and the question of whether any of this is applicable to situations with more than one well obviously arises. The answer to this lies partly in the concept of drainage areas: A well test in a well in a multi well reservoir can often be analyzed in terms of a single well in a reservoir shaped like the wells drainage area.

In general each wells drainage area is defined in terms of streamlines. The streamlines are defined by the fluid flow vectors, and are coupled to the pressure gradients via Darcys law. The streamlines end in wells, and space is divided into regions where flow is towards different wells. These regions are called drainage areas, and in general the size and shape of these areas change over time. Each producer will define its own drainage area, while injectors may divide its flow between several producers, and a producers drainage area may contain (parts of) several injectors.

In a reservoir with only producers producing at constant rates, a semi steady state develops where drainage areas are constant in time, and the pore volume of each area is proportional to the production rate. Each drainage area has the same semi steady state pressure profile, and average pressure, as a corresponding single well reservoir with no-flow boundaries. In this case a buildup test can be analyzed using the Horner plot. The calculation of average pressure should be based on the shape and area of the drainage area at shut in, and the resulting pressure estimate will be an average of pressure in the drainage area.

Note that the drainage area concept has limited applicability, and that in general the analysis of a build up well test in a multi well reservoir is best performed in terms of some sort of desuperposition (see page 47).



Figure 5.11: Example of streamline pattern that partition the reservoir into drainage areas. There is one drainage area for each producer.

5.7 Reservoir pressure vs. local pressure

The MBH and Ramey–Cobb methods provide estimates for average pressure in a reservoir region or drainage area. In terms of conditioning reservoir models to monitoring data[5], this may actually not be what is most useful. The two methods also require knowledge of the reservoir shape, which sometimes is among the unknown reservoir properties the monitoring data is supposed to contribute in determining. For the conditioning of reservoir models the local pressure in the near well region may be more relevant. The corresponding measurement is the well pressure at a fixed time after shut-in This measurement is often referred to as “one hour shut-in pressure”, but the actual relevant time does depend on permeability (radius of investigation).

[5] Conditioning of reservoir models to time dependent data, such as measured pressure, is often referred to as “history matching”.

For the conditioning of reservoir models the local pressure near the well is most relevant. In a reservoir simulation model pressure is defined in grid-blocks, and flowing pressure near a well is represented by the pressure in the block where the well is perforated. This grid-block pressure is equal to the pressure at Peaceman equivalent well-block radius[6]

$$r_e \approx 0.2L \quad , \tag{5.58}$$

where L is the linear block size. The concept of an equivalent radius is illustrated in Fig. 5.12: The flow into a grid block with a well is determined by the pressure difference between an upstream block and the grid-block pressure. This is a linear pressure profile, while the real

[6] D. W. Peaceman. “Interpretation of Well-Block Pressures in Numerical Reservoir Simulation.” In: *Society of Petroleum Engineers Journal* 18.03 (June 1978), pp. 183–194. DOI: 10.2118/6893-PA.

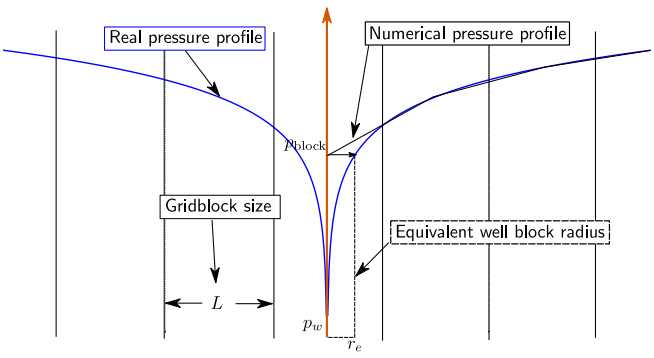


Figure 5.12: The Peaceman equivalent well-block radius

profile towards the well is a logarithmic singularity. As a result, well pressure is lower than well-grid-block pressure, and the distance from the well at which reservoir pressure is equal to grid-block pressure is the equivalent well-block radius.

What is the time it takes for well pressure to reach flowing pressure at Peaceman equivalent well-block radius $r_e \approx 0.2L$? The flowing pressure at r_e is given by the steady state profile (2.40)

$$p(r_e, t) = p_w(t) + p_c S + p_c \ln\left(\frac{r_e}{r_w}\right) \quad , \tag{5.59}$$

and the shut-in well pressure at time $t + \Delta t$ is (MDH approximation, Eq. (4.30))

$$p_w(\Delta t) = p_w(t) + \frac{p_c}{2}\left[\ln\left(\frac{4\eta\Delta t}{r_w^2}\right) - \gamma + 2S\right] \quad . \tag{5.60}$$

By combining Eq. (5.59) and (5.60), and solving for Δt we see that the time after shut in at which the well block pressure es equal to flowing grid block pressure is

Time at which shut-in pressure is equal to flowing grid-block pressure.

$$\boxed{\Delta t = e^{\gamma}\frac{r_e^2}{4\eta} \approx 0.018\frac{L^2}{\eta}} \quad . \tag{5.61}$$

This is the time when shut in pressure should be measured so that it can be compared with simulated grid block pressure for conditioning.

6
Reservoir boundaries

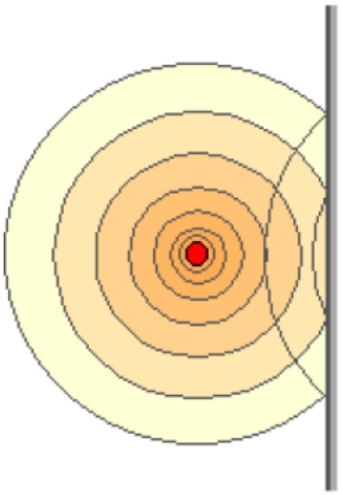


Figure 6.1: Pressure signal reflected at reservoir boundary

In this chapter we will discuss how well testing can detect reservoir boundaries and heterogeneities.

As shown in Fig. 6.1, pressure signals are reflected at reservoir boundaries, and these reflections can, when measured at the well, be used to infer quantities such as distance to barriers and reservoir shape.

Examples of situations where well test data can offer valuable information are shown in Fig. 6.2. The well test data can be analyzed quantitatively to get estimates for the distance to reservoir boundaries, the distance to and the strength of an aquifer, the distance to a gas cap, the distance to an advancing water front, and the shape and size of sand bodies.

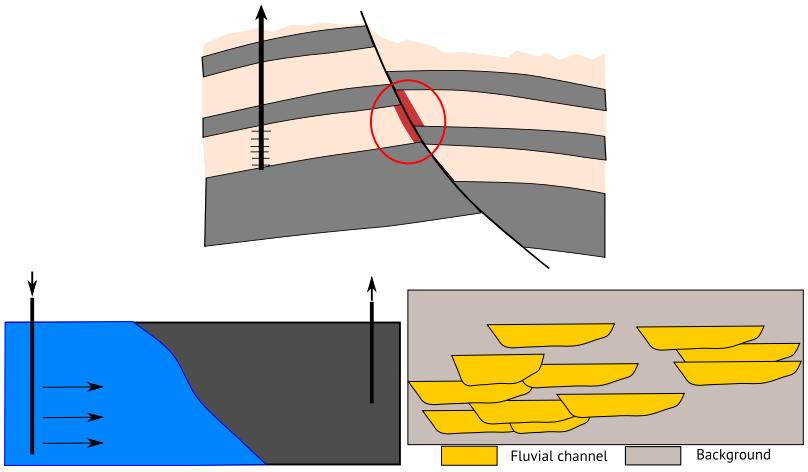


Figure 6.2: Examples of boundary like reservoir features that may be probed in a well test: A fault (top), a water injection front (bottom left), and shape of sand bodies (bottom right)

The data can also give qualitative information relating to the nature of the reservoir and the flow in the near well region. For the latter purpose, the derivative diagnostic plot briefly introduced on page 56 is particularly useful, and several examples of its use will be shown.

6.1 Well close to a linear boundary

The pressure response in a well close to linear boundary can be found using superposition in space. The method is called the method of images, since the boundary condition at a barrier or reservoir boundary

may be satisfied by placing imaginary image wells outside the reservoir area as shown in Fig. 6.3. The sum of the unconstrained pressure

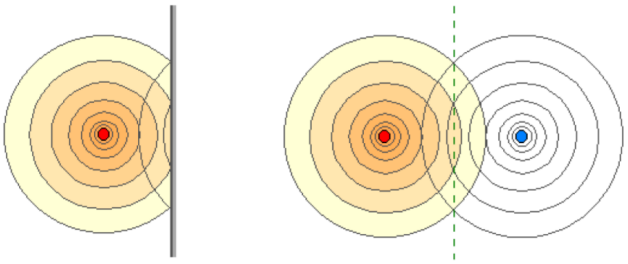


Figure 6.3: Method of images: Imaginary image wells are placed outside the reservoir in order to satisfy the boundary conditions.

field from the real well and the image wells should satisfy the boundary condition, and as shown in Fig. 6.4; the no-flow boundary condition is obtained by placing an image well with the same rate, while a

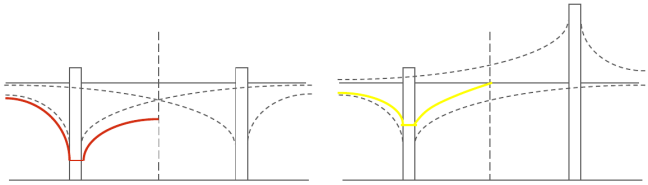


Figure 6.4: Method of images for no–flow and constant–pressure boundary condition. For the red and yellow pressure curves, their difference to the initial pressure are given by the sum of the difference between the dashed curves and the initial pressure.

constant pressure boundary condition is obtained by placing an image well with opposite rate.

The pressure response in a well close to a single linear boundary, such as a sealing fault, can be derived by the method of images: The boundary condition is satisfied by placing an image well with the same rate on the other side of the boundary as shown in Fig. 6.5.

The well pressure in a constant rate drawdown test is the sum of two infinitely acting terms, one from the real well, and another from the image well. We will ignore the short time effects of wellbore storage and skin, so we can use the logarithmic approximation for the real well, as given by Eq. (3.29):

$$p_i - p_w(t) = \frac{p_c}{2}\left(\ln\left(4\eta\frac{t}{r_w^2}\right) - \gamma + 2S\right) \quad . \tag{6.1}$$

The distance to the image well is large compared to the well radius, so this contribution is given by the exponential integral at all times, as in Eq. (3.18):

$$p_i - p(r,t) = \frac{1}{2}p_c\,\mathrm{E}_1\left(\frac{1}{4\eta}\frac{r^2}{t}\right) \quad . \tag{6.2}$$

For radius $r = 2L$, this gives:

$$p_i - p(2L,t) = \frac{1}{2}p_c\,\mathrm{E}_1\left(\frac{1}{\eta}\frac{L^2}{t}\right) \quad . \tag{6.3}$$

Employing the superposition principle in space to add the pressure equations (6.1) and (6.3), we obtain the well pressure as:

$$p_w(t) = p_i - \frac{p_c}{2}\left[\left(\ln\left(\frac{4\eta}{r_w^2}t\right) + 2S - \gamma\right) + \mathrm{E}_1\left(\frac{L^2}{\eta t}\right)\right] \quad . \tag{6.4}$$

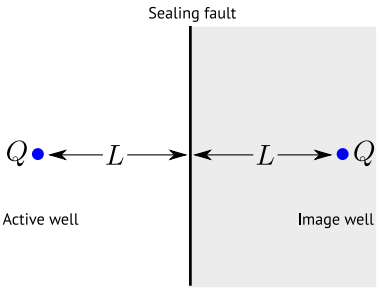


Figure 6.5: A well close to a linear boundary, modelled using an image well on the other side of the boundary

Note that the skin simply adds an extra contribution to the well pressure, so there is no skin contribution from the image well. We may write Eq. (6.4) in dimensionless form:

$$p_D(t_D, L_D) = \frac{1}{2}\left[\ln(4t_D) - \gamma + 2S + \mathrm{E}_1\left(\frac{L_D^2}{t_D}\right)\right] \quad . \tag{6.5}$$

When $t_D \to 0$, then $L_D^2/t_D \to \infty$, so $\mathrm{E}_1(L_D^2/t_D) \to 0$. This reflects that at early times the reflected signal has not reached the well, thus the exponential integral contribution is zero:

$$p_D(t_D, L_D) = \frac{1}{2}\left(\ln(4t_D) - \gamma + 2S\right) \quad , \tag{6.6}$$

which will give a slope of half when plotting p_D and t_D on a semi-log plot.

At late times, when the reflection has passed the well, the exponential integral may be approximated by a logarithm:

$$\begin{aligned} p_D(t_D, L_D) &= \frac{1}{2}\left[\left(\ln(4t_D) - \gamma + 2S\right) + \left(\ln\left(\frac{t_D}{L_D^2}\right) - \gamma\right)\right] \\ &= \ln\left(\frac{2}{L_D}t_D\right) - \gamma + S \quad . \end{aligned} \tag{6.7}$$

We observe that this gives a slope of half when plotting p_D and t_D on a semi-log plot. The fault will therefore manifest itself as a doubling of slope on a semilog plot, going from a slope of half at early times to a slope of 1 at later times. Note that if the fault is very close to boundary, the line with the first slope will be hidden by wellbore and near wellbore effects on one side and the transition to the second slope on the other, so that we will only see a single straight line. This may the be wrongly be interpreted as a reduced permeability.

A fault manifests itself as a *doubling of slope* on a semilog plot.

As illustrated in Fig. 6.6, the distance to the fault can be found from the time of crossing of the two fitted straight lines (Eqs. (6.6) and (6.7)):

$$\frac{1}{2}\ln(4t_{Dx}) - \frac{1}{2}\gamma = \ln\left(\frac{2}{L_D}t_{Dx}\right) - \gamma \quad . \tag{6.8}$$

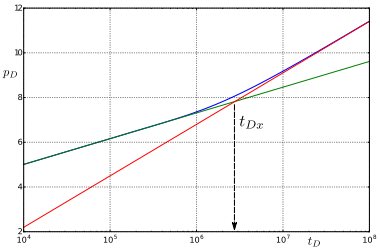


Figure 6.6: The distance to the fault can be found from the time of crossing of the two fitted straight lines

Solving Eq. (6.8) for L gives

$$\boxed{L_D = e^{-\frac{\gamma}{2}}\sqrt{t_{Dx}}, \text{ or } L = 0.749\sqrt{\frac{kt_x}{\mu\phi c_t}}} \tag{6.9}$$

The pressure response in a well close to a corner can also be solved in terms of image wells, as shown in Fig. 6.7.

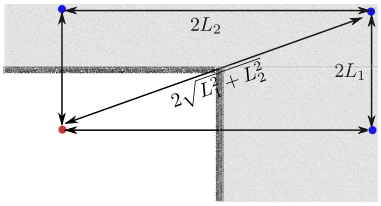


Figure 6.7: A well in a corner, and the corresponding image wells

In this case three image wells are needed to satisfy the no-flow boundary conditions along the two reservoir walls, and the expression for well pressure has four contributions:

$$\begin{aligned} p_D(t_D, L_{D1}, L_{D2}) = \frac{1}{2}\Bigg[&\left(\ln(4t_D) - \gamma + 2S\right) \\ &+ \mathrm{E}_1\left(\frac{L_{D1}^2}{t_D}\right) + \mathrm{E}_1\left(\frac{L_{D2}^2}{t_D}\right) + \mathrm{E}_1\left(\frac{L_{D1}^2 + L_{D2}^2}{t_D}\right)\Bigg] \end{aligned} \quad . \tag{6.10}$$

At early times, the contribution from the image wells are again zero, and the well pressure is given by Eq. (6.6), while at late times the exponential integrals may be approximated by logarithms:

$$p_D(t_D, L_{D1}, L_{D2}) = 2\ln(t_D) + \ln\left(\frac{2}{L_{D1}L_{D2}\sqrt{L_{D1}^2 + L_{D2}^2}}\right) - 2\gamma + S \quad . \tag{6.11}$$

Thus, the straight angled corner will manifest itself as a four times increase of the slope on a semilog plot[1].

[1] In general, if the corner has angle θ the slope will increase by a factor $\frac{2\pi}{\theta}$.

Similar to the situation with a single fault, if the well is close to the corner we may only see a single straight line, and this can wrongly be interpreted as a reduced permeability. On the other hand, if the distance to the two reservoir walls are well separated $L_2 \gg L_1$, we will see three straight lines: The first representing the infinitely acting radial flow, a second with double slope representing the semi radial flow due to the reflection from the nearest wall, and the third with four times the slope.

6.2 Flow regimes – Diagnostic plots

Until now we have seen two fundamental flow types or flow regimes: radial flow, which is characterized by a linear slope on a semilog plot and a constant value on the log–log derivative plot, and depletion, which is characterized by a unit slope on the log–log derivative plot. The unit slope is seen early in the test when all production is from the wellbore (wellbore storage effect, see Eq. (3.69)), and late for semi steady state flow (Eq. (5.20)).

In this section we will discuss various flow regimes that can be seen in a well test, and their signatures. A constant rate well test probes the volume around the well at an increasing distance from the well, consistent with the concept of a radius of investigation, and the derivative of the pressure response reflects the properties at the pressure front. The test probes the volume in the transition zone between the essentially semi steady state region closer to the well and the undisturbed outer regions, as illustrated in Fig. 3.6 on page 29. Thus, the early part of the test reflects properties and front movement close to the well, while the later parts reflect front propagation and properties at increasingly larger distances.

As illustrated in Fig. 6.8, the time periods of a well test are typically characterized as: “early time”, dominated by wellbore effects, skin, and near well heterogeneities, “middle time”, where the flow has not yet seen the whole reservoir, and “late time”, where flow is boundary dominated or in semi steady state.

Identifying flow regimes

Flow regimes are identified using the log–log derivative diagnostics plot introduced on page 56. This plot has

$$\ln(p') = \ln\left(\frac{d}{d\ln(t)}p\right)$$

on the y–axis, and $\ln(t)$ on the x–axis. If the pressure response have

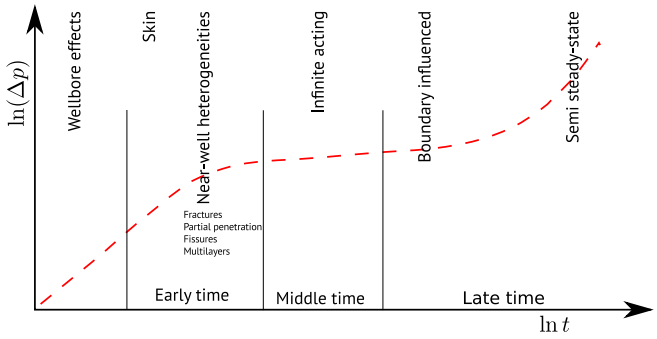


Figure 6.8: Flow periods on a log–log plot

the form $p_w = a - bt^{\alpha}$ then we have

$$\ln(p') = \ln(b\alpha) + \alpha \ln(t) \quad .$$

Thus, the time interval for a flow regime with characteristic exponent α can be identified as a period on the log–log diagnostic plot with slope $= \alpha$. We will see below that the characteristic exponent depend on the dimension in which the pressure front is propagating.

6.2.1 Spherical flow

When the pressure front propagates in three dimensions we have spherical flow. Two examples of a situation where we may see a flow period with a spherical flow regime is shown in Fig. 6.9: If the well

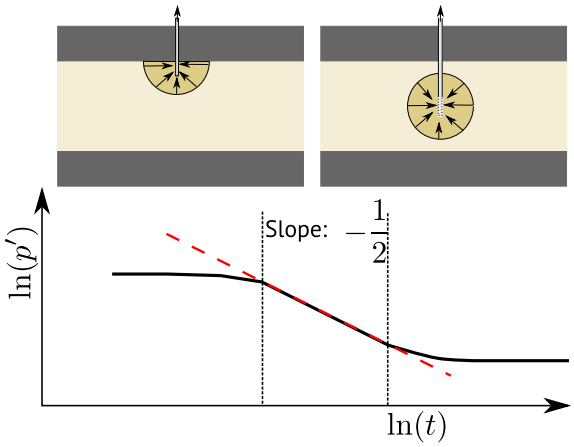


Figure 6.9: Examples of spherical flow due to an incompletely perforated reservoir zone

is only partially perforated in a reservoir zone, there will be a period where the pressure front propagates in a spherical or hemispherical pattern until it reaches the top and bottom of the zone.

For spherical flow we have

$$p(t) \propto \frac{1}{\sqrt{t}} = t^{-\frac{1}{2}} \quad , \tag{6.12}$$

which gives

$$\ln\left(\frac{d}{d\ln(t)}p\right) = -\frac{1}{2}\ln(t) + C \quad , \tag{6.13}$$

thus the slope on the derivative plot will be $-1/2$.

6.2.2 Radial flow

We have seen earlier that for radial flow, where the pressure front moves in a 2-dimensional radial pattern, the pressure has a characteristic logarithmic time behavior:

$$p(t) = a + m\ln(t) \quad , \tag{6.14}$$

which gives the derivative

$$\frac{d}{d\ln(t)}p = m \quad . \tag{6.15}$$

The plateau height corresponds to the constant slope on a semi-log plot, and depends on permeability and geometry.

Several examples of radial flow are shown in Fig. 6.10.

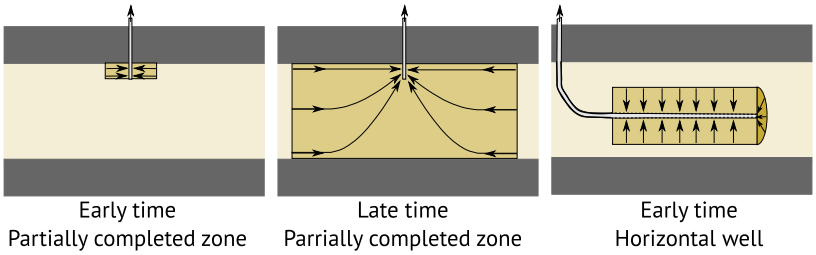


Figure 6.10: Examples of radial flow

We have seen the signature of a well test with a single radial flow period several times already, and Fig. 6.11 illustrates how this signature is affected by permeability, while Fig. 6.12 illustrates how this signature is affected by skin.

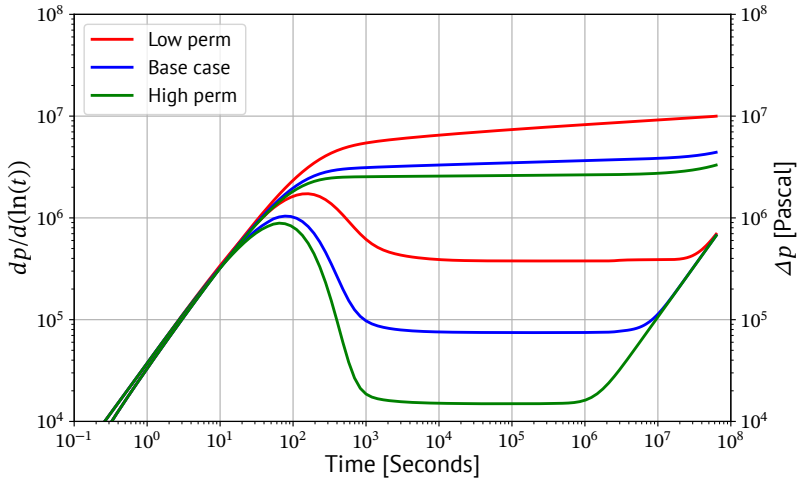


Figure 6.11: How permeability effects the radial flow diagnostic plot.

6.2.3 Linear flow

When the pressure front propagates in an essentially one dimensional pattern we have linear flow. Examples of situations with linear flow periods are flow in narrow, channel shaped, reservoirs (see page 72),

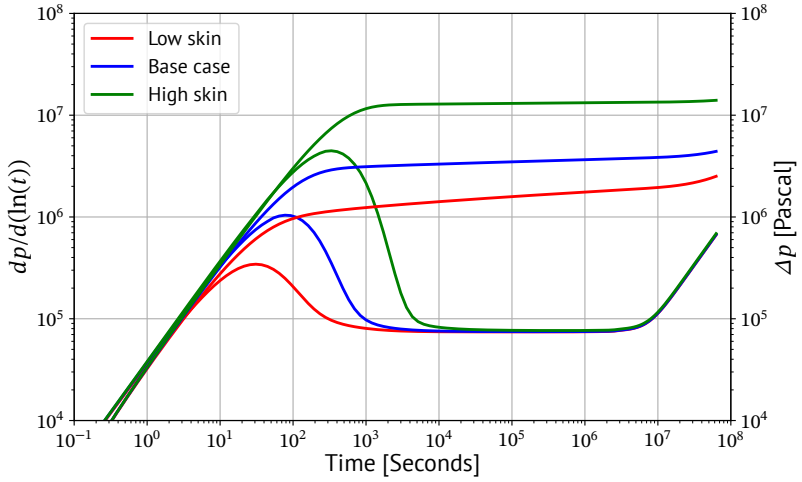


Figure 6.12: How skin effects the radial flow diagnostic plot.

and flow in hydraulically induced fractures (see page 87). Channel flow occur at middle to late times, while early time linear flow is indicative of fractures.

Linear flow has the following characteristic (see page 92):

$$p(t) \propto \sqrt{t} = t^{1/2} \quad , \tag{6.16}$$

which give the derivative

$$\ln\left(\frac{d}{d\ln(t)}p\right) = \frac{1}{2}\ln(t) + C \quad , \tag{6.17}$$

thus this flow regime is characterized by a slope of a half on the derivative plot. Figure 6.13 illustrates how channel width influence the corresponding derivative plots. This will be discussed in more detail later.

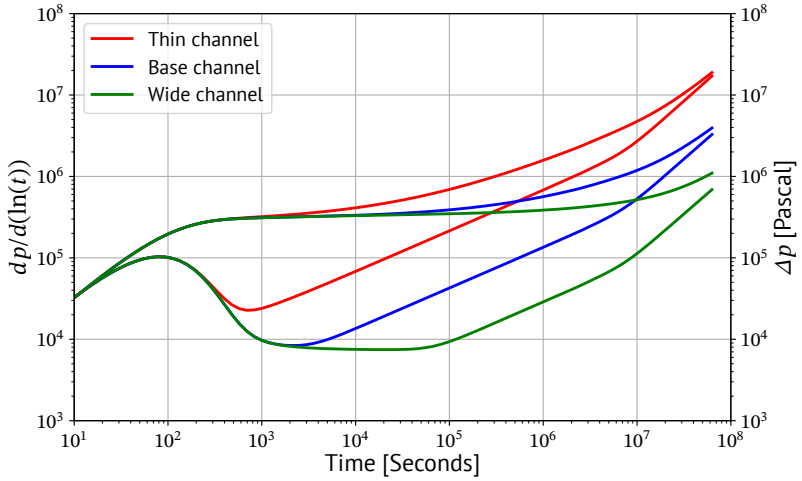


Figure 6.13: Derivative plots for channels width different width.

6.2.4 Summary of flow regimes

Each flow regime is identified by a time period with a characteristic slope on the log–log derivative diagnostic plot. Between each pe-

riod there will be a transition period, typically covering more than a decade. Two subsequent flow regimes may be of different or similar type. The sequence of flow periods is called a fingerprint, and galleries of these are called fingerprint libraries. An example of part of such a library is shown in Fig. 6.14.

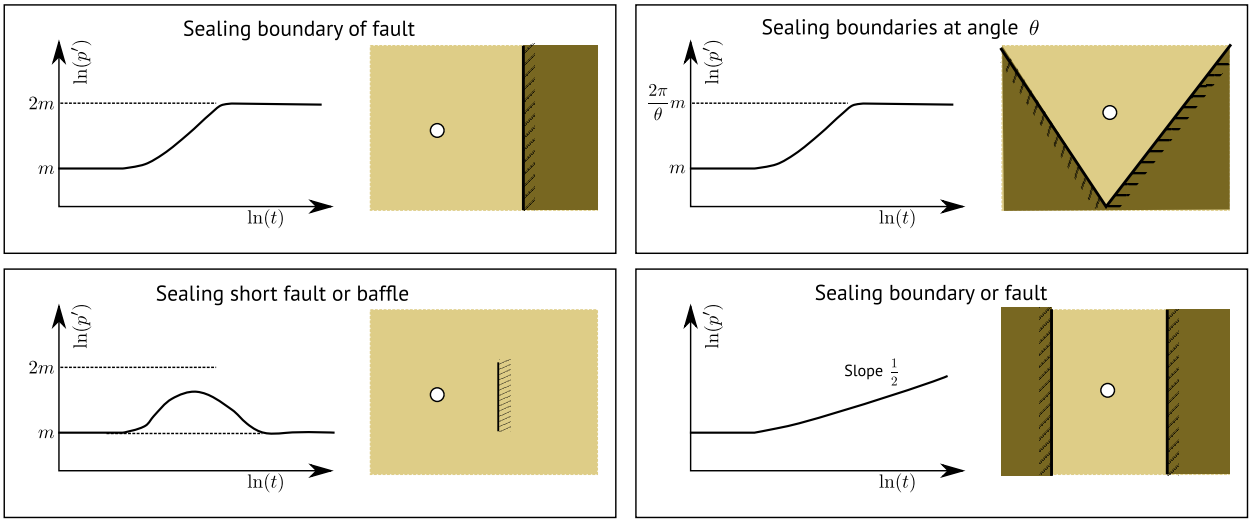


Figure 6.14: Examples of fingerprints from a fingerprint library.

There is a close relation between the dimension in which the pressure front spreads and the slope in the log–log derivative diagnostic plot over the corresponding time period: If the front spreads in d dimensions, then the slope will be $1 - d/2$. This relationship is summarized in Table 6.1.

Flow regime	dimensionality d	slope $1 - d/2$	
Spherical	3	$-\frac{1}{2}$	
Radial	2	0	
Bilinear	1½	$\frac{1}{4}$	Finite-conductive fractures
Linear	1	$\frac{1}{2}$	
Depletion	0	1	

Table 6.1: The connection between flow dimensionality and slope in the log–log derivative diagnostic plot.

6.3 Channel sands and narrow fault blocks

In this section we will investigate systems with middle-time linear flow, that is systems with channelized flow. Examples of such reservoirs are systems of tilted fault blocks that form narrow rectangular compartments as illustrated in Fig. 6.15. Another example are systems of stacked channels forming channel belts in a low-permeable background. These channels form narrow compartments of sand as illustrated in Fig. 6.16.

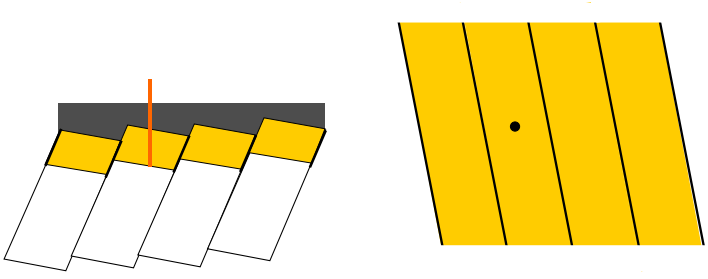


Figure 6.15: A system of tilted fault blocks forming narrow rectangular compartments.

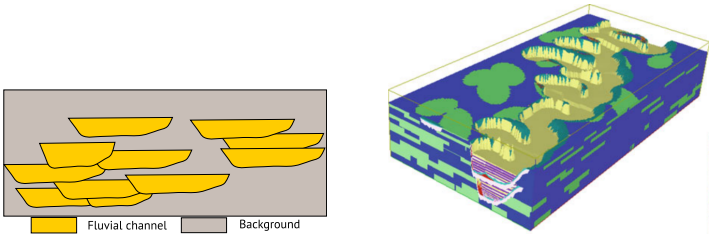


Figure 6.16: Stacked channel sands in a low-permeable background. Narrow compartments of sand are formed at low sand/background ratios.

A system with two parallel boundaries can be analyzed using superposition. As shown in Fig. 6.17 an infinite number of images are needed in this case. The first flow regime, valid for times where the radius of investigation is shorter than the distance to the nearest wall, is radial flow:

$$p_D = \frac{1}{2}\left[\ln(4t_D) - \gamma + 2S\right] \quad . \tag{6.18}$$

At late times, when the distance to the pressure front is much larger than the channel width, we have linear flow

$$p_D = \frac{2}{W_D}\sqrt{\pi t_D} + \sigma + S \quad , \tag{6.19}$$

where $W_D = W/r_w$ is the dimensionless channel width, and σ is pseudoskin, which is due to limited entry as illustrated in Fig. 6.18.

As long as $L \gg r_W$, the pseudoskin is[2],[3]

$$\sigma = \ln\left(\frac{W_D}{2\pi \sin\left(\pi\frac{L}{W}\right)}\right) \quad , \tag{6.20}$$

where L is the distance from the well to the nearest boundary. We will later see that a similar expression for pseudoskin (Eq. (7.17)) is important for the understanding of the productivity of horizontal wells.

As shown in Fig. 6.19, the derivative plot for a channel system will have a plateau, characteristic of radial flow, at early times, and a line with slope 1/2 for later times. The radial flow period is used to get estimates for permeability and skin, and the channel width and pseudoskin can be found based on a fitted straight line on pressure versus $\sqrt{t}$ plot. We see from Eq. (6.19) that the slope, m, of the straight line is

$$m = \frac{Q}{Wh}\sqrt{\frac{\mu}{\pi k \phi c_t}} \quad , \tag{6.21}$$

which gives

$$\boxed{W = \frac{1}{m}\frac{Q}{h}\sqrt{\frac{\mu}{\pi k \phi c_t}}} \quad , \tag{6.22}$$

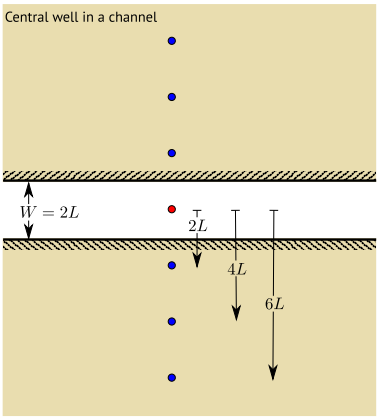


Figure 6.17: A well between to parallel boundaries and its images

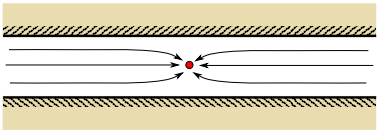


Figure 6.18: Linear flow into a well in a channel. The convergence of streamlines towards the well result in an increased pressure drop compared to fully linear flow.

[2] M. S. Hantush and C. E. Jacob. "Non-steady green's functions for an infinite strip of leaky aquifer." In: *Eos, Transactions American Geophysical Union* 36.1 (1955), pp. 101–112. DOI: 10.1029/TR036i001p00101.

[3] Madhi S Hantush. "Hydraulics of wells." In: *Advances in hydroscience* 1 (1964), pp. 281–432.

and that the pseudoskin is

$$\sigma = (p_i - p^*)\frac{2\pi kh}{Q\mu} - S \quad , \tag{6.23}$$

where p^* is the extrapolated straight line pressure at $t = 0$. Actual pseudoskin depends on reservoir heterogeneity, and well test based estimates (Eq. (6.23)) is preferred to estimates based on the theoretical formula (6.20).

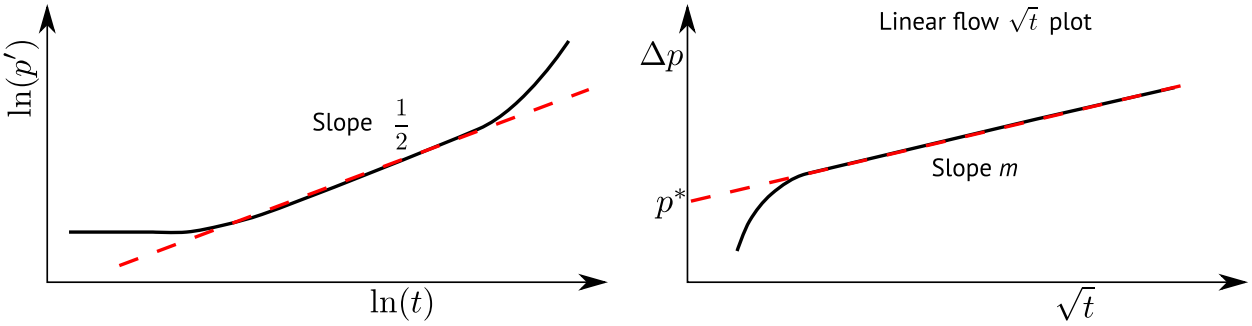


Figure 6.19: Plots for a channel system: The time period with slope 1/2 on the derivative plot corresponds to linear flow, and the channel width is estimated based on the slope of the straight line on the $\sqrt{t}$ plot.

For cases where the channels are narrow, the radial flow period will be suppressed, and it will be impossible to to use it to get good estimates for permeability and skin. If we have other data that can give estimates for the channel width, such as seismic data for fault blocks and outcrop data for channel belts, we can in these cases use Eq. (6.21) to get a permeability estimate:

$$k = \left(\frac{Q}{mhW}\right)^2 \frac{\mu}{\pi\phi c_t} \quad . \tag{6.24}$$

6.4 Leaking boundaries

In this section we will investigate the effect of boundaries that are not completely sealing. Two examples will be discussed in more detail: a partly sealing fault with good reservoir sand on both sides, and a boundary between good sand and a low permeable background.

Fig. 6.20 illustrates a typical situation where a fault runs through a reservoir. We may have good reservoir sand on both sides of the fault, and at the fault location there is a zone with reduced permeability. Both the faulting itself, and subsequent diagenetic processes contribute to the permeability reduction. The permeability in the fault zone is typically not zero, so communication is possible across the fault. In general the communication across the fault will be between different reservoir zones, with different permeability and thickness.

A general model that could be used for investigating the effect of a non sealing fault on a well test is shown in Fig. 6.21.

We will derive the well test response for a model that has been simplified even further: First, the fault zone is modelled as a plane with characteristic property $\beta_f = \frac{k_f}{L_f}$. This is the standard representation of faults in reservoir simulation. Second, we will assume that the

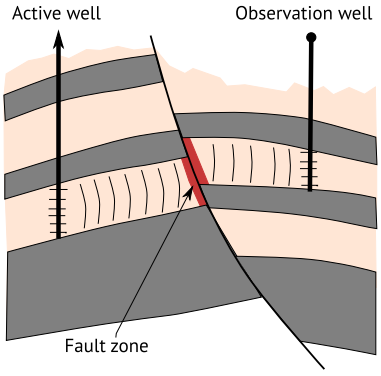


Figure 6.20: Communication across a fault

The fault zone is modelled as a plane.

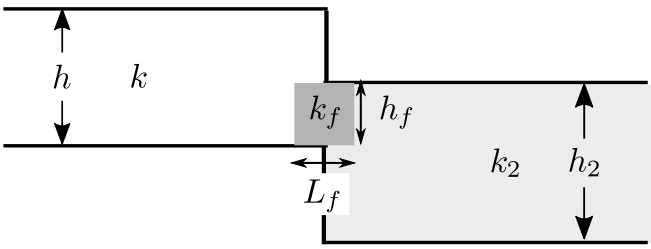


Figure 6.21: Simplified model for a non-sealing fault

reservoir on both sides have the same properties and height (essentially the same zone). Last, we will model the flow in two dimensions only, that is we will ignore the effect of the flow convergence towards the limited height contact zone.

Fig. 6.22 shows an aerial view of the model. An active well is placed at a distance L from the fault, and we will also investigate the response in an observation well on the far side of the fault.

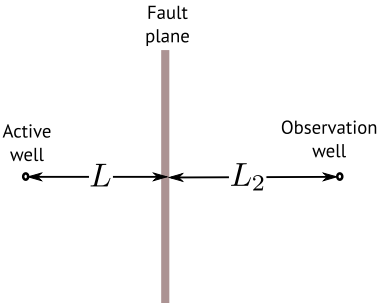


Figure 6.22: Areal view of a non-sealing fault with an observation well on the far side

In this analysis we will use L as characteristic length for dimensionless parameters:

$$x_{DL} = \frac{x}{L} \qquad t_{DL} = \frac{\eta t}{L^2} = \frac{kt}{\mu\phi c_t L^2} \quad , \tag{6.25}$$

and the fault is characterized by the dimensionless quantity α:

$$\alpha = \frac{L}{L_f}\frac{h_f}{h}\frac{k_f}{k} \quad . \tag{6.26}$$

If we ignore the short time effects due to the finite wellbore radius, the dimensionless pressure in the fault block with a well producing at at a constant rate is described by the following diffusivity equation:

$$\frac{\partial^2}{\partial x^2}p_1 + \frac{\partial^2}{\partial y^2}p_1 + 2\pi\,\delta(x+1)\delta(y) = \frac{\partial}{\partial t}p_1 \quad , \tag{6.27}$$

where δ is the Dirac delta function[4] which represent a point sink (the well at $x_{DL} = -1$ and $y_{DL} = 0$). The diffusivity equation that describe the pressure on the other side of the fault is

$$\frac{\partial^2}{\partial x^2}p_2 + \frac{\partial^2}{\partial y^2}p_2 = \frac{\partial}{\partial t}p_2 \quad . \tag{6.28}$$

The initial condition, and the boundary condition at infinity, is that pressure is initial pressure: $p_1 = p_2 = 0$. In addition we have two conditions at the fault that couple the two equations: Flow is continuous across the fault ($x = 0$)

$$\frac{\partial}{\partial x}p_1(0,y) = \frac{\partial}{\partial x}p_2(0,y) \quad , \tag{6.29}$$

and the flow through the fault is proportional to the pressure difference across the fault

$$\frac{\partial}{\partial x}p_1(0,y) = \alpha(p_1(0,y) - p_2(0,y)) \quad . \tag{6.30}$$

The equation system (6.27)–(6.30) may be solved using a Laplace transform in time and a Fourier transform in y.[5] The well pressure

[4] The delta function is zero everywhere, but $\int_{-\epsilon}^{\epsilon} f(x)\delta(x-x_0)\,dx = f(x_0)$

[5] L.M. Yaxley. "Effect of a Partially Communicating fault on Transient Pressure Behavior." In: *SPE Formation Evaluation* (Dec. 1987), pp. 590–598. DOI: 10.2118/14311-PA.

($x_D = -1$ and $y_D = 0$) is

$$p_D(t_{DL}, \alpha) = \frac{1}{2}\,\mathrm{E}_1\left(\frac{1}{4t_{DL}}\left(\frac{r_w}{L}\right)^2\right) + \frac{1}{2}\,\mathrm{E}_1\left(\frac{1}{t_{DL}}\right) - I(t_{DL}, \alpha) \quad , \tag{6.31}$$

where

$$I(t_{DL}, \alpha) = \sqrt{\pi}\alpha e^{4\alpha} \int_0^{t_{DL}} e^{4\alpha^2 u}\ \mathrm{erfc}\left(2\alpha\sqrt{u} + \frac{1}{\sqrt{u}}\right)\frac{du}{\sqrt{u}} \quad . \tag{6.32}$$

The complementary error function erfc() is also discussed on page 91.

We see that the well test response is the sealing fault response (6.4) minus a correction that is proportional to the transmissibility of the fault (α). The corresponding derivative diagnostic plot is shown in Fig. 6.23. For long enough times, the plot falls back to a plateau value

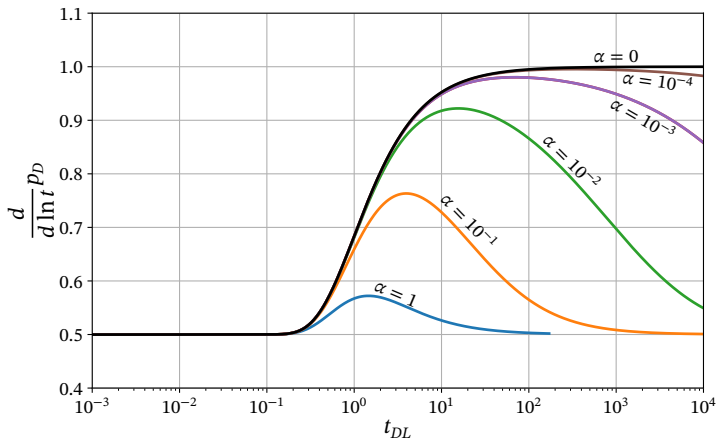


Figure 6.23: Log derivative diagnostic plot for a well near a non-sealing fault

of 1/2, so we have full-circle radial flow. The effect of the fault is seen in an intermediate period, and the fault transmissibility can be estimated based on type-curve matching (see page 130).

The fault properties can also be inferred from the response in an observation well on the far side of the fault. If the observation well is directly opposed to the active well as shown in Fig. 6.22, the observation-well pressure (pressure at $x_D = \frac{L_2}{L}$ and $y_D = 0$) is

$$\begin{aligned} p_D(t_{DL}, \alpha) &= I(t_2, \alpha_2) \\ \alpha_2 &= \frac{L + L_2}{L}\alpha \\ t_2 &= \left(\frac{L}{L + L_2}\right)^2 t_{DL} \end{aligned} \tag{6.33}$$

where $I(t, \alpha)$ is the correction function defined in Eq. (6.32). The corresponding derivative diagnostic plot is shown in Fig. 6.24. The time it takes for the pressure signal to reach the observation well depend on the fault transmissibility, and again the fault transmissibility can be estimated based on type-curve matching. For long enough times, the plot has a plateau value of 1/2, corresponding to full-circle radial flow.

The next example of a leaking boundary is a system where the well is placed in a sand body of limited extent. If the well is close to the edge of the sand-body, and the boundary is linear, this system is called linear-composite. The system is illustrated in Fig. 6.25.

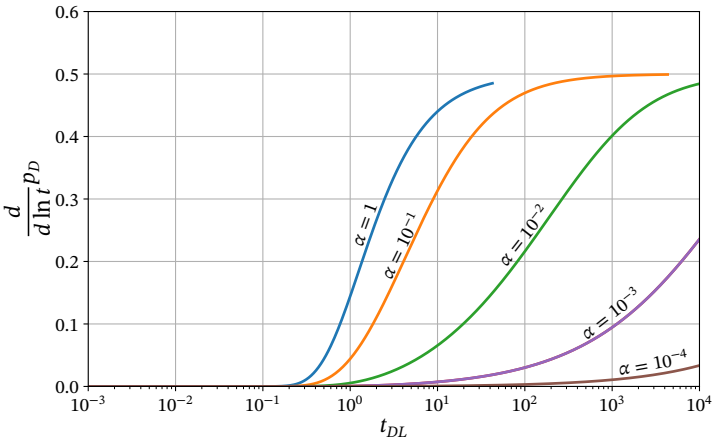


Figure 6.24: Log derivative diagnostic plot for the observation well on the far side of a non-sealing fault

The equations that govern the pressure response of this system is very similar to the equations for a leaky fault (Eqs. (6.27)–(6.29)), and they can be solved with the same methods. The fingerprint diagnostic plot corresponding to the linear composite are shown in Fig. 6.26.

The characteristics of the plot is an initial plateau, corresponding to radial flow, followed by a transition to a second higher plateau. The first plateau reflects the permeability in the sand body where the well is located, while the second reflects the *average permeability* in the sand and the low permeability background:

$$\begin{aligned} m &= \frac{Q}{4\pi kh} \\ \overline{m} &= \frac{Q}{4\pi \frac{k+k_2}{2} h} \end{aligned} \tag{6.34}$$

If the permeability of the background is much lower than the sand ($k_2/k \lessapprox 0.01$), then we will see a doubling just as for a completely closed barrier.

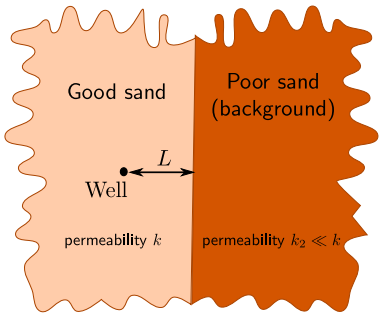


Figure 6.25: A well close to the edge of a sand-body

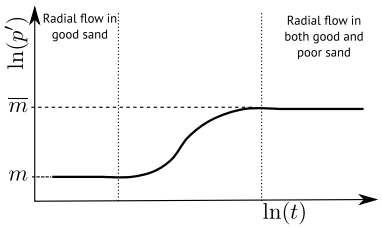


Figure 6.26: Fingerprint of a linear–composite system

7
Horizontal wells

Today most new production wells are horizontal or highly deviated. Compared to a vertical well, a horizontal well has an increased reservoir contact and an increased drainage area. As long as vertical communication is sufficient, a horizontal well will typically also have increased productivity. In reservoirs with an aquifer, gas cap or both, or with water or gas injection, horizontal wells can be judiciously placed to avoid gas and water coning and early break through of water or gas, which gives higher oil rates and increased reservoir sweep.

The objectives for testing of horizontal wells are basically the same as for vertical wells: Determine permeability (horizontal and vertical), skin (formation damage) and pseudoskin (completion effectiveness), and detecting reservoir and sand body boundaries.

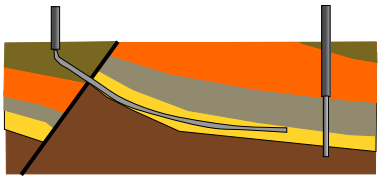


Figure 7.1: Horizontal vs. vertical well

7.1 Flow regimes

The main ideal flow regimes in a horizontal well are illustrated in Fig. 7.2. The flow regimes are vertical radial flow, where the top and bottom of the reservoir is not yet seen, intermediate linear flow, which is similar to flow in a channel, and, when the length of the well is negligible compared to the radius of investigation, horizontal radial flow. In addition there will be an initial period dominated by wellbore storage and skin, and a late time boundary dominated flow period.

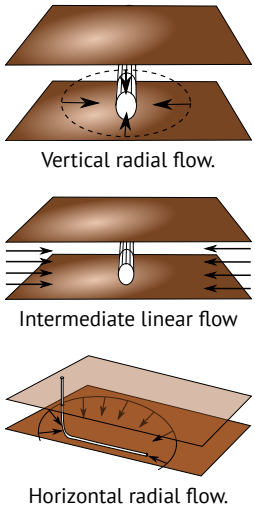


Figure 7.2: Ideal flow regimes in a horizontal well.

The ideal log–log diagnostic plot showing these flow regimes are shown in Fig. 7.3. It should be noted that it in practice can be difficult to identify all flow regimes.

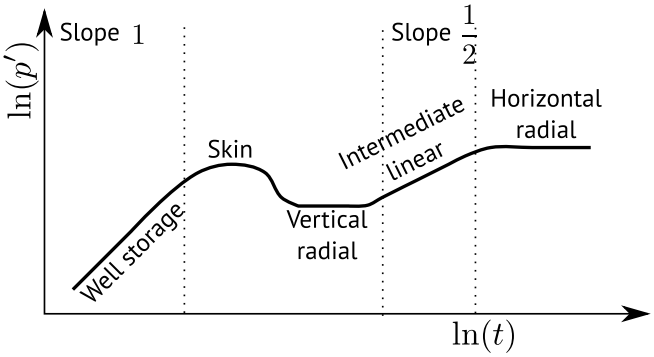


Figure 7.3: Ideal log–log diagnostic and flow regimes for a horizontal well

7.2 Anisotropy

We have previously assumed that permeability is isotropic and can be treated as a scalar. However, the permeability is usually different for vertical and horizontal flow, so for the description of flow around a horizontal well, where we have flow in both the horizontal and vertical direction, this assumption is normally not valid.

Permeability is actually a *tensor* [1], $\mathbf{K}$, and Darcys law should be expressed as

$$q = -\frac{1}{\mu}\mathbf{K}\cdot\nabla p \quad , \tag{7.1}$$

or, on component form

$$q_i = -\frac{1}{\mu}\sum_j K_{ij}\frac{\partial}{\partial x_j}p \quad , \tag{7.2}$$

where $\mathbf{K} = (K_{ij})$. Since permeability is a tensor, flow is in general not parallel to the pressure gradient. However, the permeability is associated with certain principal directions in space. If the pressure gradient is along any of these principal directions the flow will be in that direction, and the matrix that represent the permeability tensor is diagonal in a coordinate system that follows the principal directions. There are three orthogonal principal directions, and the directions are determined by the geology. In general both the permeability along the principal directions and the directions themselves are space dependent, however, the main anisotropy is usually vertical vs. horizontal, in which case the principal directions are

[1] Permeability is a linear operator that operates on a gradient to produce a vector. Such operators are called (2,0) tensors, or more simply tensors of order 2. A tensor of order 2 can be represented by a matrix in a given coordinate system, and the operation as a matrix–vector multiplication.

Principal directions

- Orthogonal to bedding ("vertical" k_v or k_z)
- Parallel to bedding ("horizontal" k_h or k_x and k_y)

Vertical permeability can be several orders of magnitude smaller than horizontal permeability. The ratio is called KVKH-ratio and is an important property for correct reservoir modelling.

KVKH-ratio

The main source of $k_v < k_h$ anisotropy is small scale heterogeneities. Since the nature of deposited material is not constant over time, there will always, in a sandstone reservoir, be a layered or semi-layered structure. The spatial frequency of these structures vary, and can be as high as on the mm scale in the case of tidally influenced deposits as illustrated in Fig. 7.4. On larger scales (dm–m), both depositional and diagenetic processes produce horizontal sheets of shales and cemented barriers that restrict vertical flow as illustrated in Fig. 7.5. In contrast, in fractured reservoirs (see page 93) the main fracture direction is often vertical so that the permeability is largest in the vertical direction.

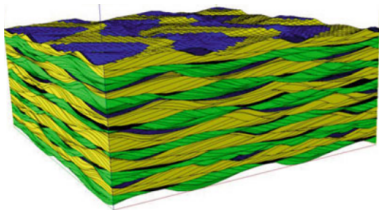


Figure 7.4: Small scale heterogeneities

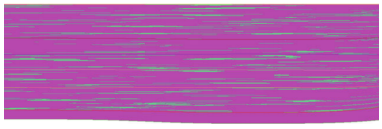


Figure 7.5: Barriers and baffles restricting vertical flow

7.3 Quantitative analysis

In this section we will discuss how the vertical–radial and linear flow regimes may be analyzed.

7.3.1 Vertical–radial flow

The vertical radial flow regime (Fig. 7.6) can be analyzed using a straight line fit on a semilog plot. That is, permeability and skin can be found in the same way as for a vertical well. But since the permeability is anisotropic it is unclear which permeability is actually estimated by this procedure, and what the measured skin factor represents.

The flow around a vertical well is described by the anisotropic diffusivity equation

$$\left[k_y \frac{\partial^2}{\partial y^2} + k_z \frac{\partial^2}{\partial z^2}\right] p = \mu \phi c_t \frac{\partial}{\partial t} p \quad , \tag{7.3}$$

where the well runs along the x-direction. Due to the permeability anisotropy, the pressure front travels faster in the horizontal direction than in the vertical, and the lines of equal pressure are ellipses.

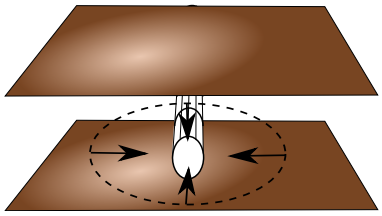


Figure 7.6: Vertical radial flow

We can transform the anisotropic equation (7.3) into an equivalent isotropic equation by scaling lengths x_i with $\sqrt{k'/k_i}$, so that $x_i' = \sqrt{k'/k_i} x_i$. Then we have

$$\frac{\partial^2}{\partial {x_i}^2} = \frac{\partial^2 x_i'}{\partial {x_i}^2} \frac{\partial^2}{\partial {x_i'}^2} = \frac{k'}{k_i} \frac{\partial^2}{\partial {x_i'}^2} \quad . \tag{7.4}$$

Applying the above transformation to Eq. (7.3), then the resulting equation is

$$k' \left[\frac{\partial^2}{\partial {y'}^2} + \frac{\partial^2}{\partial {z'}^2}\right] p = \mu \phi' c_t' \frac{\partial}{\partial t} p \quad , \tag{7.5}$$

where we have replaced ϕ, and c_t with ϕ', and c_t' to indicate that these parameters may not be invariant under the coordinate transform. Since the parameters are volumetric they will be invariant if the coordinate transform preserve volume, i.e. $L_y L_z = L_y' L_z'$.We have

$$L_y' L_z' = \sqrt{\frac{k'}{k_y}} L_y \sqrt{\frac{k'}{k_z}} L_z = \frac{k'}{\sqrt{k_y k_z}} L_y L_z \quad . \tag{7.6}$$

Thus, under the condition

$$\frac{k'}{\sqrt{k_y k_z}} = 1 \implies k' = \sqrt{k_y k_z} \quad , \tag{7.7}$$

the parameters ϕ and t will be invariant under the coordinate transform. Flow governed by the anisotropic diffusivity equation can then be described by an equivalent isotropic equation:

$$k' \left[\frac{\partial^2}{\partial {y'}^2} + \frac{\partial^2}{\partial {z'}^2}\right] p = \mu \phi c_t \frac{\partial}{\partial t} p \quad . \tag{7.8}$$

This implies that the permeability estimate found by fitting to a straight line,

$$k' = \frac{Q\mu}{4\pi L} \frac{1}{m} \quad , \tag{7.9}$$

where L is the well length, corresponds to the equivalent isotropic permeability

$$\boxed{k' = \sqrt{k_z k_y}} \quad . \tag{7.10}$$

An anisotropic reservoir behaves like an isotropic reservoir with effective permeability $k = \sqrt{k_z k_y}$.

In order to understand how the estimated skin is to be interpreted we will have a closer look at how the shape of the bore-hole and its surroundings are transformed. The anisotropy is characterized by the KVKH–ratio, M:

$$M = \frac{k_z}{k_y} \quad . \tag{7.11}$$

In the equivalent isotropic system lengths in the x_i direction are scaled with

$$\sqrt{\frac{k'}{k_i}} = \sqrt{\frac{\sqrt{k_z k_y}}{k_i}} \quad , \tag{7.12}$$

thus

$$L'_y = \sqrt[4]{M}\, L_y \qquad L'_z = \sqrt[4]{\frac{1}{M}}\, L_z \quad . \tag{7.13}$$

Typically, $k_z < k_y$, so that $M < 1$. This yields $L'_y < L_y$ and $L'_z > L_z$, thus due to the scaling of lengths (Eq. (7.13)), the effective thickness of the reservoir is increased. As a result, the duration of the vertical radial flow period is increased in an anisotropic reservoir. In spite of this, the flow regime may often not be observed with realistic well paths. Vertical positioning of horizontal wells can be poor even when geo-steering tools are used, and wells are also intentionally drilled through layering to create improved reservoir contact. Examples of

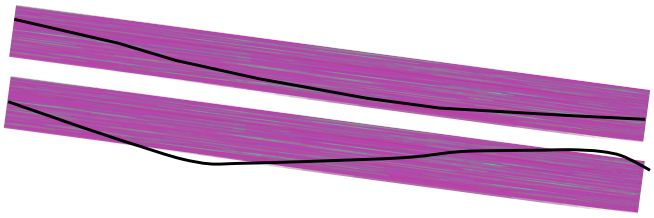


Figure 7.7: Typical well paths of a real horizontal well

well paths are shown in Fig. 7.7, and it is unlikely that vertical radial flow is reached in these wells.

We see from Eq. (7.13) that the circular wellbore is transformed to an ellipse as shown in Fig. 7.8, and the damaged volume around the wellbore is also transformed in a similar manner. The permeability of the damaged zone does typically not have the same anisotropy as the reservoir, so we will have an anisotropic permeability in the skin region of the equivalent model. Any near wellbore heterogeneities will also be transformed, and will influence pressure profile differently than the bulk k_v–k_h model. As a consequence, the measured skin has no direct physical interpretation in terms of permeability and thickness of a damaged zone. Predicting the skin based on a model of the damaged zone is non-trivial. The skin is therefore estimated by the difference between the pressure in a isotropic model with effective

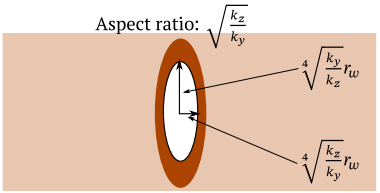


Figure 7.8: The circular wellbore is transformed to an ellipse.

permeability k and a circular wellbore with radius r_w, and the actual extra pressure drop due to a damaged zone in an anisotropic reservoir.

The coordinate transform is volume preserving, so it does not influence the wellbore storage effect.

7.3.2 Intermediate–linear flow

As shown in Fig. 7.9, the intermediate flow situation is analogous to linear flow in a channel (see page 73), and the well pressure is given by

$$\Delta p = \sqrt{\frac{\mu}{\pi\phi c_t k_h}}\frac{Q}{l_w h}\sqrt{t} + \frac{Q\mu}{2\pi\sqrt{k_v k_h}\,l_w}(S + \sigma(M, h, z_w)) \quad . \tag{7.14}$$

Here l_w is the length of the well. The first term is the solution to the 1-D diffusivity equation with a point source, and since the flow is horizontal it only depend on the horizontal permeability $k_h = k_y = k_x$. The second term is the pressure drop due to skin, which depend on the effective isotropic permeability $\sqrt{k_v k_h}$. The third term is pressure drop due to convergence of flow into the well in two dimensions (pseudoskin). Here z_w is the height from the formation bottom, as illustrated in Fig. 7.9.

The linear flow regime can be analyzed to get estimates for horizontal permeability, k_h, and pseudoskin, σ. We see from Eq. (7.14) that if we plot pressure as a function of $\sqrt{t}$ and fit the linear flow period to a straight line. Then the horizontal permeability is found from the slope, m, as

$$\boxed{k_h = \frac{Q^2\mu}{l_w^2 h^2 \pi\phi c_t}\frac{1}{m^2}} \quad . \tag{7.15}$$

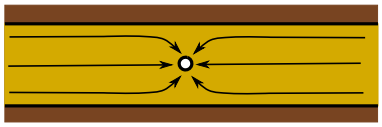


Figure 7.9: Intermediate linear flow. The additional pressure drop due to flow convergence towards the well is called pseudoskin.

If the effective permeability, $\sqrt{k_v k_h}$, and skin S is known, the pseudoskin can be found using the extrapolated pressure Δp^* at $t = 0$

$$\boxed{\sigma = \frac{2\pi\sqrt{k_v k_h}\,l_w}{Q\mu}\Delta p^* - S} \quad . \tag{7.16}$$

The ideal pseudoskin in a homogeneous system depend on the three ratios $M = k_v/k_h$, h/r_w, and z_w/h as

$$\sigma(M, h, z_w) = \ln\left(\frac{h}{\pi r_w\left(1 + \sqrt{M}\right)\sin(\pi\frac{z_w}{h})}\right) \quad , \tag{7.17}$$

where z_w/h is the relative position (depth) of the well in the zone. In theory, one can use a measured pseudoskin to evaluate the well positioning. In practice this may be impossible due to near wellbore heterogeneities or variation in the relative vertical position along wellbore

7.4 Near well heterogeneities

All well testing is sensitive to near well heterogeneities, and a horizontal well is even more sensitive to near well heterogeneities than a

vertical well. An illustration of a horizontal well in a heterogeneous environment is shown in Fig. 7.10. The heterogeneities will influence



Figure 7.10: A horizontal well in a heterogeneous environment

skin and pseudoskin, so the measured skin and pseudoskin will contain information relating to the heterogeneity pattern. On the other hand, the presence of these heterogeneities will influence the pressure response in a way that may mask the vertical radial flow regime.

The idealized analysis assume that the inflow is constant along the well. This may not hold due to a heterogeneous formation, uneven formation damage, or well friction, as illustrated in Fig. 7.11.

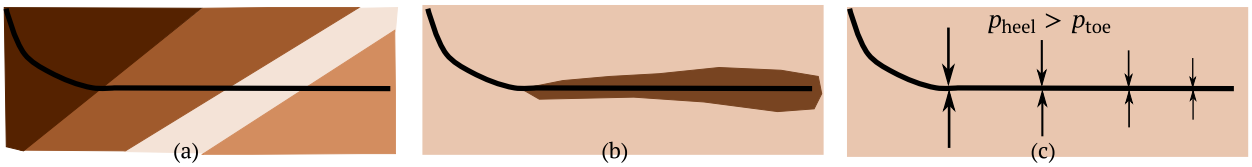


Figure 7.11: Uneven inflow along the well due to heterogeneous formation (a), uneven well damage (b) and well friction (c).

7.5 Well tip effects

If the well does not penetrate the whole reservoir there will be a heel and toe effect that may mask the vertical radial flow or linear flow.

The drainage pattern around the central part of the well will be radial, while the drainage at the tip will have a (hemi)-spherical shape. This is illustrated in Fig. 7.12.

To get a rough estimate for when the spherical flow pattern start influencing the pressure response in the well we may assume that the contribution from each flow regime (radial vs. spherical) is proportional to the area of the corresponding pressure front. The area of the spherical front is

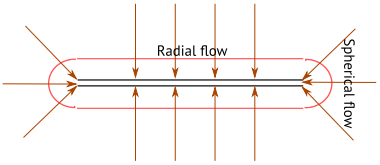


Figure 7.12: Effect of finite well length

$$A_{\text{spherical}} \approx 4\pi r_{\text{inv}}^2 \propto t \quad , \tag{7.18}$$

where $r_{\text{inv}} = \sqrt{4\eta t}$ is the radius of investigation (Eq. (3.26)). The area of the radial front is

$$A_{\text{radial}} \approx 2\pi l_w r_{\text{inv}} \propto \sqrt{t} \quad . \tag{7.19}$$

The spherical contribution is negligible for short times, but due to the different time dependency of the two terms, spherical flow will ultimately be dominant. The tip effect is negligible when $A_{\text{spherical}} \ll A_{\text{radial}}$:

$$r_{\text{inv}} \ll \frac{1}{2} l_w \quad , \tag{7.20}$$

which gives

$$t \ll \frac{l_w^2}{16\eta} = \frac{\mu\phi c_t}{16k'} l_w'^2 \quad , \tag{7.21}$$

where Eq. (7.21) is expressed in terms of lengths in an isotropic reservoir. We will need to take into account anisotropy. By repeating the procedure outlined on page 81 (scaling lengths with $\sqrt{k'/k_i}$), but now in three dimensions, we see that we need to make the following substitutions[2]:

$$k' \to \sqrt[3]{k_h^2 k_v}\,, \quad l_w' \to \sqrt[6]{\frac{k_v}{k_h}}\, l_w \quad \text{and} \quad h' \to \sqrt[3]{\frac{k_h}{k_v}}\, h \quad , \tag{7.22}$$

where h is the reservoir thickness. We may conclude that the tip effect can be neglected as long as

$$\boxed{t \ll \frac{\mu\phi c_t}{16\sqrt[3]{k_h^2 k_v}} \sqrt[3]{\frac{k_v}{k_h}} l_w^2 = \frac{\mu\phi c_t}{16k_h} l_w^2} \quad . \tag{7.23}$$

The time where the tip effect can be ignored depend only on the horizontal permeability, and Eq. (7.23) can also be obtained by just considering Eq. (7.20) as an inequality in one dimension along the wellbore.

In short horizontal wells the tip effect may come into play before the pressure front reaches the top and bottom of the reservoir. In these cases we will not see the intermediate linear flow regime. If the well is in the middle of the reservoir, the time to reach top and bottom is determined by

$$r_{\text{inv}} = \frac{1}{2} h' \quad , \tag{7.24}$$

where lengths are measured in the equivalent isotropic reservoir. Using the definition of radius of investigation, solving for time, and making the substitutions (Eq. (7.22)) we get

$$t_r = \frac{\mu\phi c_t}{16k'} h'^2 = \frac{\mu\phi c_t}{16\sqrt[3]{k_h^2 k_v}} \left(\sqrt[3]{\frac{k_h}{k_v}} h \right)^2 = \frac{\mu\phi c_t}{16k_v} h^2 \quad , \tag{7.25}$$

where t_r is the time to reach the top of the reservoir. This time depend only on the vertical permeability, and Eq. (7.25) can also be derived by just considering Eq. (7.24) as an equality in the vertical direction.

If we say that Eq. (7.23) is equivalent to

$$t < 0.01 \frac{\mu\phi c_t}{16k_h} l_w^2 \quad , \tag{7.26}$$

then by comparing Eq. (7.26) and Eq. (7.25) we see that intermediate linear flow can be observed when

$$\begin{aligned} t_r &< 0.01 \frac{\mu\phi c_t}{16k_h} l_w^2 \\ \frac{\mu\phi c_t}{16k_v} h^2 &< 0.01 \frac{\mu\phi c_t}{16k_h} l_w^2 \\ 100 \frac{k_h}{k_v} h^2 &< l_w^2 \end{aligned} \tag{7.27}$$

[2] The reader might find it confusing that the effective permeability is different in two and three dimensions (Eqs. (7.10) and (7.22)). Note that the equation for the permeability estimate (7.9) contain the well length, l_w, which has to be scaled for three dimensional flow. When taking this into account, the permeability estimated in the well test is $k = \sqrt{k_h k_v}$ just as in the two dimensional case. Note also that the relative scaling of horizontal and vertical lengths is the same.

This yields the following criterion for observing intermediate linear flow:

$$\boxed{l_w > 10\sqrt{\frac{k_h}{k_v}}\,h} \quad . \tag{7.28}$$

Criterion for observing intermediate linear flow

8
Fractured wells

Hydraulic fracturing is a popular and effective stimulation method. A fracture is defined as a single crack initiated from the wellbore by hydraulic fracturing, that is by injecting a fluid (typically water with additives) at high pressure. The fracture is kept open by injecting a proppant (sand or similar particulate material) with the fracturing fluid. A fractured well has an increased productivity since the fracture provides an increased surface for the reservoir fluid to enter the wellbore. The orientation of the fracture plane is determined by the minimum stress direction, and since the maximum stress is always the overburden in deep reservoirs, fractures are vertical in deep reservoirs. Note that hydraulically induced fractures are different from naturally occurring fractures, which will be discussed in a separate chapter (page 93). Natural fractures are often called "fissures" to avoid confusion.

In addition to the usual reservoir characterization goals, well tests are performed in order to investigate the efficiency of hydraulic fracturing jobs, and to monitor any possible degradation of fracture properties due to production. In order to reach these goals, a separate well test should preferentially be performed prior to fracturing of the reservoir to determine permeability and skin.

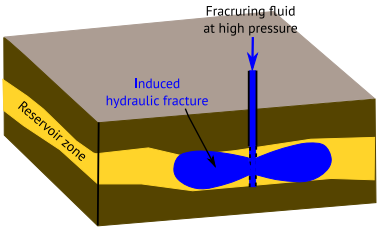


Figure 8.1: The concept of hydraulic fracturing

8.1 Laplace transform in well testing

In this and in subsequent chapters we will apply the Laplace transform. The Laplace transform is useful for solving differential equations, as it can transform partial differential equations into ordinary differential equations we are able to solve. The transform was in fact developed to solve the diffusion equation, i.e. an equation on the form of Eq. (2.14). Joseph Fourier had introduced a method to solve the diffusion equation using the Fourier transform. Laplace recognized that the Fourier transform was only applicable for a limited space, and introduced the Laplace transform to find solutions in indefinite space.

The Laplace transform $\mathscr{L} : f \rightarrow \tilde{f}$ is an integral transform, and it is usually applied as a transform in time:

$$\tilde{f}(s) = \int_0^\infty f(t)e^{-st}\,dt \quad . \tag{8.1}$$

The partial differential operator we used in the superposition principle (see page 39) was linear. Also the Laplace transform is a linear operator:

$$\begin{aligned} \mathscr{L}(f+g) &= \mathscr{L}f + \mathscr{L}g = \tilde{f} + \tilde{g} \\ \mathscr{L}(cf) &= c\mathscr{L}f = c\tilde{f} \quad . \end{aligned} \tag{8.2}$$

A further property of the Laplace transform is the following:

$$\mathscr{L}(f * g) = \mathscr{L}(f)\mathscr{L}(g) \quad , \tag{8.3}$$

where the first expression is a *finite convolution* defined as:

$$(f * g)(t) = \int_0^t f(\tau)g(t-\tau)d\tau \quad . \tag{8.4}$$

The power of the convolution is that is can be used to find the inverse Laplace transform as follows:

$$\mathscr{L}^{-1}(\mathscr{L}(f)\mathscr{L}(g)) = f * g \tag{8.5}$$

Calculating the integral, we observe that the Laplace transform of unity and of t are

$$\begin{aligned} \mathscr{L}(1) &= \int_0^\infty e^{-st}\,dt = \left[-\frac{1}{s}e^{-st}\right]_0^\infty = \frac{1}{s} \\ \mathscr{L}(t) &= \int_0^\infty te^{-st}\,dt = \left[-\frac{t}{s}e^{-st}\right]_0^\infty - \int_0^\infty -\frac{1}{s}e^{-st}\,dt = \frac{1}{s}\mathscr{L}(1) = \frac{1}{s^2} \quad , \end{aligned} \tag{8.6}$$

where we are applying integration by parts when solving the transform in time t. We observe that time t and the variable s has an inverse correspondence, hence late times t corresponds to small s. This correspondence will be utilized in the next chapter.

The transformation of the partial derivatives are

$$\begin{aligned} \mathscr{L}\left(\frac{\partial f}{\partial x}\right) &= \int_0^\infty \frac{\partial f}{\partial x}e^{-st}\,dt = \frac{d\tilde{f}}{dx} \\ \mathscr{L}\left(\frac{\partial f}{\partial t}\right) &= \int_0^\infty \frac{\partial f}{\partial t}e^{-st}\,dt = s\tilde{f}(x,s) - f(x,0) \quad , \end{aligned} \tag{8.7}$$

where we use the basic rule $\int \frac{\partial}{\partial x}f(x,y)dy = \frac{\partial}{\partial x}\int f(x,y)dy$ for the first equality, and integration by parts for the second equality.

Using the above rules, we see that the diffusivity equation (2.16),

$$\eta\nabla^2 p = \frac{\partial p}{\partial t} \quad , \tag{8.8}$$

is transformed into the form

$$\eta\nabla^2\tilde{p} = s\tilde{p} - p_i \quad . \tag{8.9}$$

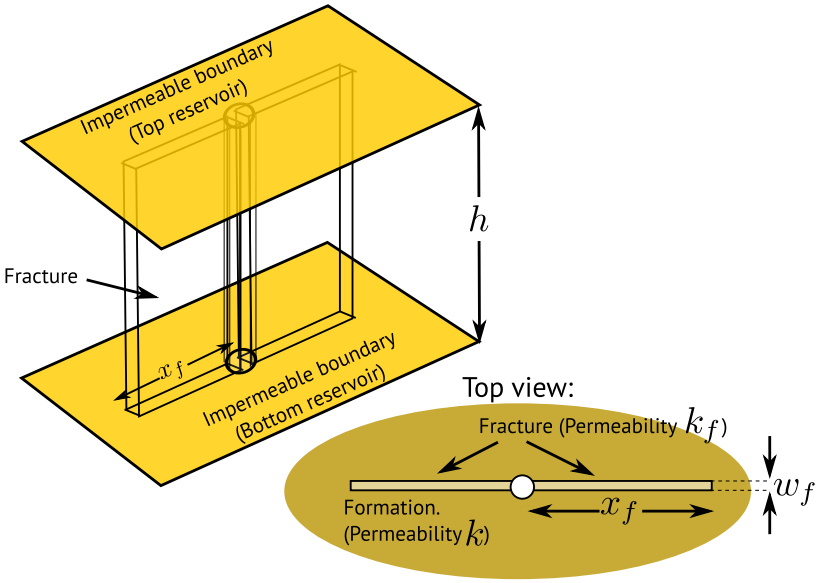


Figure 8.2: Characteristic parameters for a vertically fractured well

8.2 Vertical fractures

As discussed in the introduction, fractures in deep reservoirs are typically in the vertical direction. In this chapter we will therefore consider the analysis of a well test in a vertical well with a vertical fracture that covers the whole reservoir thickness.

A simplified model for this situation is illustrated in Fig. 8.2, and the fracture is characterized by fracture half length, x_f, fracture width, w_f, and fracture permeability, k_f.

8.3 Flow periods and flow regimes

The possible flow regimes in a vertically fractured well are shown in Fig. 8.3: Initially there is flow only in the fractures (a), this is called

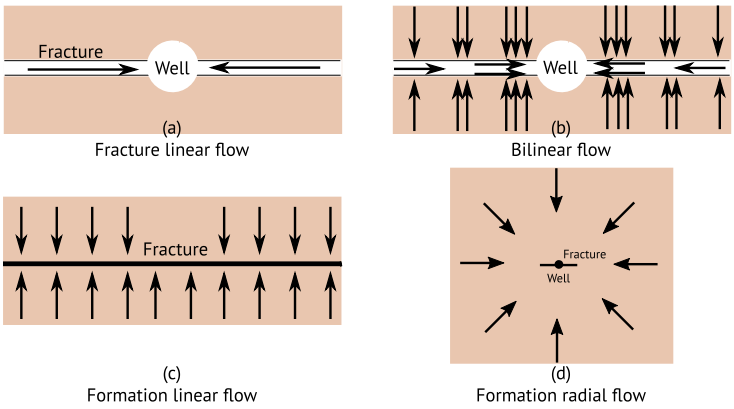


Figure 8.3: Possible flow regimes in a vertically fractured well

Fracture linear flow

fracture linear flow. This regime is, however, never observed in practice, and the effect of the fracture is instead seen as an increased volume for wellbore storage. In the second regime, (b), the pressure front

extends both linearly along the fracture and linearly into the reservoir close to the fracture. This is called bilinear flow. This regime is only observed when the fracture has a low conductivity. In the third regime, (c), the pressure front moves linearly out from the fracture into the reservoir. This is formation linear flow. When the distance from the well to the pressure front is large compared to the fracture length, we are in the fourth regime, (d), where the flow is infinite-acting radial flow, called formation radial flow.

Bilinear flow

Formation linear flow

Formation radial flow

8.4 Formation radial flow

The radial flow can be analyzed is using the standard methods for non-fractured wells. In particular this means that permeability and skin is found by fitting to a straight line on semi-log plot. As illustrated in Fig. 8.4, there will be a reduced convergence of flow lines into a fractured well compared to a non-fractured well. A successfully fractured well will thus have a negative skin, reflecting the desired improved productivity.

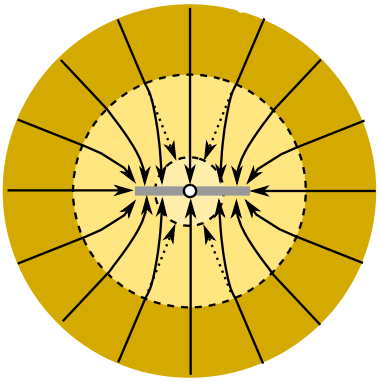


Figure 8.4: Due to the reduced flow convergence, the effect of the fracture will be a negative skin or increased defective wellbore radius.

8.5 Formation linear flow

In this section we will derive the equation for linear (1-dimensional) flow, and show how the analysis of the formation linear flow period can provide an estimate for how far the fracture has propagated into the reservoir, that is the fracture half-length.

As long as the propagating pressure front is close enough to the fracture such that we can ignore tip effects, the problem is one dimensional. The diffusivity equation is then

$$\frac{\partial^2 P}{\partial x^2} = \frac{1}{\eta}\frac{\partial P}{\partial t} \quad , \tag{8.10}$$

where

$$P = p_i - p \quad \text{and} \quad \eta = \frac{k}{\mu\phi c_t} \quad . \tag{8.11}$$

Pressure is at initial pressure at infinity, giving the boundary conditions

$$P(x,0) = 0 \quad \text{and} \quad P(\infty,t) = 0 \quad . \tag{8.12}$$

Darcy's law gives the boundary condition for the pressure gradient at the fracture:

$$\left.\frac{\partial P}{\partial x}\right|_{x=0} = -\frac{\mu}{4x_f hk}Q(t) \quad , \tag{8.13}$$

where we have used that half of the flow rate goes into each flow direction (see Fig. 8.2).

Solving by Laplace transform.

Equations (8.10)–(8.13) can be solved by Laplace transform in time: Similar to the transform into Eq. (8.9), the partial differential equation (8.10) is then transformed into an ordinary differential equation in x:

$$\frac{d^2\tilde{P}}{dx^2} = \frac{s}{\eta}\tilde{P} \quad . \tag{8.14}$$

where we have applied the initial condition (8.12). The general solution to Eq. (8.14) is

$$\tilde{P}(x,s) = A\exp\left(\sqrt{\frac{s}{\eta}}x\right) + B\exp\left(-\sqrt{\frac{s}{\eta}}x\right) \quad . \tag{8.15}$$

Due to the boundary condition at infinity (Eq. (8.12)) we have $A = 0$, and B is determined by applying the boundary condition on the derivative (Eq. (8.13)):

$$\left.\frac{\partial\tilde{P}}{\partial x}\right|_{x=0} = \int_0^\infty -\frac{\mu}{4x_f hk}Q(t)e^{-st}\,dt = -\frac{\mu}{4x_f hk}\tilde{Q}(s) \quad . \tag{8.16}$$

Assuming a constant well rate $Q(t) = Q$ starting at $t = 0$ then gives

$$\tilde{Q}(s) = Q\cdot\tilde{1} = \frac{Q}{s} \quad , \tag{8.17}$$

where we use that the Laplace transform of unity is $1/s$ from Eq. (8.6). Thus

$$\begin{aligned} -\sqrt{\frac{s}{\eta}}B = \left.\frac{\partial\tilde{P}}{\partial x}\right|_{x=0} &= -\frac{\mu}{4x_f hk}\frac{Q}{s} \\ B &= \frac{\mu\sqrt{\eta}}{4x_f hk}Qs^{-\frac{3}{2}} \end{aligned} \tag{8.18}$$

This give the following solution in Laplace space:

$$\tilde{P}(x,s) = \frac{\mu\sqrt{\eta}}{4x_f hk}Qs^{-\frac{3}{2}}\exp\left(-\sqrt{\frac{s}{\eta}}x\right) \quad . \tag{8.19}$$

By an iterative procedure one can show that

$$\mathcal{L}(t^n) = \frac{\Gamma(n+1)}{s^{n+1}} \quad , \tag{8.20}$$

where the gamma-function Γ is an extension of the factorial function such that $\Gamma(n+1) = n!$. Applying the inverse Laplace function $\mathcal{L}^{-1}$ to Eq. (8.20) then yields:

$$\mathcal{L}^{-1}(s^n) = \frac{t^{-n-1}}{\Gamma(-n)} \quad . \tag{8.21}$$

Further we have the following inverse Laplace transforms[1]:

$$\mathcal{L}^{-1}\left(\frac{1}{s}\exp\left(-a\sqrt{s}\right)\right) = \operatorname{erfc}\left(\frac{a}{2\sqrt{t}}\right) \quad . \tag{8.22}$$

The *complementary error function* $\operatorname{erfc}() = 1 - \operatorname{erf}()$, where erf() is the *error function*:

$$\operatorname{erf}(x) = \frac{2}{\sqrt{\pi}}\int_0^x e^{-u^2}du \quad . \tag{8.23}$$

We observe from the plot in Fig. 8.5 that the complementary error function is rapidly converging towards zero.

With the method of finite convolutions given by Eq. (8.5), we can apply the inverse transforms Eq. (8.21) and Eq. (8.22) on Eq. (8.19) to find the pressure as a function of time and distance from the fracture:

$$P(x,t) = \frac{Q\mu\sqrt{\eta}}{4x_f kh}\left[2\sqrt{\frac{t}{\pi}}e^{-\frac{x^2}{\eta t}} - \frac{x}{\sqrt{\eta}}\operatorname{erfc}\left(\frac{x}{2\sqrt{\eta t}}\right)\right] \quad . \tag{8.24}$$

[1] The inverse transform can be found in good tables of Laplace transforms, or by using a computer algebra program such as Maple or Mathematica.

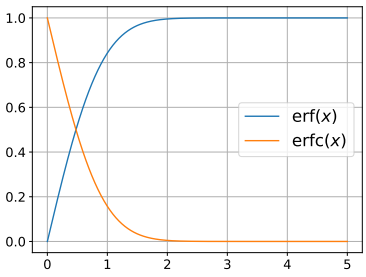


Figure 8.5: A plot of the error function and the complementary error function for positive values.

Due to the shape of the complementary error function, we see that the pressure P converge to zero away from the well, thus the pressure converge to the initial pressure away from the well.

For well testing purposes we are only interested in the well pressure, and inserting $x = 0$ into Eq. (8.24) gives

$$\boxed{p_w(t) = p_i - \frac{Q\mu\sqrt{\eta}}{2x_f kh\sqrt{\pi}}\sqrt{t}} \quad . \tag{8.25}$$

We see from Eq. (8.25) that the well pressure response in the formation linear flow regime is proportional to the square root of time. The flow regime is identified on the log-derivative diagnostic plot as a period with slope $\frac{1}{2}$, and on a plot of pressure as a function of $\sqrt{t}$ the period with formation linear flow will show a straight line with slope m:

$$m = \frac{Q\mu\sqrt{\eta}}{2x_f kh\sqrt{\pi}} = \frac{Q}{2x_f h}\sqrt{\frac{\mu}{k\pi\phi c_t}} \quad . \tag{8.26}$$

If permeability is known, for instance from analysis of the formation radial flow period or from a test performed prior to fracturing, the slope can be used to estimate the fracture half length:

Fracture half-length is estimated based on the slope of a straight line on a p vs. $\sqrt{t}$ plot.

$$\boxed{x_f h = \frac{Q}{2m}\sqrt{\frac{\mu}{k\pi\phi c_t}}} \quad . \tag{8.27}$$

Note that the property actually measured is the fracture area, $A_f = 2x_f h$.

8.6 Bilinear flow

If the fracture has a finite conductivity, an early flow period with bilinear flow, as illustrated in Fig. 8.6, may be observed. This flow period can be analyzed to obtain an estimate for fracture conductivity.

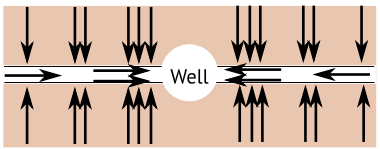


Figure 8.6: Bilinear flow

The early time behavior with a finite permeability fracture can be shown to be[2]

$$p = p_i - m\sqrt[4]{t} \quad , \tag{8.28}$$

where [3]

$$m = \frac{\Gamma\left(\frac{3}{4}\right)Q\mu}{\pi h\sqrt{k_f w_f}\sqrt[4]{\phi\mu c_t k}} \quad . \tag{8.29}$$

[2] H. Cinco-Ley and Samaniego-V. F. "Transient Pressure Analysis for Fractured Wells." In: *Journal of Petroleum Technology* (Sept. 1981), pp. 1749–1766. DOI: 10.2118/7490-PA.

[3] $\Gamma(\cdot)$ is the gamma function.

We see from Eq. (8.28) that the pressure response for bilinear flow is proportional to the 4th root of time. Thus, the flow regime is identified on the log-derivative diagnostic plot as a period with slope $\frac{1}{4}$, and on a plot of pressure as a function of $\sqrt[4]{t}$, the period with formation linear flow will show a straight line with slope m. If permeability is known, the slope can be used to estimate the fracture conductivity $k_f w_f$:

A special $\sqrt[4]{t}$ plot is used to estimate fracture conductivity.

$$\boxed{k_f w_f = \left(\frac{\Gamma\left(\frac{3}{4}\right)Q\mu}{\pi hm}\right)^2 \frac{1}{\sqrt{\phi\mu c_t k}} \approx \frac{0.152}{\sqrt{\phi\mu c_t k}}\left(\frac{Q\mu}{hm}\right)^2} \quad . \tag{8.30}$$

9
Naturally fractured reservoirs

Naturally fractured reservoirs constitute a huge portion of petroleum reservoirs throughout the world, especially in Middle East. A natural fracture are created when stresses exceed the rupture strength of the rock, and the fracturing process is more prevalent in brittle rocks such as limestone, as opposed to sandstone.

The presence of fractures is crucial for the productivity of low permeable rocks, as the highly conductive fractures increase the effective permeability of the formation.

A naturally fractured formation is generally represented by a tight matrix rock broken up by highly permeable fractures (see Fig. 9.1).

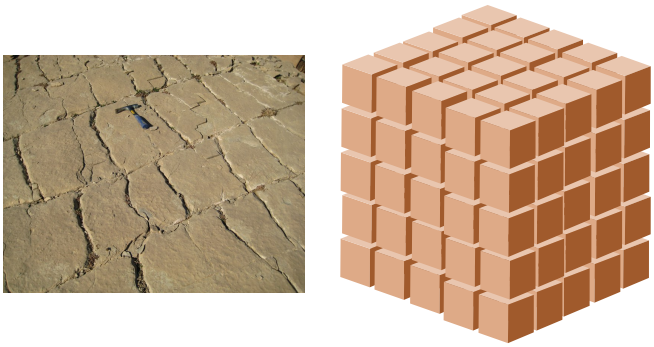


Figure 9.1: Representations of a dual porosity reservoir. Outcrop of fractured carbonate rock (left), and a simplified 3D "stacked sugar cubes" representation (right).

The fractures tend to form a continuous fracture network throughout the formation, and they represent the dominant flow paths. If only the fractures are connected, and there is virtually no long distance transport in the matrix system, the formation may be denoted as *dual porosity*. If there is some flow through the matrix system, the formation is denoted as *dual porosity – dual permeability*. Note that macroscopic behavior of these systems in many cases are single porosity, where the presence of fractures only effect effective permeability and porosity. In these notes we will only discuss dual porosity systems.

9.1 Dual porosity model

In a dual porosity system, the macroscopic fluid flow is only in the fractures. A characteristic feature of dual porosity systems is that the effective permeability of the formation, as found by well testing and

production, is much larger that the permeability measured on core material:

$$k_{\text{formation}} \gg k_{\text{matrix}} = k_{\text{core}} \quad . \tag{9.1}$$

This is illustrated in Fig. 9.2.

In many cases the number of fractures penetrated by a well is limited, and extra fractures must be created in the near well volume by hydraulic fracturing to sufficient productivity. The wells produce from the fracture system only, but the bulk of the oil is stored in the matrix:

$$V_{\text{matrix}}\phi_{\text{matrix}} \gg V_{\text{fracture}}\phi_{\text{fracture}} \quad . \tag{9.2}$$

As a result of production, a pressure difference between matrix and fracture develops, and the matrix will supply fluid to the fractures. This oil is subsequently produced through the fracture system as illustrated in Fig. 9.3

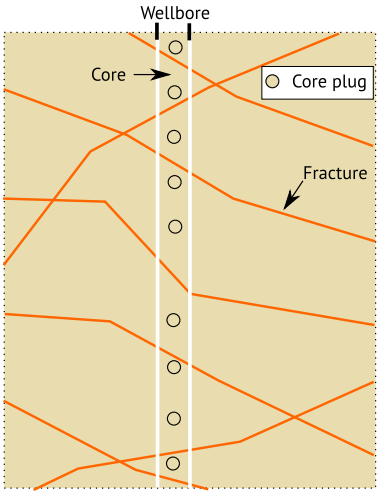


Figure 9.2: A cored well in a fractured reservoir. The permeability of the core plugs represent the matrix and is not representative for formation permeability which describes flow in the fractures.

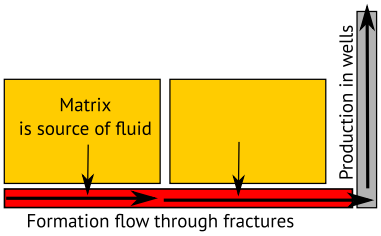


Figure 9.3: Flow in a dual porosity system.

In well testing, dual porosity systems are analyzed in terms of the dual porosity model commonly used in reservoir simulation. The dual porosity model is a macroscopic model where the representative elementary volume (REV) contains many matrix blocks. The fractures are thus not explicitly modelled, in stead each point in space (REV) is modelled as having two sets of dynamic variables, one set for matrix, and one set for fractures:

- Two pressures, matrix pressure p_m, and fracture pressure p_f.
- Two set of saturations, matrix saturations (S_{om}, S_{wm}, and S_{gm}), and fracture saturations (S_{of}, S_{wf}, and S_{gf}).
- The oil and gas in matrix and fracture can also have different fluid composition (in the BO-model: R_{sm} and R_{sf}).

In terms of static variables the dual porosity model is described using one permeability (the bulk permeability of the fracture system k_{fb}), two porosities (the bulk fracture porosity ϕ_{fb}, and the bulk matrix porosity ϕ_{mb}), and a matrix–fracture coupling term, σ, which describe the ability of the matrix to supply fluid to the fractures. Note that the permeability k_{fb} is not the permeability in the fractures, it is the effective permeability of the formation, and that the porosities are bulk porosities, i.e.

$$\begin{aligned} \phi_{fb} &= \frac{\text{Pore volume in fractures}}{\text{Total volume}} \\ \phi_{mb} &= \frac{\text{Pore volume in matrix}}{\text{Total volume}} \end{aligned} \quad . \tag{9.3}$$

How the dual porosity parameters are actually specified in various reservoir simulation software does however differ between simulators.

The dual porosity model is often visualized in terms of the Warren and Root “sugar cube” model, where the matrix is a set of equal rectangular cuboids as illustrated in Fig. 9.1. The validity of the dual porosity model is however not limited to this picture.

9.2 The diffusivity equation for dual porosity

In this section a diffusivity equation will be developed for the dual porosity model, and the main dimensionless parameters that characterize the solutions to this equation will be identified.

The equation for the flow in the fracture system is similar to the ordinary single porosity hydraulic diffusivity equation (2.13), but the flow from the matrix into the fractures must be accounted for:

$$\frac{k_{fb}}{\mu}\nabla^2 p_f + \sigma_{mf} = \phi_{fb} c_{tf} \frac{\partial}{\partial t} p_f \quad . \tag{9.4}$$

Here σ_{mf} is the volume of liquid flowing from matrix to fracture per time and bulk volume, and Eq. (9.4) expresses the mass balance in the fracture system. There is no bulk flow in the matrix system, so there the mass balance is simply expressed as

$$\phi_{mb} c_{tm} \frac{\partial}{\partial t} p_m = -\sigma_{mf} \quad . \tag{9.5}$$

The two equations (9.4) and (9.5) are coupled through an equation for matrix–fracture flow. In the standard dual porosity model this flow is proportional to the pressure difference:

Flow from matrix to fracture is proportional to the pressure difference.

$$\sigma_{mf} = \frac{\sigma}{\mu}(p_m - p_f) \quad , \tag{9.6}$$

where σ is the matrix–fracture coupling. If the permeability in the matrix blocks is homogeneous, and the matrix blocks are of similar shape and size, it follows from Darcys law that σ is proportional to the matrix permeability. Eq. (9.6) is therefore usually written as

$$\sigma_{mf} = \alpha \frac{k_{mb}}{\mu}(p_m - p_f) \quad , \tag{9.7}$$

where

Shape factor

$$\alpha = \frac{\sigma}{k_{mb}} \tag{9.8}$$

is called the shape factor, and

$$k_{mb} = \frac{V_m}{V_m + V_f} k_m \quad . \tag{9.9}$$

where V_m is the volume of matrix, V_f is the fracture volume, and k_m is the permeability of the matrix rock. The matrix–fracture coupling, σ, is dimensionless, while the shape factor, α has dimension of inverse area. We will see later (on page 103, see Eq. (9.46)) that the shape factor can be interpreted as $\alpha = \frac{1}{h_m^2}\alpha'$, where α' is a pure geometric factor representing the shape of the matrix blocks, while h_m is the typical matrix block size.

For further analysis we will express Eqs. (9.4)–(9.6) on dimensionless form using the following variables and parameters:

Dimensionless variables for the dual porosity model

$$\begin{array}{ll} x_D = \dfrac{x}{r_w} & t_D = \dfrac{k_{fb} t}{(\phi_{mb} c_{tm} + \phi_{fb} c_{tf})\mu r_w^2} \\ p_D = \dfrac{2\pi k_{fb} h}{Q\mu}(p_i - p) & \\ \lambda = \dfrac{r_w^2}{k_{fb}}\sigma & \omega = \dfrac{\phi_{fb} c_{tf}}{\phi_{fb} c_{tf} + \phi_{mb} c_{tm}} \end{array} \quad . \tag{9.10}$$

Now Eq. (9.6) can be substituted in Eq. (9.5), and then we have two coupled equations: One for the flow in the fracture system

$$\boxed{\nabla_D^2 p_f + \lambda(p_m - p_f) = \omega \frac{\partial p_f}{\partial t_D}} \quad , \tag{9.11}$$

and one for the mass balance in the matrix.

$$\boxed{(1-\omega)\frac{\partial p_m}{\partial t_D} = -\lambda(p_m - p_f)} \quad . \tag{9.12}$$

Note that these equations holds for pressures both on normal and dimensionless form.

Compared to a single porosity system, the dual porosity system is characterized by two additional dimensionless parameters. These parameters are the storativity ratio

Storativity ratio

$$\omega = \frac{\phi_{fb} c_{tf}}{\phi_{fb} c_{tf} + \phi_{mb} c_{tm}} \quad , \tag{9.13}$$

and the inter-porosity flow parameter

Inter-porosity flow parameter

$$\lambda = \frac{r_w^2}{k_{fb}}\sigma = \frac{k_{mb} r_w^2}{k_{fb}}\alpha \quad . \tag{9.14}$$

The storativity ratio express how much of the total compressibility can be attributed to the fractures, and in a fractured reservoir ω is small: $\omega < 10^{-2}$. In other systems with dual porosity like properties, such as certain high contrast layered formations, ω can be larger. The inter-porosity flow parameter express the strength of the fracture–matrix coupling, that is the ability of the matrix to supply fluid to the fracture system. Typical values for λ is in the range 10^{-3} to 10^{-9}.

9.2.1 Solution in the Laplace domain

We will analyze the equation system (9.11) and (9.12) in terms of the Laplace transform (see page 87). The Laplace transformed equation for flow in the fracture system (Eq. (9.11)) is

$$\nabla^2 \tilde{p}_f + \lambda(\tilde{p}_m - \tilde{p}_f) = \omega s \tilde{p}_f \quad , \tag{9.15}$$

and the equation for mass balance in the matrix (Eq. (9.12)) is

$$(1-\omega)s\tilde{p}_m = -\lambda(\tilde{p}_m - \tilde{p}_f) \quad . \tag{9.16}$$

To simplify notation, we always assume dimensionless numbers in the Laplace domain. Using Eq. (9.16), the matrix pressure can be expressed in terms of the fracture pressure as

Equations in the Laplace domain are on dimensionless form.

$$\tilde{p}_m = \frac{\lambda}{(1-\omega)s + \lambda}\tilde{p}_f \quad , \tag{9.17}$$

and this can be substituted in Eq. (9.15) to get the equation in Laplace space for the fracture pressure:

$$\boxed{\left(\nabla^2 - s\frac{\omega(1-\omega)s + \lambda}{(1-\omega)s + \lambda}\right)\tilde{p}_f = 0} \quad . \tag{9.18}$$

Since the wells produce from the fracture system, and there is no macroscopic matrix flow, this is the equation that is relevant for well testing.

We can define the following function

$$f(s,\lambda,\omega) = s\frac{\omega(1-\omega)s+\lambda}{(1-\omega)s+\lambda} \quad , \tag{9.19}$$

then Eq. (9.18) is simplified to the following form:

$$\left(\nabla^2 - f\right)\tilde{p}_f = 0 \quad . \tag{9.20}$$

The limiting behavior of the function $f(s,\lambda,\omega)$ will play an important role in the well test interpretation.

For a well test in a fully penetrating vertical well we are interested in the radial version of Eq. (9.20):

$$\left(\frac{d^2}{dr^2} + \frac{1}{r}\frac{d}{dr} - f(s)\right)\tilde{p}_f = 0 \quad . \tag{9.21}$$

This can be rearranged to the following equation:

$$\left(\chi^2\frac{d^2}{d\chi^2} + \chi\frac{d}{d\chi} - \chi^2\right)\tilde{p}_f = 0 \quad , \tag{9.22}$$

where $\chi = r\sqrt{f(s)}$. Equation (9.22) is the modified Bessel's equation[1] with constant equal 0. The general solution to Eq. (9.22), or equivalently to Eq. (9.21), is

$$\tilde{p}_f(r,s) = A\,\mathrm{I}_0\left(r\sqrt{f(s)}\right) + B\,\mathrm{K}_0\left(r\sqrt{f(s)}\right) \quad , \tag{9.23}$$

where A and B are constants determined by the boundary conditions, and $\mathrm{I}_0(\cdot)$ and $\mathrm{K}_0(\cdot)$ are modified Bessel functions of first and second kind. A plot of the Bessel functions $\mathrm{I}_0(\cdot)$ and $\mathrm{K}_0(\cdot)$ is shown in Fig. 9.4. From this plot we observe that the function $\mathrm{I}_0(x)$ grows and $\mathrm{K}_0(x)$ decreases with increasing x. Then the boundary condition $p_D(\infty,s) = 0$ implies that $A = 0$.

[1] For the modified Bessel's equation and its solutions, see https://en.wikipedia.org/wiki/Bessel_function.

Darcys law determines the boundary condition at the well ($r = 1$, remember that we are on dimensionless form in the Laplace domain) which in the Laplace domain is (see Eq. (8.17))

$$\left.\frac{d\tilde{p}_f}{dr}\right|_{r=1} = -\frac{1}{s} \quad . \tag{9.24}$$

By combining Eq. (9.24) and (9.23), and using

$$\frac{d}{dz}\mathrm{K}_0(z) = -\mathrm{K}_1(z) \quad , \tag{9.25}$$

we can solve for B:

$$\begin{aligned}
\frac{d\tilde{p}_f}{dr} &= B\frac{\partial}{\partial r}\mathrm{K}_0\left(r\sqrt{f(s)}\right) = -B\mathrm{K}_1\left(r\sqrt{f(s)}\right)\sqrt{f(s)} \\
\left.\frac{d\tilde{p}_f}{dr}\right|_{r=1} &= -B\mathrm{K}_1\left(\sqrt{f(s)}\right)\sqrt{f(s)} = -\frac{1}{s} \\
B &= \frac{1}{s\mathrm{K}_1\left(\sqrt{f(s)}\right)\sqrt{f(s)}} \quad ,
\end{aligned} \tag{9.26}$$

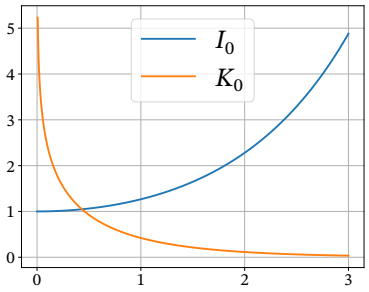


Figure 9.4: The modified Bessel functions I_0 and K_0.

which gives the following general solution for the pressure:

$$\tilde{p}(s) = \frac{\mathrm{K}_0\left(r\sqrt{f(s)}\right)}{s\sqrt{f(s)}\,\mathrm{K}_1\left(\sqrt{f(s)}\right)} \quad . \tag{9.27}$$

As we have $r = 1$ at the well, Eq. (9.27) reduce to the following solution for the well pressure:

$$\boxed{\tilde{p}_w(s) = \frac{\mathrm{K}_0\left(\sqrt{f(s)}\right)}{s\sqrt{f(s)}\,\mathrm{K}_1\left(\sqrt{f(s)}\right)}} \quad . \tag{9.28}$$

To get an expression for the well test response, we need to get the inverse transform of Eq. (9.28). An explicit expression for the inverse, and thus for the the pressure as a function of time, has not been found. However, the early time and late time behavior can be analyzed based on the large s and small s limits of $f(s)$. The middle time behavior can in a similar way be approximately analyzed under some extra assumptions on ω and λ. The inverse transform can also be evaluated numerically. We will in the following analyze the early and late time behavior and investigate how the well test may be analyzed.

The early time and late time behavior of the well test can be analyzed based on the large s and small s limits of $f(s, \lambda, \omega)$ (Eq. (9.19)).

From Eq. (8.6) we have that the Laplace transform of time is $1/s^2$, thus early times (small t_D) correspond to large s. Further, we see from Eq. (9.19) that for large s we have

$$f(s, \lambda, \omega) \approx s\omega \quad . \tag{9.29}$$

Similarly, for late times ($s \to 0$) we have

$$f(s, \lambda, \omega) \approx s \quad . \tag{9.30}$$

For $f = s\omega$, we see that Eq. (9.20) is $(\nabla^2 - s\omega)\tilde{p}_f = 0$, which corresponds to the following inverse of the the Laplace transform:

$$\nabla_D^2 p_f = \omega \frac{\partial p_f}{\partial t_D}. \tag{9.31}$$

Similarly, for $f = s$, we see that Eq. (9.20) is $(\nabla^2 - s)\tilde{p}_f = 0$, which corresponds to the following inverse of the the Laplace transform:

$$\nabla_D^2 p_f = \frac{\partial p_f}{\partial t_D}. \tag{9.32}$$

Thus, at early and late time we are back to the dimensionless diffusivity equation, representing a infinite acting system. These early and late time systems are similar up to a scaling of dimensionless time t_D by the constant ω.

We see from the definition of ω (Eq. (9.13)) and the dimensionless time t_D (Eq. (9.10)) that

$$\frac{t_D}{\omega} = \frac{k_{fb}t}{(\phi_{mb}c_{tm} + \phi_{fb}c_{tf})\mu r_w^2} \frac{\phi_{fb}c_{tf} + \phi_{mb}c_{tm}}{\phi_{fb}c_{tf}} = \frac{k_{fb}t}{\phi_{fb}c_{tf}} \tag{9.33}$$

thus a division of dimensionless time t_D with ω switches between a system with the total compressibility of fractures *and* matrix to a system with *only fracture* compressibility. Also from the definition of

[2] Laplace transform: $\tilde{f}(s) = \int_0^\infty f(t)e^{-st}\,dt$

the Laplace transform[2], multiplying s with ω corresponds to dividing time with ω. Accordingly, $f = s$ represents the infinitely acting system with total compressibility, and $f = s\omega$ represents the infinitely acting system with fracture compressibility.

If we have no matrix–fracture flow ($\lambda = 0$) the system will be single porosity with only the fracture system active, and by setting $\lambda = 0$ in Eq. (9.19) we get

$$f(s, 0, \omega) = s\omega \quad . \tag{9.34}$$

This gives the same pressure equation as for the early time behavior, thus the early time behavior ($f = s\omega$) is single porosity infinitely acting with fracture compressibility. Similarly, the late time behavior ($f = s$) is single porosity infinitely acting with total compressibility.

Both early and late time in an infinitely acting well test in a dual porosity system show single porosity behavior.

We see from the dimensionless expression for the infinitely acting single porosity well test (3.49), and Eq. (9.31) that the early time dimensionless well pressure is

$$p_{D\,\text{early}} = \frac{1}{2}\left(\ln\left(\frac{t_D}{\omega}\right) + a + 2S\right) \quad , \tag{9.35}$$

where $a = \ln(4) - \gamma \approx 0.8091$. Similarly, from Eq. (9.32) the late time pressure is

$$p_{D\,\text{late}} = \frac{1}{2}\left(\ln(t_D) + a + 2S\right) \quad . \tag{9.36}$$

The time when cross-over from early to late time behavior occurs is related to λ. By inspecting Eq. (9.19) we see that we have early time behavior when

$$\omega(1-\omega)s \gg \lambda \implies t_D \ll \frac{\omega(1-\omega)}{\lambda} \quad , \tag{9.37}$$

and late time behavior when

$$(1-\omega)s \ll \lambda \implies t_D \gg \frac{1-\omega}{\lambda} \quad . \tag{9.38}$$

Ideally dual porosity behavior will manifest itself as two parallel straight lines in a semilog plot, as illustrated in Figs. 9.5 and 9.6, and a dip on the log–log derivative diagnostic plot.

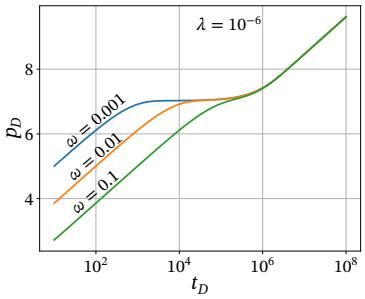


Figure 9.5: Dimensionless semilog plot of dual porosity with varying ω from $\omega = 0.1$ in green to $\omega = 0.001$ in blue.

Combining Eq. (9.35) and (9.36), we see that the separation of the two lines in dimensionless time, that is at fixed pressure $p_{D\,\text{early}}(t_1) = p_{D\,\text{late}}(t_2)$ for dimensionless times t_i, gives

$$\frac{t_1}{t_2} = \omega \quad , \tag{9.39}$$

as can be seen in in Figs. 9.5 and 9.6. Likewise, the separation in dimensionless pressure at a fixed time t_D gives

$$p_{D\,\text{early}}(t_D) - p_{D\,\text{late}}(t_D) = -\frac{1}{2}\ln(\omega) \quad . \tag{9.40}$$

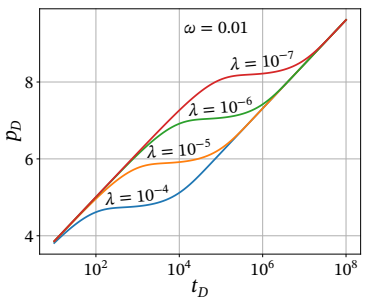


Figure 9.6: Dimensionless semilog plot of dual porosity with varying λ from $\lambda = 10^{-7}$ in red to $\lambda = 10^{-4}$ in blue.

In a fractured reservoir, the time where the late time behavior starts (Eq. (9.38)) is (almost) independent of ω since $1 - \omega \approx 1$. A small λ, i.e. poor matrix fracture coupling, corresponds to late start of late time behavior, and a large λ corresponds to early start. Note also that $\omega < 1$, so that $\ln(\omega) < 0$, which means that a small ω corresponds to a large separation of the two lines.

As mentioned earlier, no explicit expression for the well pressure as a function of time exist. Finding the inverse of the Laplace transform for arbitrary times require numerical inversion. The inversion of Laplace transforms is in general a hard problem, and there exist no general algorithm for the inversion. However, since we here have an explicit expression for the Laplace transformed pressure, and since the pressure has a nice monotonic behavior, a number of possible algorithms do exist. In cases where we only know the Laplace transformed pressure for a number of discrete values of s, the selection of algorithms is much more restricted, but an algorithm that is suitable for the kind of functions that occur in well testing is the Stehfest algorithm. This algorithm will be discussed in more detail later (see page 128).

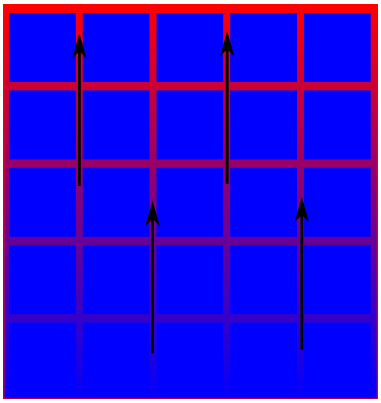


Figure 9.7: Radial fracture flow; Flow only in fractures, matrix is undisturbed.

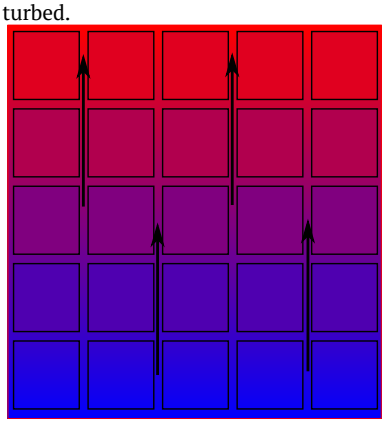


Figure 9.8: Radial bulk flow; Matrix and fracture pressure in equilibrium.

9.3 Flow periods

In this section we will give a qualitative presentation of the flow regimes and corresponding flow periods that were identified in the preceding section.

The first flow period is radial fracture flow, that is radial flow in the fracture system. The pressure front spreads radially from the well, and the matrix–fracture flow is negligible since the necessary pressure difference has not yet been developed. Since diffusivity of the radial flow in this period is determined by the small fracture storativity, $\phi_{fb}c_{tf}$, the pressure front is spreading relatively fast. Radial fracture flow is illustrated in Fig. 9.7.

The late flow period is radial bulk flow, where fractures and matrix are in quasi-equilibrium and the pressure front spreads with the same speed in both fractures and matrix. Since diffusivity of the radial flow in this period is determined by the larger total storativity, $\phi_{fb}c_{tf} + \phi_{mb}c_{tm}$, the pressure front is spreading relatively slower than in the first period[3]. Radial bulk flow is is illustrated in Fig. 9.8.

The intermediate flow period is a transition period with matrix–fracture equilibration. The spread of the pressure front slows down in the transition period, and the matrix–fracture flow is in a transient state as illustrated in Fig. 9.9. The transition will show up as a pronounced dip on the log-derivative diagnostic plot, and in the period after the dip minimum, the slope on the diagnostic plot will be close to 1, similar to constant drainage of a finite volume (see Fig. 9.10)It should be noted that the nature of the transition period is dependent on how the matrix–fracture coupling is modelled. In alternative "transient models" the dip in log-derivative will not be as pronounced [4].

[3] The *absolute* speed of the pressure front is proportional $t^{-\frac{1}{2}}$ (eq. 3.25), so it is always slowing with time. The relative speed discussed here refers to the proportionality constant.

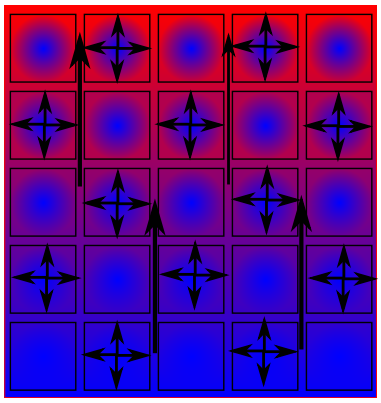


Figure 9.9: Transition period with matrix–fracture equilibration; Transient pressure gradient driving flow in matrix blocks.

[4] See George Stewart:"*Well test design and analysis*" pages 582-586 for a discussion of transient models).

9.4 Analyzing a drawdown test

Both early and late time behavior of a dual porosity system is similar to a single porosity system, which means that in these two time peri-

ods the pressure will be a straight line on a semilog plot. We will now show how these two straight lines and their separation can be used to get estimates for formation permeability, k_{fb}, matrix–fracture coupling, σ, and storativity ratio, ω. In practice the first straight line is often hidden by wellbore storage and near near well effects. However, a dual porosity system will also show a dip on the log–log derivative diagnostic plot, and a fit to log–log derivative data, a variant of type curve matching, can also give estimates for σ and ω.

We will first discuss the analysis based on semilog plot where, ideally, dual porosity behavior will manifest itself as two parallel straight lines as shown in Fig. 9.10.

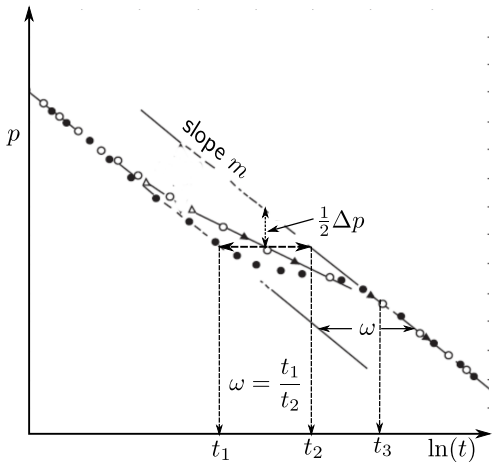


Figure 9.10: Semilog plot with dual porosity behavior

The second straight line is used in the usual manner to get estimates for bulk permeability, k_{fb}, and skin, S. The length of the radial fracture flow period depends on λ (see Fig. 9.6), and the first straight line is often only seen when λ is very small. In the cases it is apparent, the semilog plot can be used to find ω and λ (see Fig. 9.10). As shown in Fig. 9.10 two dimensionless times t_1 and t_2, can be found based on the pressure in the middle of the transition. The storativity ratio is estimated based on the separation of the two lines (Eq. (9.39) and (9.40)):

$$\boxed{\omega = \frac{t_1}{t_2}} \quad . \tag{9.41}$$

and an estimate for λ is found based on either of the two times:[5]

$$\boxed{\lambda = \frac{0.561 \cdot (\phi_{mb} c_{tm} + \phi_{fb} c_{tf}) \mu r_w^2}{k_{fb} t_2} = \frac{0.561 \cdot \phi_{fb} c_{tf} \mu r_w^2}{k_{fb} t_1}} \tag{9.42}$$

The numerical factor (0.561) is based on an analysis of the intermediate period and on numerical inversion of Eq. (9.28). One should not expect Eq. (9.42) to give very accurate estimates for λ. A third time t_3 is defined as the start of the late time period based on visual inspection of the log–derivative plot. The time t_3 can also used for estimating λ:

$$\boxed{\lambda = \frac{4(\phi_{mb} c_{tm} + \phi_{fb} c_{tf}) \mu r_w^2}{k_{fb} t_3}} \quad . \tag{9.43}$$

[5] Alain C. Gringarten. "Interpretation of Tests in Fissured and Multilayered Reservoirs With Double-Porosity Behavior: Theory and Practice." In: *Journal of Petroleum Technology* (Apr. 1984), pp. 549–564. DOI: 10.2118/10044-PA.

The numerical factor (4) is again based on numerical inversion.

9.4.1 Derivative analysis

Early time dual-porosity behavior is usually suppressed by wellbore storage and near wellbore effects. However, the log–derivative will have a dip with a minimum which depends on ω. For large times (and small ω) the dimensionless pressure log–derivative is a function of $t_D\lambda$. Based on these observations a number of type curves can be created by numerically inverting Eq. (9.28) for various combinations of these parameters. Examples of such type curves are shown in Fig. 9.11. With known permeability, λ and ω can be found by fitting the end of transition period to a type-curve by adjusting the two parameters as shown in Fig. 9.12. This is an example of a general method much used in well test analysis: fitting to type curves. Several other examples of type curves for the analysis of dual porosity systems are given in the review article by Alain C. Gringarten.[6]

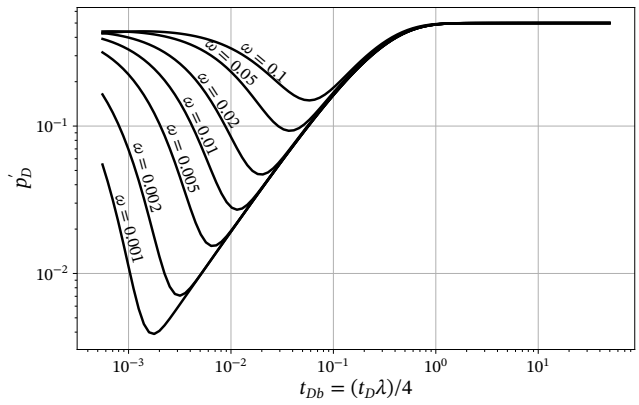


Figure 9.11: Example of a type curve for log–log derivative diagnostic plot with dual porosity behavior.

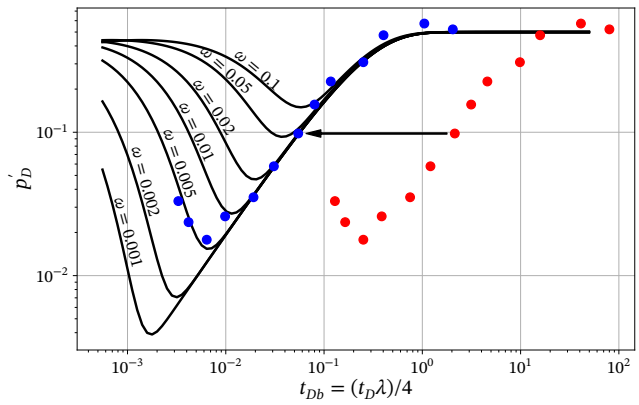


Figure 9.12: Finding λ and ω by fitting to a log–log derivative type curve: Early time data that are influenced by wellbore storage and skin are removed. Data points are moved horizontally by adjusting λ, and ω is found based on the minimum.

Fitting data to a type curve is a much used method in well test analysis.

In a dual porosity simulator, the parameters that characterize the system are k_{fb}, σ, ϕ_{fb}, and ϕ_{mb}, and based on the estimates for λ and ω we have

$$\sigma = \frac{k_{fb}}{r_w^2}\lambda \quad \text{and} \quad \phi_{fb} = \frac{\omega}{1-\omega}\phi_{mb} \quad , \tag{9.44}$$

[6] Gringarten, "Interpretation of Tests in Fissured and Multilayered Reservoirs With Double-Porosity Behavior: Theory and Practice."

where ϕ_{mb} is based on core plug measurements. It should however be noted that the way these parameters are actually specified in different simulators will vary. In the "industry standard" simulator ECLIPSE the matrix–fracture coupling is for instance specified by giving the matrix permeability and the shape factor separately (Eq. (9.7)).

Physically the matrix–fracture flow depend on matrix block permeability, k_{mb}, matrix block geometry, and the characteristic matrix block size, h_m. Given an estimate for λ and some prior knowledge of matrix block geometry, it should therefore be possible to say something about matrix block size. If all matrix blocks have the same size and shape, we could express Eq. (9.7) as

$$\sigma_{mf} = \frac{\sigma}{\mu}(p_m - p_f) = \left(\frac{\alpha'}{h_m}\right)\left(\frac{k_{mb}}{\mu}\right)\left(\frac{(p_m - p_f)}{h_m}\right) \quad . \tag{9.45}$$

The first term is proportional to matrix-block area per volume, and is the product of a pure geometric factor α' and h_m^{-1}, and the last term is the pressure gradient, which is the driving force for flow. Eq. (9.45) gives

$$\sigma = \frac{k_{mb}}{h_m^2}\alpha' \quad , \tag{9.46}$$

so the characteristic matrix block size is

$$h_m = \frac{\sqrt{\alpha'}}{\lambda}\sqrt{\frac{k_{mb}}{k_{fb}}}\, r_w \quad . \tag{9.47}$$

Examples of the geometrical factor α' for various matrix block geometries are shown in Fig. 9.13.

Based on Eq. (9.47) it is in principle possible to estimate matrix block size from λ if we know something about block shape. Since actual block sizes vary throughout the formation, this estimate is in any case only an indication of a typical size, and due to diagenesis, fracture walls are additionally often covered with calcite cement. In these cases, the measured λ from well-testing is insufficient for estimating block size.

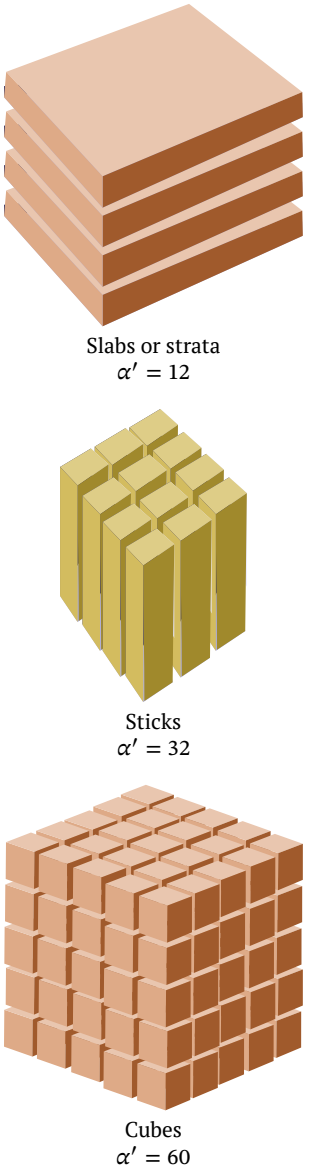


Figure 9.13: Geometrical factor α' for various matrix block geometries

9.5 Skin in fractured reservoirs

Since it is assumed that a representative elementary volume contain many fractures, the dual porosity model is a macroscopic model which is valid only on length scales much larger than the matrix block size. This means that the model is not valid for near wellbore flow. This fact contribute to the suppression of early time dual–porosity behavior in real well tests, and is also important for the interpretation of the physical significance of a measured skin in the well. If the well intersects the fracture system, pressure drops will be significantly less than predicted by the dual porosity model. The reason for this is that the flow follows the fractures so that the near well flow pattern will not have the logarithmic convergence close to the well that is responsible for much of the pressure drop in an equivalent single porosity model (see Fig. 9.14). Based on flow in a network, wells with fracture system contact should have a negative skin. The negative skin is larger

for large matrix block sizes, and for a square network an approximate formula is

$$S \approx \frac{\pi}{2} - \ln(\frac{h_m}{r_w}) \quad . \tag{9.48}$$

This approximation is only valid for matrix block sizes $h_m > 5r_w$.

Wells that do not intersect fractures have larger pressure drops than predicted, and a corresponding large positive skin. The missing fracture–well contact introduce an area around the well with reduced permeability (matrix permeability k_m) compared to the effective permeability of the formation (bulk fracture permeability k_{fb}), and if we use the formula for a circular damage area we get the following approximate expression for skin

$$S \approx \left(\frac{k_{fb}}{k_m} - 1\right) \ln(\frac{h_m}{2r_w}) \quad . \tag{9.49}$$

It should be noted that wells in fractured reservoirs are usually acidized or hydraulically fractured to obtain good communication with the fracture system. A successful well stimulation will result in a large negative skin.

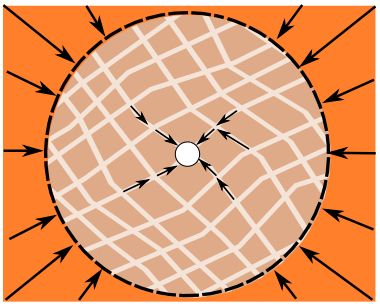


Figure 9.14: A well located in a fracture system. Beyond a distance $r \gtrapprox 16h_m$, the reservoir behaves like an effective dual porosity system, with radial flow towards the well. In the inner region the flow pattern is determined by the discrete fracture network.

9.6 Validity of model

The dual porosity model is a macroscopic theory based on the representative elementary volume (REV) concept. The short and early middle time behavior of a well test in a fractured reservoir will however often correspond to length scales than are smaller than the REV. This implies that any analysis of these time periods based on the dual porosity model is approximate at best. The relevance of type curves used for well storage and skin correction can for instance be questioned, as it is not expected that the dual porosity model can describe the corresponding time periods well.

Fracture systems are often localized. Two examples are shown in Fig. 9.15; fractures that are clustered in a fracture zone near a large fault, and fractures that are located in regions of high stress such as the top of an anticline. Such systems can not be analyzed in terms of a simple dual porosity model with homogeneous properties. A well in a fractured zone on the top of an anticline should for instance be analyzed in terms of a chanalized system (see page 72), and in this context the well test can be used to estimate the extent of the fractured zone.

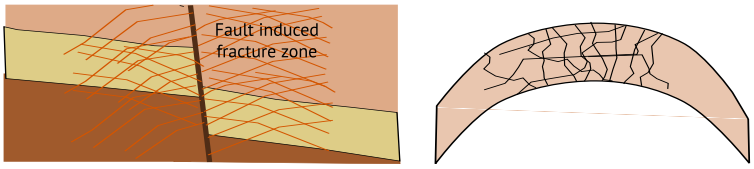


Figure 9.15: Examples of localized fracture systems. Fractures near a fault zone, and located in a high stress zone at the top of an anticline.

Some fracture systems are highly irregular in the sense that fracture and matrix block sizes have a large variation. Typically the variation can span several orders of magnitude and the system approaches

[7] Fractals are systems with no characteristic length scale.

fractal behavior[7]. To capture the behavior of such systems, large fractures must be explicitly modelled, while the smaller fractures may be included as dual porosity.

The dual porosity model has a single variable set representing the inner state of the matrix blocks. This is a good approximation if the pressure profile in the matrix blocks have reached a semi steady state, and due to this the model is often called the pseudo-semi-steady-state (PSSS) inter-porosity flow model. In reality the real profile will have a transient behavior. Multi porosity models is an attempt to include these transients by describing the inner state of the matrix with more variables, each describing layers within matrix blocks. In particular, the model often known as the "transient interporosity model" is a continuous variant of a multi-porosity model.

Multi porosity models.

In real systems, matrix blocks have a varying shape and size, while multi porosity models assume a given shape and size for all blocks. Thus, the actual transient behavior may not be well described by these models. Also due to diagenesis, the fracture walls are often covered with calcite cement, and the matrix–fracture pressure drop will be localized over these barriers. In these cases, a semi-steady-state is developed early.

The dual–porosity and dual–porosity–dual–permeability model may also be applicable in layered systems. Layer communication is governed by diagenetic or depositional barriers of unknown extent and strength. Dual porosity layer communication (λ) can be obtained from well test data.

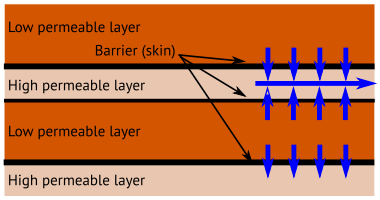


Figure 9.16: Layered system with dual porosity like behavior.

9.7 Final comments

Dual porosity effects are elusive and may not be readily accessible by well testing for all systems where they are important in production.

A number of heterogeneous systems show well test responses that can be mis-interpreted as dual porosity effects. The occurrence of natural fractures must be established from the inspection of whole core or well logs before applying the dual porosity model for well test interpretation. Note, however, that high-contrast heterogeneous or layered systems may also show dual-porosity dual-permeability behavior and the use of these models need not be limited to naturally fractured reservoirs.

Fractured reservoirs with large matrix–fracture coupling are effectively single porosity, but the effective permeability can only be measured by well testing.

10
Gas reservoirs

The objectives of well testing in gas wells are the same as in oil and water wells. The well test gives estimates for formation permeability, and probe reservoir structure such as the location of faults. The test can also contribute to reservoir and well monitoring by giving reservoir pressure and skin. Due to high flow rates, the skin in gas wells is however often rate dependent, and multi rate testing is needed for skin estimation.

The analysis methods used in oil-well testing can however not be directly applied to the testing of gas wells. The reason for this is that the fluid properties have a stronger pressure dependency; compressibility and viscosity can not be treated as a constants, and constant surface volume rates corresponds to variable down-hole rates. We will in this chapter show that some smart tricks, in particular the concept known a s pseudo-pressure, can be employed so that the familiar analysis methods can, at least approximately, still be applied.

Before any major approximations have been made, the general equation for the pressure is (see page 15)

$$\nabla \cdot \left(\frac{k\rho(p)}{\mu(p)} \nabla p \right) = \phi c_t(p) \rho(p) \frac{\partial}{\partial t} p \quad . \tag{10.1}$$

In gas reservoirs, the diffusivity equation is non-linear.

Since the parameters, ρ, μ, and c_t depend on pressure, Eq. (10.1) is non-linear (see page 39 for the definition of a linear partial differential equation). All of the methods developed over the preceding chapters are derived under the condition that the governing equation (2.13) is linear. Thus, in order to take advantage of these methods, Eq. (10.1) must be approximately linearized by a change of variables p or t. The new variable replacing pressure is called pseudo-pressure, and the use of this variable instead of pressure in the analysis is standard procedure in gas well testing. The introduction of an additional variable change for time, that is pseudo-time, may reduce non linearities further in some cases, and can be introduced in cases when the total pressure change in the test is large.

10.1 Pseudo pressure

In order to take advantage of the methods developed for the testing of oil wells in gas well testing, Eq. (10.1) must be linearized. We will

show that the equation can be approximately linearized by a variable change as long as the total pressure change is not too large. Thus, if the total pressure change in the test period is small, well test in gas reservoirs can be analyzed using the same methods and equations as for oil reservoirs provided that pressure is replaced by pseudo-pressure in the analysis.

Pseudo-pressure

Pseudo-pressure ψ is defined as

$$\boxed{\psi(p) = \frac{\mu_i}{\rho_i}\int_{p_0}^{p}\frac{\rho(p')}{\mu(p')}\,dp' \quad ,} \quad . \tag{10.2}$$

where p_0 is some reference pressure, and μ_i and ρ_i are viscosity and density at initial reservoir pressure. The differential equation for pseudo pressure is

$$k\nabla^2\psi = \phi c_t(p)\mu(p)\frac{\partial}{\partial t}\psi \quad . \tag{10.3}$$

Note that the choice for reference pressure p_0 is arbitrary, as Eq. (10.2) only contains derivatives of the pseudo-pressure.

Applying the fundamental theorem of calculus, we obtain the following:

$$\begin{aligned}\nabla\psi(p) &= \frac{\partial\psi}{\partial p}\nabla p = \frac{\mu_i}{\rho_i}\frac{\rho(p)}{\mu(p)}\nabla p \\ \frac{\partial}{\partial t}\psi(p) &= \frac{\partial\psi}{\partial p}\frac{\partial}{\partial t}p = \frac{\mu_i}{\rho_i}\frac{\rho(p)}{\mu(p)}\frac{\partial}{\partial t}p \quad .\end{aligned} \tag{10.4}$$

Using the equality's above, we can show that Eq. (10.3) is equivalent with Eq. (10.1). The formulation using pseudo pressure (Eq. 10.3) does not introduce any extra approximations to the full nonlinear formulation (Eq. (10.1)), and it is still nonlinear as the right hand side is pressure dependent.

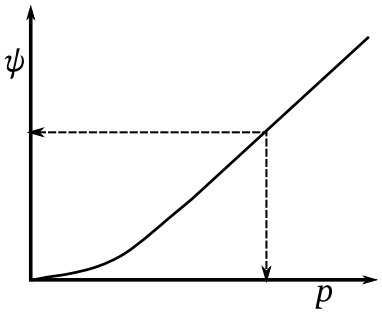


Figure 10.1: Pseudo pressure is a monotonous function of pressure

Pseudo pressure, ψ, has dimension pressure and is a monotonous function of pressure. Note also that ψ is a pure fluid property, by that we mean that it is a characteristic of a given reservoir fluid. The same pseudo-pressure function, $\psi(p)$, applies to all tests in wells in a given reservoir.

The pseudo-pressure function, $\psi(p)$, is a pure fluid property.

To obtain the pseudo pressure a good model for the density and viscosity as a function of pressure is needed. This model should be based on on some key measurements performed on the reservoir fluid, including compositional analysis. These measurements can be used to create a tuned equation of state and viscosity correlation.

In many textbooks the pseudo pressure is expressed using the compressibility factor, $Z(p)$:

$$\psi(p) = \frac{\mu_i Z_i}{p_i}\int_{p_0}^{p}\frac{p'}{\mu(p')Z(p')}\,dp' \quad . \tag{10.5}$$

Since $\rho(p) \propto p/Z(p)$, this definition is identical to the definition in Eq. (10.2). Note, however, that it is also common in many text to use the so called un-normalized pseudo pressure, $m(p)$, which is defined as

Un-normalized pseudo pressure

$$m(p) = 2\int_{p_0}^{p} \frac{p'}{\mu(p')Z(p')}\,dp' \quad . \tag{10.6}$$

$m(p)$ does not have the dimension of pressure, and numerical values are very different from the corresponding true pressures. In all other aspects, $m(p)$ and $\psi(p)$ are interchangeable.

10.1.1 Pseudo pressure in low pressure reservoirs (p^2 analysis)

If the reservoir pressure is low it can be modelled as an ideal gas. Thus, the density is determined by the ideal gas law,

$$\rho(p,T) = \frac{p}{RT} \quad , \tag{10.7}$$

and the viscosity is independent of pressure. The pseudo pressure is then

$$\psi(p) = \frac{1}{2p_i}(p^2 - p_0^2) \quad . \tag{10.8}$$

Inserting Eq. (10.8) into Eq. (10.3) then yields

$$k\nabla^2 p^2 = \phi c_t(p)\mu \frac{\partial}{\partial t} p^2 \quad . \tag{10.9}$$

Well test analysis in the low pressure regime thus amounts to replacing pressure with the pressure squared, and is therefore called p^2-analysis.

We can further simplify Eq. (10.9) by assuming that the total compressibility for a gas can be approximated by the liquid compressibility, $c_t \simeq c_l$, and that the liquid compressibility for an ideal gas can be approximated as $c_l \simeq 1/p$:

$$k\nabla^2 p^2 = 2\phi\mu \frac{\partial}{\partial t} p \quad . \tag{10.10}$$

At reservoir temperatures in the range 50–150 °C, the approximations above are accurate for pressures $p < 140$ bar.

10.2 Analyzing tests using pseudo pressure

If the total pressure change in the test period is small the product $c_t\mu$ may approximately be treated as a constant during the test. The differential equation for pseudo pressure is then our well known linear diffusivity equation.

$$\eta\nabla^2\psi = \frac{\partial}{\partial t}\psi \quad , \tag{10.11}$$

where the diffusivity, $\eta = \frac{k}{\phi c_t \mu}$, is a constant evaluated at the pressure at the start of the test.

Diffusivity is a constant evaluated at conditions at the start of the test.

The notion of a constant rate boundary condition is different when pseudo pressure replace pressure in the analysis. We will show that well tests should be analyzed in terms of (constant) mass rates when pseudo pressure is used, in contrast to reservoir volume rates when pressure is used. Note that a constant mass rate, Q_m, corresponds to a constant surface volume rate, Q_s, as $Q_m = Q_s\rho_s$, while a constant

[1] The boundary conditions are discussed on page 20 and 27

reservoir rate corresponds to a variable surface rate as $Q_s = \frac{\rho(p)}{\rho_s}Q$. The variable volume rate which should be used for determining the inner boundary condition for $\nabla\psi$ via Darcys law[1] is

$$Q(p) = \frac{Q_m}{\rho(p)} = \frac{\rho_s}{\rho(p)}Q_s \quad . \tag{10.12}$$

By rearranging the first equation in Eq. (10.4) we see that

$$\frac{k}{\mu_i}\nabla\psi = \frac{\rho}{\rho_i}\frac{k}{\mu}\nabla p \quad , \tag{10.13}$$

and Eq. (10.12) and (10.13) may be combined to give the boundary condition at the sand face ($r = r_w$). The result is

$$\frac{k}{\mu_i}\nabla\psi = \frac{Q_i}{2\pi r_w h} \quad , \tag{10.14}$$

where

$$Q_i = \frac{\rho(p)Q(p)}{\rho_i} = \frac{Q_m}{\rho_i} = \frac{\rho_s}{\rho_i}Q_s = B_{gi}Q_s \quad . \tag{10.15}$$

We see from Eq. (10.2), (10.11), and (10.14) that a well test in a gas reservoir can be analyzed using the same methods as for oil wells by replacing pressure with pseudo pressure, and using the values at initial reservoir pressure for viscosity and gas reservoir volume factor. The diffusivity is, on the other hand, evaluated at the pressure at the start of the test, which may be different from the initial pressure.

Oil well test are analyzed using reservoir volume rates. Gas well test are analyzed using mass rates.

10.2.1 Two-rate drawdown–buildup sequences

Flow rates in gas wells are often so large that non-Darcy (turbulent) pressure drops must be accounted for. The measured skin, S', is then

$$S' = S + DQ_s \quad , \tag{10.16}$$

where S is the normal skin factor, while DQ_s is a rate-dependent skin term with D a coefficient for the rate Q_s. In order to determine the two skin components, a multi-rate test is needed. An example of a multi-rate test is two drawdown–buildup sequences with different rates as illustrated in Fig. 10.2. If the first buildup is long enough for the pressure to recover to the initial value p_{wi}, that is

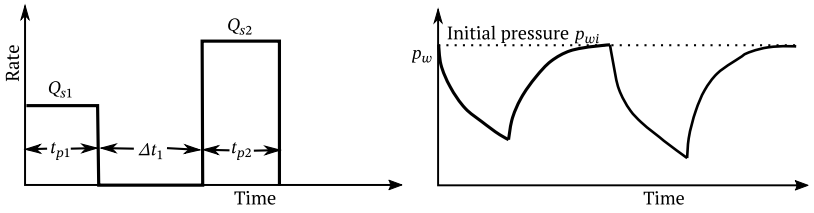


Figure 10.2: Two rate test with independent drawdown–buildup sequences.

$$\Delta t_1 > t_{p1} \quad , \tag{10.17}$$

we have two build-ups that can be analyzed independently using the Horner plot (page 40). The Horner analysis give two independent permeability estimates and two skin estimates

$$S'_1 = S + DQ_{s1} \quad \text{and} \quad S'_2 = S + DQ_{s2} \quad . \tag{10.18}$$

Given these two skin estimates the two components of the skin are

$$S = \frac{S_1' Q_{s2} - S_2' Q_{s1}}{Q_{s2} - Q_{s1}}$$
$$D = \frac{S_2' - S_1'}{Q_{s2} - Q_{s1}} \quad . \tag{10.19}$$

10.2.2 Step rate test

In gas wells the mobility ratio of gas and drilling-mud is highly unfavorable. As a result, gas have a tendency to finger through the mud filtrate (see Fig. 10.3), and well clean up by production may take a long time. The resulting time dependent skin may invalidate well test results, in particular skin estimates. A multi-rate test with more than two rates provides data redundancy which can be used for detecting insufficient clean up and improve data quality.

A step rate test is a test where the rate is increased in steps, as shown in Fig. 10.4, and at least three steps are needed in order to get the necessary redundancy in the skin estimates. Below we will derive a method for analyzing the four flow periods in a three-rate step rate test. The method involves plots that are similar to Horner plots (see page 40), and the derivation is based on superposition. The Horner plot is actually a special case of these variable rate plots, and the method can easily be generalized to any number of rate steps.

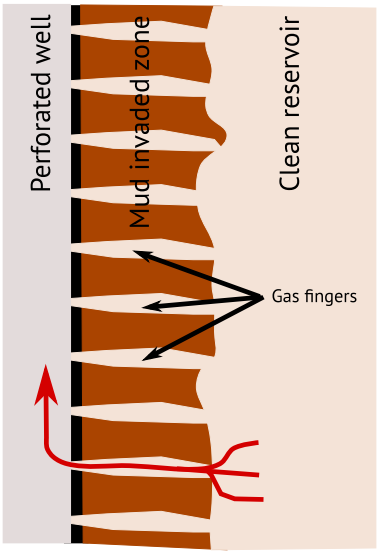


Figure 10.3: Fingering of gas during well clean up.

Variable rate plots are similar to Horner plots.

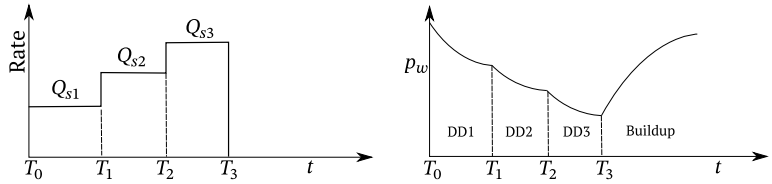


Figure 10.4: Step rate test with 3 drawdown periods, DD1, DD2 and DD3, and a final build-up.

The expected infinite acting pressure for each of the four test periods is found by superposition, that is the variable rates in the well is replaced by superposition of four constant-rate pseudo-wells starting at different times. The first pseudo-well has a contribution (Eq. (3.29)):

$$\psi(p_i) - \psi(p)_1 = \frac{Q_{s1}}{Q_{s3}} m \left(\ln\left(\frac{t}{t_0}\right) + a + 2S' \right) \quad , \tag{10.20}$$

where

$$m = \frac{Q_{s3} B_{gi} \mu_i}{4\pi k h} \quad , \tag{10.21}$$

$$a = \ln\left(\frac{4k}{\phi c_t \mu r_w^2} t_0\right) - \gamma \quad , \tag{10.22}$$

and t_0 is an arbitrary time unit conventionally set to $1h = 3600s$. Note that, as discussed on page 109, all rates are surface rates, and the product $c_t\mu$ in Eq. (10.22) is evaluated at the start of the test, while the product $B_{gi}\mu_i$ in Eq. (10.21) is evaluated at initial reservoir pressure. The contribution for the other pseudo-wells are

$$\psi(p_i) - \psi(p)_n = \frac{Q_{sn} - Q_{s\,n-1}}{Q_{s3}} m \left(\ln\left(\frac{t - T_n}{t_0}\right) + a + 2S' \right) \quad . \tag{10.23}$$

We will get the best permeability estimate from the final buildup period. By adding all the contributions to the well pressure (Eq. (10.20) and (10.23)) we get

$$\psi(p_i) - \psi(p) = m f_4(t) \quad , \tag{10.24}$$

where

$$f_4(t) = \frac{Q_{s1}}{Q_{s3}} \ln\left(\frac{t}{t-T_1}\right) + \frac{Q_{s2}}{Q_{s3}} \ln\left(\frac{t-T_1}{t-T_2}\right) + \ln\left(\frac{t-T_2}{t-T_3}\right) \quad . \tag{10.25}$$

We see from Eq. (10.24), that if we plot the pseudo pressure as a function of the log-time like variable $f_4(t)$, we get a straight line with slope m, as shown in Fig. 10.5. Note the similarity with the Horner plot.

The permeability is estimated from the slope m (Eq. (10.21)):

$$k = \frac{Q_{s3} B_{gi} \mu_i}{4\pi h} \frac{1}{m} \quad . \tag{10.26}$$

We see from Eq. (10.25) that $f_4(\infty) = 0$, so $f_4 = 0$ corresponds to infinite time. Thus, just as for the Horner plot, the average reservoir pressure can be found based on the extrapolated pressure, ψ^*, using the MBH-correction as explained on page 60. For a gas reservoir, reservoir volume may also be estimated based on the corresponding depletion, and known total production, using mass balance.

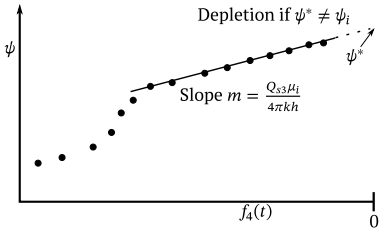


Figure 10.5: Variable rate buildup plot is used for permeability estimate. The horizontal axis is a transformed time given by Eq. (10.25).

By adding all the active contributions to the well pressure we get the following expression for the nth drawdown period

$$\frac{Q_{s3}}{Q_{sn}} (\psi(p_i) - \psi(p)) = m\,(f_n(t) + a + 2S) \quad , \tag{10.27}$$

with

$$\begin{aligned} f_1(t) &= \ln\left(\frac{t}{t_0}\right) \\ f_2(t) &= \frac{Q_{s1}}{Q_{s2}} \ln\left(\frac{t}{t-T_1}\right) + \ln\left(\frac{t-T_1}{t_0}\right) \\ f_3(t) &= \frac{Q_{s1}}{Q_{s3}} \ln\left(\frac{t}{t-T_1}\right) + \frac{Q_{s2}}{Q_{s3}} \ln\left(\frac{t-T_1}{t-T_2}\right) + \ln\left(\frac{t-T_2}{t_0}\right) \end{aligned} \quad . \tag{10.28}$$

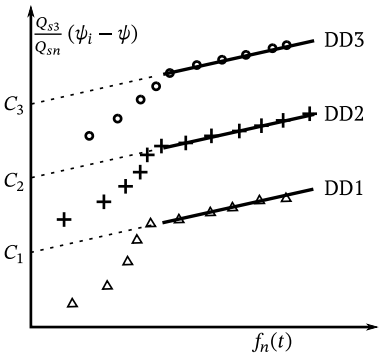


Figure 10.6: Step rate semilog plot for estimating rate dependent skin. All drawdown periods (DD1, DD2, and DD3, see Fig. 10.4) are fitted to straight lines with a common slope. The horizontal axis is a transformed time given by Eq. (10.28)

Each of the three drawdown periods will give estimates for total effective skin $S'_n = S + DQ_{sn}$. We see from Eq. (10.27) that the scaled pseudo-pressures, $\frac{Q_{s3}}{Q_{sn}}(\psi(p_i) - \psi(p))$, should be straight lines with the same slope, m, when plotted as a function of $f_n(t)$. The slope is known from analyzing the buildup, thus each line should be fitted with one parameter (the intercept) while forcing the slope. All periods are typically plotted on the same plot, as shown in Fig. 10.6, and if the actual slope on early periods is not m it indicates insufficient clean-up, or other problems.

The effective skins, $S'_n = S + DQ_{sn}$, are estimated from the intercepts, C_n (Eqs. (10.27) and (10.22)):

$$S'_n = \frac{C_n}{2m} - \ln\left(\frac{4kt_0}{\phi c_t \mu r_w^2}\right) + \gamma \quad . \tag{10.29}$$

The effective skin is a linear function of rate (Eq. (10.16)), so if we plot the effective skin as a function of rate as in Fig. 10.7, and fit to a straight line, the intercept is S and the slope is D. Again, if the first period(s) are not on a line it is an indication of insufficient clean-up, or other problems.

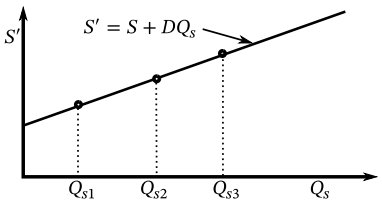


Figure 10.7: Skin vs. rate plot for estimating the components of rate dependent skin

10.3 Pseudo time

In the analysis with pseudo pressure above (see 109), we assumed that the pressure change during the test period was so small that $c_t\mu$ could be treated as a constant. If the maximum pressure change in the test period is to large, then the product $c_t\mu$ cannot be treated as a constant. In particular, this could be a problem for extended tests in tight reservoirs.

In the case when $c_t\mu$ cannot be treated as a constant, the differential equation for pseudo pressure can approximately be expressed as

$$k\nabla^2\psi = \phi c_{ti}\mu_i \frac{\partial}{\partial t_a}\psi \quad , \tag{10.30}$$

when time is replaced by pseudo time, t_a, which is defined as

$$t_a = \mu_i c_{ti} \int_{t_0}^{t} \frac{1}{\mu(t')c_t(t')}\, dt' \quad . \tag{10.31}$$

The pseudo time function, $t_a(t)$, is a function of pressure history.

The linear equation for pseudo pressure using pseudo time (10.30) is simply derived by inserting Eq. (10.31) into Eq. (10.3). The equation is at best only approximately correct since t_a is a function of pressure history, and thus different at different points in space, while the spatial derivative on the left hand side in Eq. (10.30) is evaluated at constant time. Fortunately, numerical experiments show that the approximation may be accurate for well testing purposes.

The pseudo time is a monotonous function of time, but it is a function of pressure history, and thus not a pure fluid property. Unlike pseudo pressure, the pseudo time function is different for each well test, and since $t_a(t)$ is space dependent, the question of which pressure history should be used arise. In addition, the formulation does not honor material balance. A full numerical simulation should always be performed in order to quality check results obtained using the pseudo time formulation, and matching the measurements with simulation may be more appropriate in cases with significant pressure changes. Estimates based on pseudo time will in any case serve as good starting values for the final matching process.

11
Multiphase flow

In reservoirs with pressure support from an aquifer or gas cap, and when well testing is used for reservoir monitoring of water or gas flooded reservoirs, the understanding of multiphase flow effects will be important for the interpretation of well tests. In this chapter we will, however, not investigate these situations. Here we will discuss the testing of wells where a two-phase region develops in the near well region. This situation will usually occur in gas condensate reservoirs and in oil reservoirs at or near the bubble point. We will also not investigate well testing in situations were, during the test or as a result of prior production, the reservoir is depleted such that a two-phase situation develops in the whole reservoir.

The phase diagram of the reservoir fluid in a gas condensate reservoir is shown in Fig. 11.1. A two phase region will develop close to the

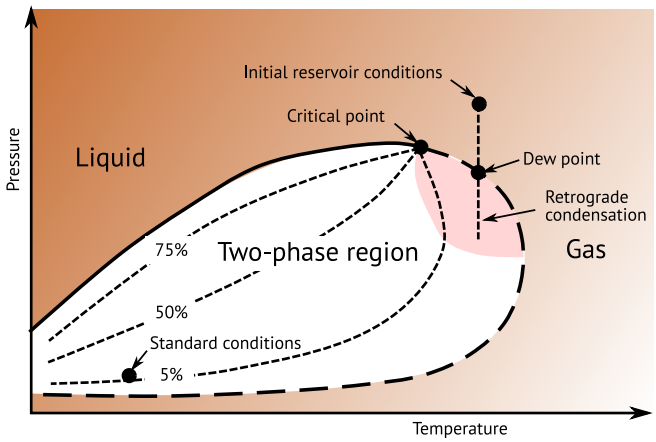


Figure 11.1: Phase diagram of gas-condensate reservoir fluid. At initial pressure the fluid is in a supercritical single phase. The two phase region is entered and liquid drops out when the pressure is reduced to the dew point pressure.

well when well pressure falls below the dew point pressure. Since flow depend on relative permeability, the two phase region has reduced total mobility, which introduce an extra contribution to skin. However, the two phase region is also highly dynamic; it grows in size, saturations are changing, and the composition of gas and liquid will change while producing. Relative permeability in the two phase region will change due to the dynamic saturation, and in a condensate reservoir relative permeability may also depend on composition which is also changing. The pressure and saturation profile around a well in a gas condensate reservoir is illustrated in Fig. 11.2.

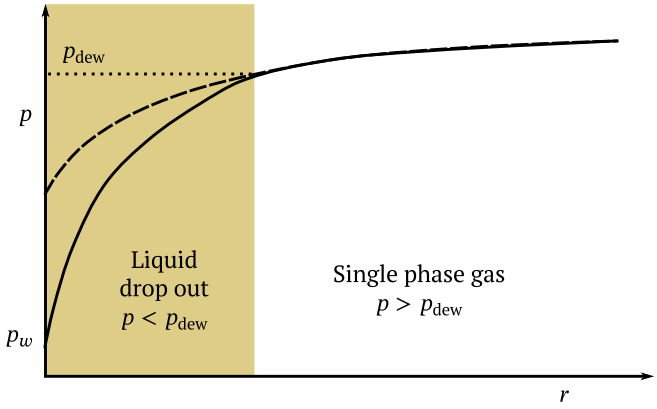


Figure 11.2: Pressure profile around a well below dew point pressure. In the liquid drop out (two phase) zone there is a larger pressure drop than in a corresponding single phase zone (dashed line).

The phase diagram of the reservoir fluid in an oil reservoir is shown in Fig. 11.3. A two phase region will develop close to the well when

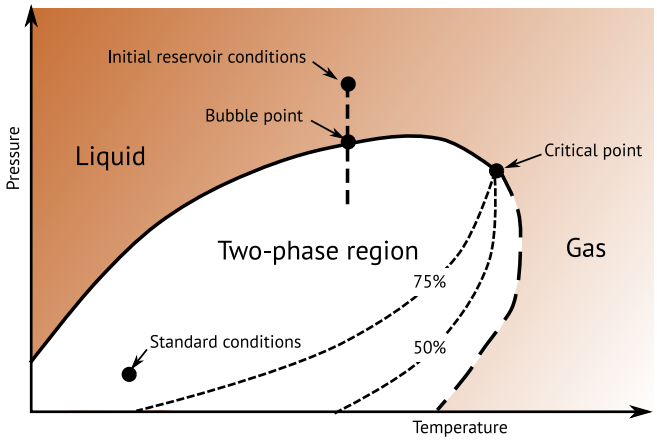


Figure 11.3: Phase diagram of oil reservoir fluid. At initial pressure the fluid is one phase liquid. The two phase region is entered and gas appears when the pressure it reduced to the bubble point pressure.

well pressure falls below the bubble point pressure. The two phase region is also in this case dynamic, and additionally mobile gas outside the immediate near well region may segregate. The composition of the produced fluids (surface gas oil ratio, and R_s of the reservoir liquid) will consequently not be constant during the test.

Due to the complications mentioned above, results based on well test analysis should always be checked with a “full-physics” simulation (see page 123). These simulations must allow for possible gravity segregation for oil and compositional changes for condensate.

11.1 Radial composite

Build-up tests and multi rate tests can often be analyzed in terms of the simple radial composite model. As shown in Fig. 11.4, the radial composite model has an inner region near the well with altered properties, representing the two-phase region, and an outer region with the original single-phase properties.

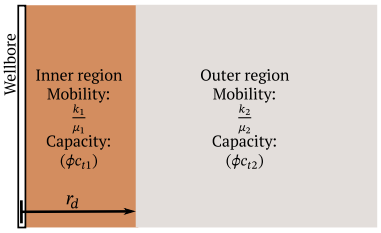


Figure 11.4: Radial composite model

The fundamental response of a radial composite is shown Fig. 11.5. At early times the pressure front will travel through the inner region,

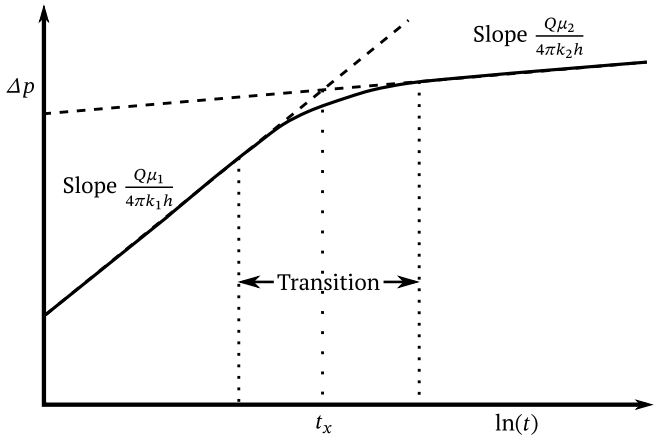


Figure 11.5: sketch of the fundamental response of a radial composite model with mobility ratio $M = \frac{k_2}{\mu_2}\frac{\mu_1}{k_1} > 1$.

and on the pressure vs. $\ln(t)$ plot we will see a straight line with a slope that reflects the inner region properties. At late times the front travels in the outer region, and we will see a straight line with a reduced slope reflecting the properties of the outer region. The corresponding log-log derivative plot for the fundamental response is shown in Fig. 11.6.

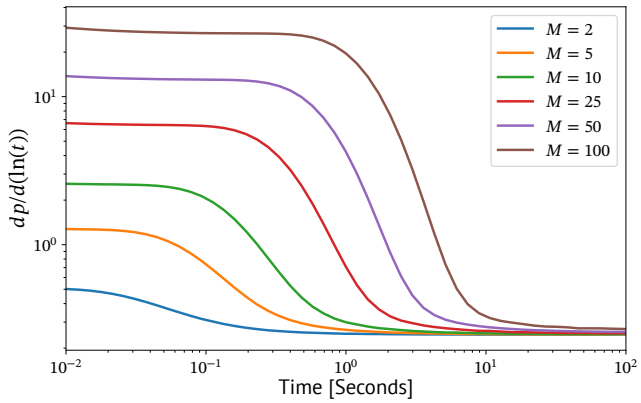


Figure 11.6: Log-log derivative plot of the fundamental response of a radial composite model.

Drawdown does not behave as a radial composite.

The initial drawdown period in any drawdown test has a highly dynamic inner zone and does not behave as a radial composite. Due to the changing composition, it is also difficult to maintain a constant rate. On the other hand, we will see below that buildup and well designed step-rate tests may see radial composite at the pressure front. Other tests may also show behavior that are reminiscent of radial composite, but the model can not be used for quantitative analysis.

Pressure profiles during a build up test are illustrated in Fig. 11.7. We will assume that the production period, t_p, is of sufficient length so that a near steady state profile has developed in the near well region, and that the changes in the pressure profile during the test is dominated by the shut-in (that is by the negative rate well in the superposition picture). Since the pressure front travels through the inner two-phase region at early times, the early-time step response reflects the properties of the two-phase region. Similarly, since the pressure

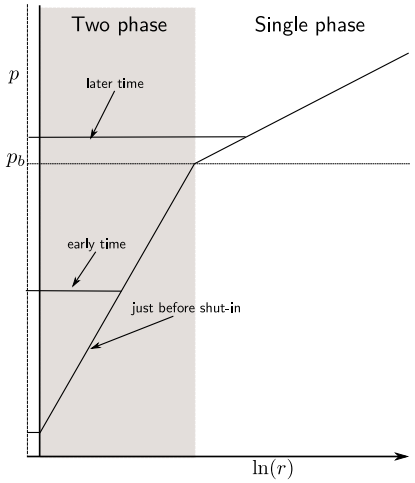


Figure 11.7: Pressure profiles during buildup. Note that the pressure front travels through the two-phase region as long as well pressure is below bubble-point pressure, and through the single phase region at later times.

front travels through the outer single-phase region at later times, the late-time response reflects the single phase properties. The fact that the two phase-region disappears when well pressure rise above bubble point pressure will represent a reduced skin at this point, but this is irrelevant since the rate is zero.

Analysis of the early part of the build-up test will give estimates for the effective mobility in the two phase region, the time of the transition can be used to estimate the size of the two-phase region, and the late part yield estimates for formation permeability and effective skin. The reduced mobility in the near well two-phase region contribute to an increased skin, so the measured effective skin has three contributions: The altered permeability in the near wellbore region (normal skin), reduced mobility in the near well two-phase region, and, in gas condensate reservoirs, an extra pressure drop due to high-rate turbulent flow close to the well. The last contribution is rate dependent, and the second is dynamic, so any detailed analysis of skin require a multi rate test.

Effective skin include reduced mobility in the near well two-phase region.

An example of a step rate test is shown in Fig. 11.8, and this test has been discussed for gas reservoirs on page 111. We will analyze the response to a rate change, and again assume that the previous production period is of sufficient length so that a steady state pressure profile has been developed in the near well region. The development of the pressure profile is illustrated in Fig. 11.9. Initially the front travels in the two-phase region, and the response will reflect the properties of this region, and the late-time response reflects single phase with effective skin. Note that, since the rates in this case is not zero, the change in two-phase region properties and size due to the pressure changes represent a non-constant effective skin that will influence the pressure response. The response is thus not completely that of a radial composite. However, the dynamic skin effect will be of the order $\left(\frac{\Delta t}{t_p}\right)^2$, and the rate schedule may be designed to minimize its influence.

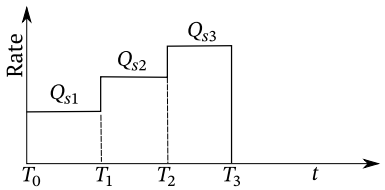


Figure 11.8: Example of a step rate schedule.

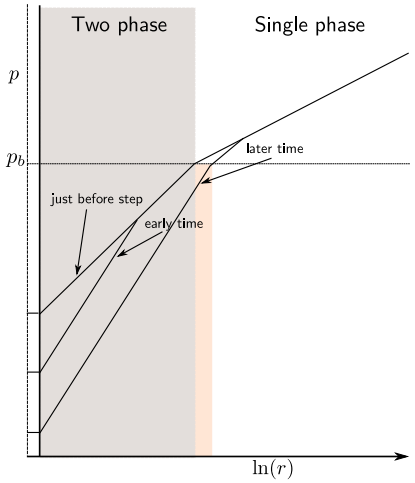


Figure 11.9: Pressure profiles during step rate test. Initially the pressure front travels through the two-phase region. The front travel through the single phase region at later times. Relative change in two-phase zone is small during the test provided that the initial production time is sufficiently long.

11.1.1 Well tests in water injectors

Water injectors may be tested in order to investigate how the injected water displace oil. The composite radial model can in many cases be used in order to understand and analyze these tests, as can be seen from the mobility distribution shown in Fig. 11.10.

Ideally the near well region will comprise three regions with different total mobility: In the outer unflooded region the mobility will be that of oil at initial water saturation, and since the flooding is of Buckley-Leverett type[1] there will be a sharp front with a step change in water saturation. Behind this front we have a two-phase region with reduced mobility. Since typically the injected water is much colder than the reservoir the volume close to the well will be cooled, and as cold fluids have higher viscosity than hot fluids the total mobility is reduced in the near well region. Typically the viscosity is increased by a factor ≈ 4 for both oil and water at North-sea conditions. In ideal one-dimensional or radial displacement the temperature distribution will be a sharp front which typically travels with a speed $\approx 1/3$ of the saturation front. The temperature is constant (at injection temperature) behind the front. Due to heat flow to the rock above and below the reservoir zone the real temperature front will however typically be zone with gradual temperature change.

We have seen that the region around a water injector can be described in terms of three zones with different mobility, and ideally the mobility in each zone is approximately constant, so that a well test may be analyzed in terms of a radial composite model. The saturation behind the saturation front is however not exactly constant, even for ideal Bucley-Leverett displacement (see Fig. 11.10), and in real cases there will be some dispersion in the front location due to reservoir heterogeneities. Since the temperature front is also typically a zone with gradual temperature change, the radial composite analysis should not be expected to give very accurate results, but it can serve as a good starting point for more detailed analysis.

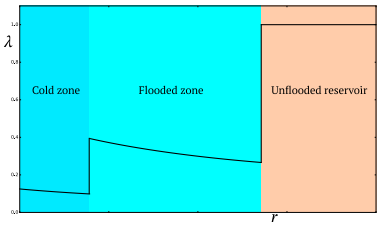


Figure 11.10: Sketch of the ideal relative mobility in the region around a water injector.

[1] For a discussion of Buckley-Leverett displacement, see for instance L.P. Dake. *Fundamentals of Reservoir Engineering*. Developments in Petroleum Science 8. Elsevier, 1978, page 356–362, where the theory is developed for 1-dimensional linear flow. The radial displacement near a water injector is described by the same equations where the distance x is replaced by r^2.

11.2 Pseudo pressure and pseudo time

Well tests in gas reservoirs can in many cases be analyzed using the methods developed for oil reservoirs provided the analysis is performed in terms of pseudo-pressure (see page 107). We will now show that the concept of pseudo-pressure, in the form of the so called steady-state pseudo pressure, is approximately valid for both single and two-phase flow.

Before any major approximations have been made, the general equation for the pressure in the single phase case is Eq. (10.1), which, in the two-phase situation, may be generalized to

$$\nabla \cdot \left(\left(\frac{k_{rg}\rho_g}{\mu_g} + \frac{k_{ro}\rho_o}{\mu_o} \right) \nabla p \right) = \frac{\phi}{k} c_t(p) \rho(p) \frac{\partial}{\partial t} p \quad , \tag{11.1}$$

where

$$\begin{aligned} c_t &= \frac{1}{\phi}\frac{d\phi}{dp} + \frac{1}{\rho}\frac{d\rho}{dp} \\ \rho &= S_o\rho_o + S_g\rho_g \end{aligned} \quad . \tag{11.2}$$

Eq. (11.1) is just an expression for the conservation of total mass.

Pseudo pressure is defined provided that total composition is constant.

If we assume that the total composition is constant, we may uniquely define the following pseudo pressure

$$\psi(p) = \frac{\mu_i}{\rho_i} \int_{p_0}^{p} \left(\frac{k_{rg}\rho_g}{\mu_g} + \frac{k_{ro}\rho_o}{\mu_o} \right) dp' \quad , \tag{11.3}$$

since density, saturation, and viscosity in that case is a function of pressure only. The relative permeabilities are also functions of pressure through the pressure dependent saturations. In practice we will use an equation of state to define the pressure dependency of saturations and densities, and the pressure dependency of viscosity is determined by a tuned viscosity correlation.

The diffusivity equation for the pseudo pressure defined in Eq. (11.3) is

$$\nabla^2 \psi = \frac{\phi \mu_t(p) c_t(p)}{k} \frac{\partial}{\partial t} \psi \quad , \tag{11.4}$$

where

$$\mu_t = \rho \left(\frac{\rho_o k_{ro}}{\mu_o} + \frac{\rho_g k_{rg}}{\mu_g} \right)^{-1} \tag{11.5}$$

is the effective viscosity. This can be verified by substituting the definition of the pseudo pressure (11.3) into Eq. (11.4).

The concept of pseudo pressure in a two-phase system assumes constant composition in both time and space. This implies a constant surface GOR, and a steady state profile where the saturation is a function of distance from the well while the total composition is constant. Both of these conditions are at best only approximately valid. The right hand side of Eq. (11.4) is also, just as in the single-phase gas case, a function of pressure, and we need to assume that the product $\mu_t(p)c_t(p)$ changes little during the test so that it may be treated as a constant.

Pseudo pressure, effective viscosity, and total compressibility should be evaluated using the composition of the production stream

at the start of the analyzed period. As a consequence, in contrast to the single phase case, the steady state pseudo pressure is process dependent. Note also that $\psi(p)$ depend on relative permeability, which, in particular for gas condensate, is difficult to measure with high accuracy. Relative permeability may also depend on rate, which translate into a variation with distance from the well. All these concerns calls for caution when applying pseudo pressure. However, it has been shown that the analysis of two-phase buildup tests can often be made to sufficient accuracy using pseudo-pressure and replacing $\mu_t(p)c_t(p)$ with a constant.[2]

Two phase pseudo pressure is process dependent.

If the maximum pressure change in the test period is not small then the product $\mu_t(p)c_t(p)$ cannot be treated as a constant. In these cases we may also introduce pseudo time (see page 113). The two phase pseudo-time t_a is defined as

$$t_a = \mu_i c_{ti} \int_{t_0}^{t} \frac{1}{\mu_t(t')c_t(t')}\, dt' \quad . \tag{11.6}$$

Like in gas well testing, pseudo time is an uncontrolled approximation.

For well tests producing below bubble- or dew-point pressure, results based on pseudo pressure and pseudo time, or any other approximate analytical theory, should always be quality checked using full physics numerical simulations.

[2] J.R. Jones and R. Raghavan. "Interpretation of Flowing Well Response in Gas-Condensate Wells." In: *SPE Formation Evaluation* (Sept. 1988), pp. 578–594. DOI: 10.2118/14204-PA.

12
Numerical methods

Analysis based on analytical solutions of simple models should always be the first pass in well test interpretation. However, analytical models have limited applicability in real world situations with complex well paths, non trivial geology, multiple interacting wells, and multi-phase flow. In this chapter we will discuss how a well test can be simulated, and the way such numerical simulations can be utilized in the analysis in order to obtain estimates for reservoir parameters.

In general numerical simulations are necessary in a number of contexts:

- In the context of unknown and complex geometry, direct simulations is used to test "what if" scenarios.

  Scenario testing.

- Given the scenario, that is a geological concept that can be described by a set of numerical parameters, simulation is combined with automatic or manual parameter estimation.

  Parameter estimation.

- Simulation on models with increased complexity and additional physics is used to validate results from parameter estimation based on simplified analytic or numerical models, or the model parameters from these simple models are used as starting points for parameter estimation using the more complex simulation model. Model validation is particularly important for multiphase flow.

  Model validation.

- The analysis of well tests on wells with complex paths.

  Complex well paths.

- Situations involving several wells, and in particular interference testing, can usually only be adequately analyzed using numerical simulations.

  Interference testing

- Finally, it should be mentioned that simulations are used to obtain type curves for complex geological concepts. Traditional type-curve matching can then be performed using these type curves, see page 102 for an example.

  Type curves.

12.1 Well tests simulators

Commercial software packages for well test interpretation typically include a well test simulator and a module for building suitable simulation grids. The complexity of the models that can be built, and the

ease of use may vary, but the first choice will be to use the provided simulator as it should be well integrated with the other visualization and interpretation tools. Conventional reservoir simulators can also be used for simulating well test. These simulators are the most complete with regards to reservoir flow-physics and phase behavior, but are not tuned to solving well-test problems. Thus, creation of suitable grids and providing correct boundary conditions can be challenging. On the other end of the scale we have production technology oriented "multi-physics" simulators, which can also be used to simulate well tests. These simulators are coupled well–near-well-reservoir simulators that give an accurate description of flow in the completions and wellbore, including details in the inflow to the well, but they typically have limited capabilities regarding the representation of reservoir geology, and additionally they tend to be very computationally inefficient.

Based on which differential equations that are solved, simulators may be divided into four classes: Simulators that solve the linear diffusivity equation, those that solve the non-linear diffusivity equation, black-oil simulators, and compositional simulators. A given simulator program may include more than one of these in the same package. The simulators may also be categorized according to the way the equations are discretized, either by finite elements or by control-volume finite difference methods.

Finite elements vs. finite difference.

The linear diffusivity equation,

Linear diffusivity equation.

$$\nabla \cdot (K \cdot \nabla \psi) - c_t \mu \frac{\partial}{\partial t} \psi = 0 \quad , \tag{12.1}$$

is the equation that all the analytical analysis methods are based on, and, with $\psi(p)$ being the pseudo pressure, it is universally applicable for single phase well tests as long as the total pressure change during the test is not too large. In Eq. (12.1), K is the space dependent permeability tensor, and the purpose of the well test is, in a general sense, to characterize the permeability field K, i.e. the reservoir. A numerical solution of Eq. (12.1) is needed whenever the reservoir has a complex shape or permeability distribution, or when the well path or completion pattern is non-trivial. Finite element discretisation is more suited than finite difference for complex geometries, as it is easier to create grids that follow general complex shapes, so simulators that solve the linear (and also non-linear) diffusivity equation are often finite element based.

In a finite element discretisation the solution is approximately expressed as a sum of basis functions, ϕ_n,

In finite element methods, the solution is expressed in terms of local basis functions, often called trial-functions.

$$\psi(t, x) = \sum_n a_n(t) \phi_n(x) \quad . \tag{12.2}$$

Each basis function is localized around a node in the grid as shown in Fig. 12.1, and different finite element methods differ in terms of the shape of the selected basis functions. If we insert Eq. (12.2) into Eq. (12.1), we get

$$\sum_n \phi_n \frac{d}{dt} a_n - \frac{1}{c_t \mu} \sum_n a_n \nabla \cdot (K \cdot \nabla \phi_n) = 0 \quad . \tag{12.3}$$

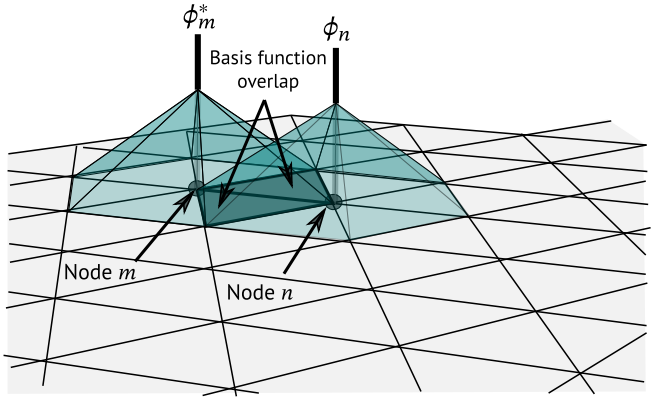


Figure 12.1: Example of basis functions (elements) for finite element discretization of a two-dimensional domain. Note that the simple pyramid shaped elements shown here may be to simple for accurate simulation, and higher order elements are used in actual simulators.

We now introduce a second set of basis functions, ϕ_n^*. Note that the the two sets are usually identical, but they need not be and sometimes lower order functions are used for this second set than for the first set. If we multiply Eq. (12.3) with each function in the second set and integrate over all space, we get the following system of equations expressed on matrix form

Projections onto a second set of local basis functions, the test functions, transform the partial differential equation into a system of ordinary differential equations.

$$A \cdot \frac{d}{dt} a - \frac{1}{c_t \mu} B^* \cdot a = 0 \quad , \tag{12.4}$$

where

$$A_{mn} = \int \phi_m^* \phi_n \, dV \quad , \tag{12.5}$$

and

$$B_{mn}^* = \int \phi_m^* \nabla \cdot (K \cdot \nabla \phi_n) \, dV \quad . \tag{12.6}$$

The above expression for the matrix B^* (Eq. (12.6)), contains derivatives of the permeability, and second derivatives of the basis functions. However, since the reservoir is modelled in terms of regions with different properties, and since the derivative of the basis functions are usually not continuous (see for instance Fig. 12.1), the integrand will contain δ-function type terms. We would prefer an expression that contain first derivatives only, and we will also see that as an additional bonus we will get an expression where flow boundary conditions can be implemented in a very natural manner.

We can apply the divergence theorem to transform a volume integral to a surface integral over the outer boundaries

$$\int \nabla \cdot (\phi_m^* \cdot K \cdot \nabla \phi_n) \, dV = \int \phi_m^* K \cdot \nabla \phi_n \cdot dS \quad . \tag{12.7}$$

We may also apply the chain rule for derivation:

$$\int \nabla \cdot (\phi_m^* \cdot K \cdot \nabla \phi_n) \, dV = \int \nabla \phi_m^* \cdot K \cdot \nabla \phi_n \, dV + \int \phi_m^* \nabla \cdot (K \cdot \nabla \phi_n) \, dV \quad . \tag{12.8}$$

Combining Eqs. (12.7) and (12.8) gives

$$\int \phi_m^* \nabla \cdot (K \cdot \nabla \phi_n) \, dV = - \int \nabla \phi_m^* \cdot K \cdot \nabla \phi_n \, dV + \int \phi_m^* K \cdot \nabla \phi_n \cdot dS \quad , \quad . \tag{12.9}$$

and substituting Eq. (12.9) for Eq. (12.6) in Eq. (12.4) gives

$$A \cdot \frac{d}{dt} a + \frac{1}{c_t \mu} B \cdot a = b \quad , \tag{12.10}$$

where

$$b_m = \frac{1}{c_t} \int \phi_m^* \frac{1}{\mu} K \cdot \nabla \sum_n a_n \phi_n \cdot dS = \frac{1}{c_t} \int \phi_m^* \, q \cdot dS \quad , \tag{12.11}$$

and

$$B_{mn} = - \int \nabla \phi_m^* \cdot K \cdot \nabla \phi_n \, dV \quad , \tag{12.12}$$

We have seen that by introducing two sets of localized basis functions, $\{\phi_n(x)\}$ and $\{\phi_n^*(x)\}$, the partial differential equation (12.1) is transformed into an system of ordinary differential equations for the coefficients $a_n(t)$ (Eq. (12.10)). The right hand side of this system of equations are determined by the flux across the boundaries. Flux boundary conditions, such as a given well rate, are thus straight forward to implement. Other boundary conditions, such as constant pressure, can of course also be implemented, but we will not go into any detail here.

The system of differential equations (12.10) is solved by time-stepping, that is the coefficient vector at time $t^{n+1} = t^n + \Delta t$ is calculated by solving a system of linear equations where the coefficients are calculated based on the vector at t^n. An implicit time stepping scheme has to be applied, and we will use the Crank–Nicholson scheme as an example. In that case the time-discretized Eq. (12.10) is

$$A \cdot \left(\frac{a(t^{n+1}) - a(t^n)}{\Delta t} \right) + \frac{1}{c_t \mu} B \cdot \left(\frac{a(t^{n+1}) + a(t^n)}{2} \right) = b(t^n) \quad , \tag{12.13}$$

The pressure change during a time step is calculated by solving a sparse linear system of equations.

which correspond to the following set of linear equations

$$\left(A + \frac{\Delta t}{2 c_t \mu} B \right) a(t^{n+1}) = \left(A - \frac{\Delta t}{2 c_t \mu} B \right) a(t^n) + b \, \Delta t \quad . \tag{12.14}$$

the matrix elements A_{mn} and B_{mn} are non-zero only where the functions ϕ_m^* and ϕ_n overlap

We see from Eqs. (12.5) and (12.12) that the matrix elements A_{mn} and B_{mn} are non-zero only if the functions ϕ_m^* and ϕ_n overlap, so since the basis functions are local, these matrices are sparse, and the number of non-zero elements is proportional to the number of grid nodes. The matrices are also independent of time, implying that they only need to be evaluated once for all time steps.

Flexible gridding to complex geometry and well paths is the major strength of the finite element discretisation.

The finite element method is extremely flexible in terms of grids. Note also that the reservoir properties (e.g., K) is not expressed in terms of the basis functions, so they can have an independent grid representation, adding an additional level of flexibility.

If the maximum pressure change in the test period is too large then the product $c_t \mu$ cannot be treated as a constant. This is especially acute for extended tests in gas reservoirs. Introducing pseudo time can provide some insight, but analysis that employ full numerical simulation should be considered as mandatory (see page 113). It is clearly necessary to perform the simulations using pseudo pressure. The diffusivity equation,

$$\nabla \cdot (K \cdot \nabla \psi) - c_t(p)\mu(p)\frac{\partial}{\partial t}\psi = 0 \quad , \tag{12.15}$$

Non-linear diffusivity equation

is now non-linear. However, if the $c_t(p)\mu(p)$-product does not change much over short time periods, it can be treated explicitly in time stepping. Since the pseudo-pressure analysis works for short tests, explicit time stepping is a good approximation in many cases. Note that the pressure should be solved using some level of implicit time stepping, this is uncoupled to the treatment of the $c_t\mu$ product.[1] If we in addition assume that the $c_t\mu$ product varies little over each overlap area, then it can be treated as a constant in the integration, and Eq. (12.14) becomes

[1] This is reminiscent of the IMPES (Implicit pressure Explicit saturation) type of formulations much used in reservoir simulation.

$$\left(A + \frac{\Delta t}{2}B'\right)a(t^{n+1}) = \left(A - \frac{\Delta t}{2}B'\right)a(t^n) + b\,\Delta t \quad . \tag{12.16}$$

where

$$B'_{mn}(p) = \beta_{mn}B_{mn} \quad \text{and} \quad \beta_{mn} = \frac{1}{c_t(p, x_{mn})\,\mu(p, x_{mn})} \quad . \tag{12.17}$$

We see that a finite element simulation is just marginally more computationally demanding in the case of a pressure dependent $c_t\mu$ product compared to the linear case, provided that pseudo-pressure is used and we have an efficient way of calculating $c_t(p)$ and $\mu(p)$.

In situations with dynamic two-phase flow, such as production below the bubble- or dew-point pressure in oil or condensate reservoirs, simulations based on the diffusivity equation are not sufficient. Formulations that take changes in saturation or composition into account, implemented in "full physics" simulators, are needed. These simulators are either black-oil, which is sufficient for oil reservoirs, or compositional, which are usually needed in condensate reservoirs.

Full physics simulators

Full physics simulators invariably employ finite difference control volume discretisation, which is the class of discretisation used by all major commercial reservoir simulators. In this formulation space is divided into grid blocks (control volumes), and a mass balance equation is written for each of these. Each grid block is assumed to be in thermodynamic equilibrium so that the properties are spatially constant, and the saturation and composition of each phase is a function of total composition and pressure through an equation of state. Reservoir properties are also discretized using the same grid, with a single value of permeability and porosity for each block. The flux of each phase between grid blocks are normally determined by the pressure difference between the blocks and by the saturation (relative permeability) in the upstream block. This is called the two-point flux approximation with upstream weighting. Multi-point flux approximations, where the flux between two grid blocks depends on the pressure in additional neighboring blocks, are sometimes also implemented. These multi-point flux approximations reduce the grid-orientation effect, which in particular cases can severely damage the accuracy of multi-phase simulations, but are nevertheless in little use and not all simulators implement them.

Finite difference control volume discretisation

The grid consist of grid blocks, and all reservoir properties, both static and dynamic live on the same grid.

The finite difference discretisation is much more restricted with respect to gridding than the finite element methods. In particular, grid blocks need to be orthogonal, that is that grid block faces must be orthogonal to the line connecting grid centers. This is illustrated in Fig. 12.2. Often simple shoe-box shaped grid-blocks are used, but in general these orthogonal grids are called PEBI-grids or Voronoi-grids. In spite of the limitations on gridding imposed by the finite difference discretisation, tools delivered with specialist well-test simulators are in many cases able to create good orthogonal grids as illustrated in Fig. 12.3.

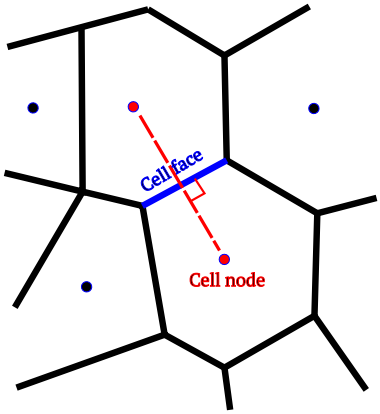


Figure 12.2: Example illustrating orthogonality of grid blocks.

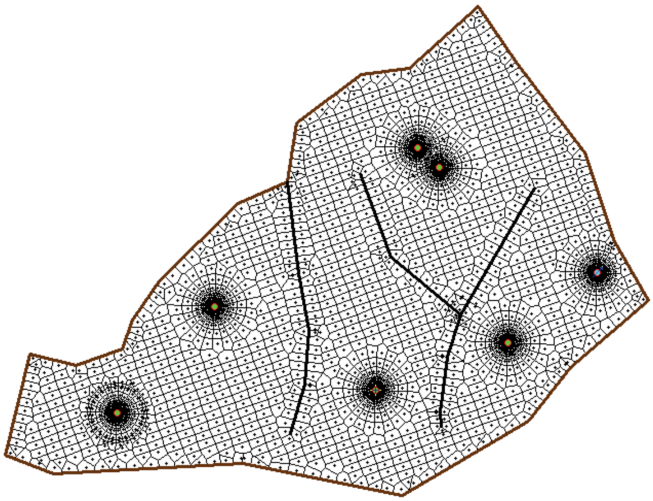


Figure 12.3: Example of a finite difference PEBI-grid with refinements around wells.

Some vendors supply a unified simulation framework where finite difference discretisation is used throughout, even for problems where the linear diffusivity equation is applicable.

12.1.1 Laplace finite element, and the Stehfest algorithm

As an alternative to time stepping, the linear diffusivity equation can be solved in Laplace space:

$$\nabla \cdot \left(K \cdot \nabla \widetilde{\psi}(s,x)\right) - c_t \mu \, s \widetilde{\psi}(s,x) = 0 \quad . \tag{12.18}$$

If we discretize by finite elements in space, we get the Laplace space analogue of Eq. (12.10):

$$\left(sA + \frac{1}{c_t \mu} B\right) \cdot a(s) = b(s) \quad . \tag{12.19}$$

This sparse linear system must be solved to get the solution for a given s. If we were to numerically invert $\widetilde{\psi}(s,x)$ by numerically evaluating an integral for each needed t, then this method would have been forbiddingly numerically demanding. Luckily, Laplace transforms of monotonously decaying functions (especially functions with exponential decay) can be accurately inverted for a given t based on transformed function values at a small number of s by the Stehfest algorithm. In well testing the fundamental solutions have the desired properties, and the Stehfest algorithm have extensively been applied

The inverse Laplace transform is calculated using the Stehfest algorithm.

to well test problems were the Laplace transform is known on closed form, but no explicit inverse transform has been found. The Laplace finite element in conjunction with the Stehfest algorithm can thus be an attractive option, at least for obtaining fundamental solutions in complex geometries and geologies. More complex well test responses can then be found by superposition of fundamental solutions.

A number of algorithms for numerical inversion of the Laplace transform do exist, but no single algorithm is suitable for all problems. In the Laplace finite element method, the calculation of $\psi(s)$ require solving a large system of linear equations, implying that any inversion method that require a large number of $\psi(s)$ values to be evaluated will be highly inefficient. Additionally values for $\psi(s)$ are only available for real s. Numerical inversion of the Laplace transform is thus a hard problem, and it is especially difficult if we are seeking algorithms where only a small number of values for real s suffice to calculate a reasonable inverse for a given t. A family of algorithms for this type of problems are based on the so called Gaver functionals,[2] and among these it is the Stehfest algorithm[3] that is commonly used in the well-testing context. We will not even attempt to derive the Stehfest algorithm here, but the result is that the solution at a given t is found as a linear combination of the Laplace solution at a series of specific s:

$$\psi(t) \approx \frac{\ln(2)}{t} \sum_{n=1}^{2N} \omega_n(N) \cdot \widetilde{\psi}\left(\frac{n\ln(2)}{t}\right) \quad , \tag{12.20}$$

where[4]

$$\omega_n(N) = (-1)^{N+n} \sum_{i=\lfloor((n+1)/2\rfloor}^{\min(n,N)} \frac{i^{N+1}}{N!} \binom{N}{i} \binom{2i}{i} \binom{i}{n-i} \quad . \tag{12.21}$$

The series in Eq. (12.20) converges to the exact solution with an increasing number of terms. The convergence can, however, be very slow. Additionally, the coefficients ω_n have alternating sign, so that extended precision arithmetic is necessary in the calculation if more than a few terms are needed. Using standard double precision arithmetic the maximum number of terms is 7. Extended precision arithmetic, which is implemented in software, is computationally much more demanding than double precision, which is implemented in the CPU hardware. However, it is easy to implement in the Stehfest algorithm itself, and for situations where the Laplace solution is explicitly known the inversion should always be performed using extended precision. In Laplace finite element the Laplace solution is only available at a precision given by the finite element code. This is typically at double precision, and implementing the finite element method using extended precision is not feasible. Fortunately, experience show that the maximum of 7 terms available for double precision is usually sufficient at least for the monotonous fundamental solutions found in the well testing context.

The main advantage of the Laplace finite element method is that the calculation cost is proportional to the number of time values we

[2] P.P. Valkó and J. Abate. "Comparison of Sequence Accelrators for the Gaver Method of Numerical Laplace Transform Inversion." In: *Computers and Mathematics with Applications* 48 (2004), pp. 629–636. DOI: 10.1016/j.camwa.2002.10.017.

[3] The names Gaver-Stehfest algorithm and Salzer summation is also used.

[4] $\lfloor x \rfloor$ is the largest integer less than or equal to x, and $\binom{m}{n}$ is the binomial coefficient.

are actually interested in. When the diffusivity equation is solved by traditional time stepping the calculation cost is proportional to the number of time steps. Since accuracy is determined by time step length, Δt, efficient automatic time step control is an issue, but the number of time steps taken is typically much larger than the ones that we actually need in order to perform the well test analysis. Also, in the initial transient period Δt must be very small, and if we are mainly interested in late time behavior we still have to time-step the solution all the way from $t = 0$.

12.2 Parameter estimation

The purpose of the well test, and the well test analysis is to characterize the reservoir. In practice this means to find numerical parameters related to conceptual models of the reservoir, i.e., parameters such as permeability, distance to faults, etc. Analysis based on analytical solutions of simple models should always be the first pass, but more often than not, the reservoir itself and our conceptual models are too complex to be accurately represented by the models where we have analytical solutions. In these cases, simulations using a well test simulator will be an integral part of the well test analysis. The simulator can be utilized in two different approaches. The first approach is to run a number of simulations to generate type curves for a specific scenario. The second approach is to include simulation runs in the inner loop of an automatic parameter matching, or optimization, procedure. The numeric model used in the well test analysis must correspond to a geological concept, and this concept should have as few parameters as possible. The parameters should be transferable to parameters used, either directly or for conditioning, in the full field geological model, but it is normally not recommended to use well test data directly in conditioning these models.

Type curve matching is attractive for models with few parameters.

Type curve matching is a proven method that historically has had a wide use in well test analysis, and the method is well supported in well test analysis software. Type curve matching is based on a model with a small number of parameters, and a set of curves, typically for pressure and pressure derivative, have been created for selected parameter settings. The curves are typically generated in terms of dimensionless time and pressure, and sometimes also in terms of other dimensionless groups, so that the actual measured time and pressure and must be scaled. This scaling may include some of the unknown parameters. The matching process simply involves comparing the scaled measured data with the type curves, adjusting the scaling, and finding the curve that is closest to the measured. An example of type curve matching was briefly discussed on page 102, with an example given in Fig. 9.12. Note that, just as for the analytic methods, the actual response can be divided into time periods, and different type curves used for the analysis of each time period. The matching process can be manual, and purely visual, or a numerical matching measure can be defined and the matching process can be assisted by

an optimization algorithm.

Well testing software typically come with a large set of type curves preloaded, and matching to these are well integrated in the software. In addition, type curves can also be found in the literature, but in many cases no curves exist that correspond to the geological concept at hand. In these cases it can be an option to use a well test simulator to generate type curve sets. This is particularly attractive if the concept is expected to be valid for a number of well tests, so that the curves can be reused. If the situation is unique, then direct parameter estimation with the simulator in the loop, as described below, will probably be more effective.

The principle behind automatic, or computer assisted, parameter matching with a well test simulator is simple: We have geological model with a set of parameters, $\{\lambda\}$, and this model is implemented in a numerical well test simulator. The simulator then run the model with different parameter values until the simulated response matches the measured well test response. Manual matching may be based on pure visual inspection of plots of the simulated results. In order to involve optimization algorithms in the matching process, then the mismatch, that is the difference between the simulated and the measured data, must be quantified. The measure is called a *mismatch function* or an *objective function,* and a typical form that is used is a weighted sum of squares:

The mismatch function is a measure for the difference between the simulated and the measured response.

$$\mathcal{O}(\{\lambda\}) = \sum_n w_n \left(M_n - S_n(\{\lambda\})\right)^2 \quad , \tag{12.22}$$

where $\mathcal{O}$ is the mismatch function, M_n is a measured quantity and S_n is the corresponding simulated value, and w_n is the weight that is put on the n-th measurement. When the objective function is defined, the parameter estimation is a minimization process, that is a question of finding the parameter set that minimize the objective.

Creating a good objective function, that is selecting which measured values to include and what weights to put on them, is highly non-trivial. It would seem that the definition is totally arbitrary and subjective, but if the objective function is defined in a Bayesian framework we have a language in which the question of what is a good objective function can be discussed.

Bayes theorem can be stated in mathematical terms as

$$P(A|B) = \frac{P(B|A)P(A)}{P(B)} \propto P(A)P(B|A) \quad , \tag{12.23}$$

where $P(A|B)$ is the conditional probability that A occur given that B has occurred. Thus Eq. (12.23) gives us a mean to obtain the posterior probability $P(A|B)$ from the prior probability $P(A)$, that is the conditional probability for the occurrence of A after the occurrence of B has been taken into account. Reformulating Bayes theorem to our setting gives

Bayes theorem: The updated probability of a parameter set after we have made measurements $p(\{\lambda\}|\{M\})$ is proportional to the product of the probability assigned to the set before the measurement $p(\{\lambda\})$ and the probability that a measurement will give the measured values given the parameter set $p(\{M\}|\{\lambda\})$.

$$p_{\text{posterior}}(\{\lambda\}|\{M\}) \propto p_{\text{prior}}(\{\lambda\})p(\{M\}|\{\lambda\}) \quad . \tag{12.24}$$

If we define an objective function such that

$$p(\{\lambda\}) \propto \exp\left(-\mathcal{O}(\{\lambda\})\right) \quad , \tag{12.25}$$

then Bayes theorem can written as

$$\mathcal{O}_{\text{posterior}}(\{\lambda\},\{M\}) = \mathcal{O}_{\text{prior}}(\{\lambda\}) + \mathcal{O}(\{M\},\{\lambda\}) \quad . \tag{12.26}$$

We see that if we define the objective function by Eq. (12.25), then an objective function of value zero gives a probability of $\exp(0) = 1$, while a large objective function gives a small probability. Thus, minimizing the objective function corresponds to finding the most probable parameter set.

Comparing Eqs. (12.22) and (12.26) we can identify the mismatch function

$$\mathcal{O}(\{M\},\{\lambda\}) = \sum_n w_n \left(M_n - S_n(\{\lambda\})\right)^2 \quad , \tag{12.27}$$

which gives

$$\mathcal{O}_{\text{posterior}}(\{\lambda\},\{M\}) = \mathcal{O}_{\text{prior}}(\{\lambda\}) + \sum_n w_n \left(M_n - S_n(\{\lambda\})\right)^2 \quad . \tag{12.28}$$

We seek the most probable posterior parameter set.

If we identify the best parameter set with the most probable posterior parameter set, we see from Eq. (12.28) that we need to minimize an objective function that contain two terms: a prior term and a mismatch function. The prior term represents prior knowledge of possible parameter values, and is often set to zero reflecting that we make no prior assumptions. Note that if the number of parameters is large, the minimization problem without a prior term is ill posed, and the prior term serves as a natural regularization. The mismatch term represents what in Bayesian statistics is called the measurement likelihood, that is the probability that a measurement will give the measured values given the parameter set.

The objective function is the sum of a prior term and a mismatch function.

If we use a Gaussian error model for uncorrelated measurements, the likelihood is

$$p(\{M\}|\{\lambda\}) \propto \exp\left(-\sum_n \frac{\left(M_n - S_n(\{\lambda\})\right)^2}{\sigma_{n,\text{model}}^2 + \sigma_{n,\text{meas}}^2}\right) \quad , \tag{12.29}$$

where $\sigma_{n,\text{meas}}$ is the measurement error and $\sigma_{n,\text{model}}$ is the model error. From Eq. (12.29), we see that the weights in Eq. (12.22) are

$$w_n = \frac{1}{\sigma_{n,\text{model}}^2 + \sigma_{n,\text{meas}}^2} \quad . \tag{12.30}$$

The weights in the mismatch function are given by the model and measurement errors.

By introducing the Bayesian framework, we have identified the need for a prior term in addition to the mismatch term in the objective function, and we have concluded that the weights in the mismatch function are given by the model and measurement errors. Determining which measurements that should be included in the mismatch remain undetermined. One might think that using all actual pressure measurements would be the correct thing to do. However, the errors, in particular the model errors, are highly correlated in time, and we have assumed uncorrelated measurements. Introducing the error covariance matrix, C, in the Gaussian error model:

$$p(\{M\},\{\lambda\}) \propto -\exp\left(\sum_{nm} \left(M_n - S_n(\{\lambda\})\right)\left(C^{-1}\right)_{nm}\left(M_m - S_m(\{\lambda\})\right)\right) \quad , \tag{12.31}$$

is sometimes proposed as a solution to this, but it is actually not a good idea. There are two main reasons for this: first, it is very difficult to obtain good estimates for the correlations, and second, the inverse of the covariance matrix is highly sensitive to small errors in the covariance estimates. The solution to the problem of correlations is to use as few measurements as possible. To obtain this, calculated quantities that are characteristic of the well test response, such as derivatives, should be used in the mismatch function instead of many direct pressure measurements.

The mismatch function should be defined using quantities that are characteristic of the well test response.

12.3 Interference testing

An interference test involves at least two wells. The pressure response from a rate change in one well is recorded in one or more non-producing wells. The main purpose of interference testing is to determine and quantify pressure communication. In some simple cases analytical models can be used for the analysis of these tests, and we have seen such an example in the section on non sealing faults (page 74), but in general numerical simulation is a necessary tool in the planning and analysis of interference tests. In this section we will give a brief presentation of two examples in order to illustrate this.

Fig. 12.4 shows two wells in a a fluvial reservoir. Optimal reser-

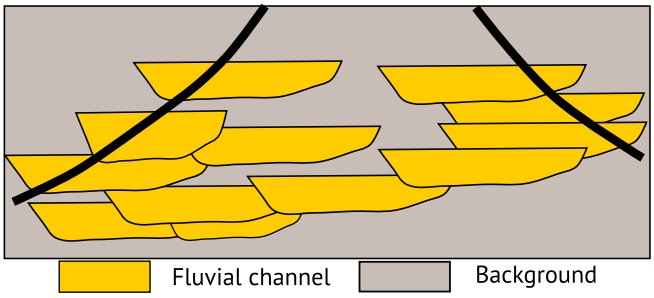


Figure 12.4: Interference testing wells for estimating sand body communication in a fluvial reservoir

voir steering, and the need for and placement of future in-fill wells, depend on the permeability distribution which is determined by the density of sand bodies and the sand body geometries. An interference test, using the two wells, would give valuable information relating to these parameters.

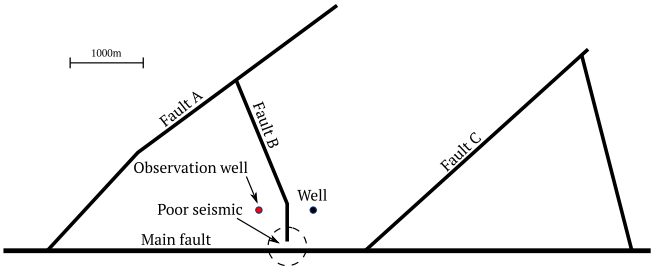


Figure 12.5: Interference testing wells for estimating fault patterns and fault communication

Fig. 12.5 shows two wells in different reservoir compartments. Due to the limited resolution of seismic, the location and extension of

faults is uncertain. When a fault with a small throw links up with a large fault, such as fault B is linked up with the main fault in Fig. 12.5, it is often difficult to determine whether it extends all the way to the large faults. It is also unknown to what extent the faults are sealing. Well tests in each of the two wells might give information relating to some of these parameters, while an interference test would give additional data. We will in the following discuss some simulated data that

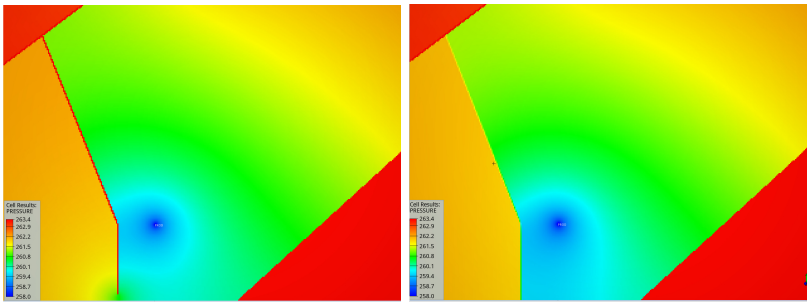


Figure 12.6: Pressure distribution in two alternative reservoirs; a reservoir with a fault that does not extend to the main bounding fault (left), and a reservoir where the same fault is not completely sealing (right).

illustrates the possible use of an interference test in this situation. Relating to Fault B, we are interested in discriminating three different cases; a completely sealing fault that links up with the main fault, a sealing fault that does not link up, and a incompletely sealing fault. In the first case, the observation well in isolated from the producer, so this situation will be easy to detect by a single pressure measurement, while we in the two other cases will get a time dependent response in both producer and observation well. The pressure distribution after prolonged production is shown in Fig. 12.6.

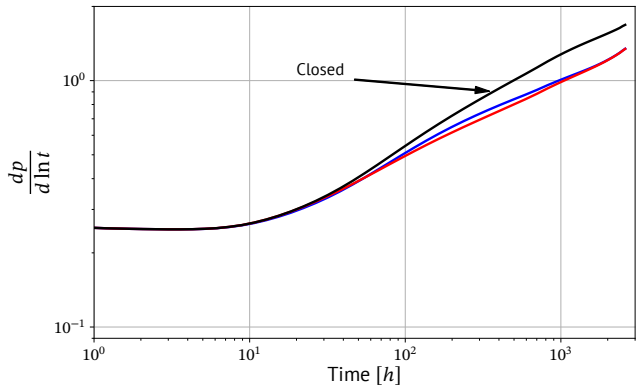


Figure 12.7: Log-derivative diagnostic plot for the drawdown test and different fault configurations. Sealing fault in black, non-sealing fault in blue, and unlinked faults in red.

As shown in Fig. 12.7, a well test might be able to differentiate between a completely sealing fault, and the two leaky-fault situations. A long test, about a month in the simulated 300 mD reservoir, is however needed, and the two other cases have an almost identical response. A log–derivative plot for the observation well response is shown in Fig. 12.8. We see that the late time response for the non-sealing-fault and unlinked-fault case is almost identical. As the pressure disturbance will have to travel a longer distance for the unlinked-fault case than in the non-sealing-fault case, the pressure signal will arrive later

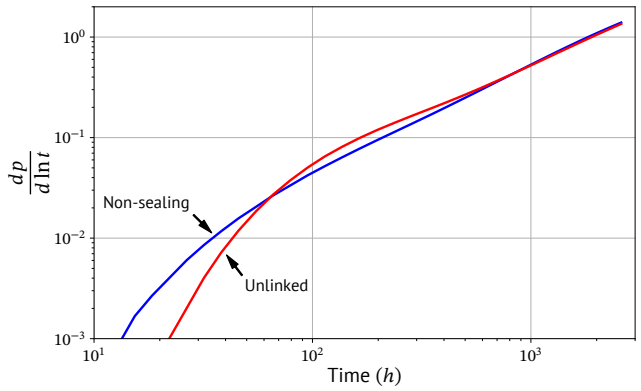


Figure 12.8: Log-derivative type plot for the observation well response and different fault configurations. Non-sealing fault in blue, and unlinked faults in red.

(a factor of two in arrival time). This difference enables the use of the observation well response to discriminate the two scenarios. In the simulated case, a test running over just a few days is sufficient for this. The strength of the signal is proportional to the rate, and the simulation results can also be used as a guide to what is a sufficient test rate in order to receive a detectable early response. The observation well response is also more sensitive to the fault seal parameters such as fault-zone permeability, and will provide more accurate estimates.

13
Deconvolution

The superposition principle was introduced in connection with the buildup test (page 39), and additional examples of application is the two-rate test (page 110) and the step-rate test (page 111). According to this principle, we can express the pressure response to any number of rate changes ΔQ_n occurring at times τ_n in terms of the response in a simple drawdown test $F(t)$:

$F(t)$ is often called the influence function.

$$p_0 - p_w(t) = \sum_n \Delta Q_n F(t - \tau_n) \quad . \tag{13.1}$$

We see that, if we approximate a continuous rate history with a number of equally spaced (Δt) step changes, and let $\Delta t \to 0$, Eq. (13.1) becomes

Convolution is the continuous version of superposition.

$$p_0 - p_w(t) = \int_0^t Q'(\tau) F(t - \tau)\, d\tau \quad . \tag{13.2}$$

This continuous version of superposition is called convolution. The inverse of convolution is deconvolution, which with reference to Eq. (13.2) means finding $F(t)$ from the known pressure and rate history $p_w(t)$ and $Q'(t)$.

Eq. (13.1) involves the derivative of the rates, and derivatives are noisy and inaccurate for any real data. By applying integration by parts and a change of variable we get an alternative form[1]

[1] In the integration by parts we have used that $Q(0) = 0$ and $F(0) = 0$.

$$p_0 - p_w(t) = \int_0^t Q(\tau) F'(t - \tau)\, d\tau = \int_0^t Q(t - \tau) G(\tau)\, d\tau \quad , \tag{13.3}$$

where $G(\tau) = F'(\tau)$.

In principle, by applying deconvolution, any rate and pressure history can be analyzed using the methods derived for the drawdown test. For instance, a well history with unstable rates or several short shut-downs, where the late time responses will be masked by short time fluctuations, can be analyzed for responses corresponding to the total producing time for the identification of reservoir boundaries. If we have complete data for all wells in a reservoir, the methodology may even be extended to finding the response for each well and each well–observation well pair. In practice the situation is not as simple, and deconvolution actually became a practical part of the well-test analysis toolbox as late as around 2010, and the development of robust deconvolution methods is still an active research topic. The

The deconvoluted pressure can be analyzed using the methods derived for the drawdown test.

Deconvolution in well testing is an ill-posed problem.

main hurdle is that the deconvolution problem, Eq. (13.3), is ill-posed in the sense that, without proper regularization, small errors in rate and pressure data give large errors in the estimates.

Note also that missing data, in particular in multi well situations, and changing reservoir properties, such as non-constant skin, will always limit the applicability of deconvolution.

Deconvolution assumes that the reservoir properties, including skin, are constant in time.

The actual implementation of deconvolution will vary between software packages, and we will not present any algorithm in detail. Algorithms and methods fall in two categories: deconvolution in the time domain, and deconvolution in Laplace space.

13.1 Spectral methods

Spectral methods are methods applied in Fourier (frequency) or Laplace space. It is well known[2] that a convolution integral in time transforms to a simple multiplication in these spaces, and that deconvolution thus amounts to division. In Laplace space, Eq. (13.3) becomes

$$\widetilde{\Delta p}(s) = s\widetilde{Q}(s)\widetilde{F}(s) \quad , \tag{13.4}$$

[2] See Eq. (15.9) in the mathematical notes for transformation to Laplace space.

where $\widetilde{F}(s)$ is the Laplace transform of G in Eq. (13.2), so that we have

$$\widetilde{F}(s) = \frac{\widetilde{\Delta p}(s)}{s\widetilde{Q}(s)} \quad . \tag{13.5}$$

In order to evaluate Eq. (13.5) we need to calculate the Laplace transform of the measured data. Measurements are only available for a finite time interval (t_0, T), while the transform is an integral over the full interval $(0, \infty)$. We can write the Laplace transform of sampled data, $\{f(t_n)\}$, as

$$I(s) = I_1(s) + I_2(s) + I_3(s) \quad , \tag{13.6}$$

where

$$\begin{aligned} I_1(s) &= \int_0^{t_0} e^{-st} f_0(t)\, dt \quad , \\ I_2(s) &= \sum_n \int_{t_{n-1}}^{t_n} e^{-st} f_n(t)\, dt \quad , \\ &\text{and} \\ I_3(s) &= \int_T^{\infty} e^{-st} f_\infty(t)\, dt \quad . \end{aligned} \tag{13.7}$$

For rates, f_0, can usually be treated as a step rate change, and $f_\infty(t)$ is a constant by definition, so that we have

$$I_1^Q(s) = \left(1 - e^{-st_0}\right) \frac{Q(t_0)}{s} \tag{13.8}$$

and

$$I_3^Q(s) = e^{-sT} \frac{Q(T)}{s} \quad . \tag{13.9}$$

If the first pressure measurement, $p_0 = p(t_0)$, is early enough so that the response is dominated by wellbore storage, the pressure in the

first integral I_1^p will be linear, $f_0^p(t) = \frac{p_0}{t_0} t$. By applying integration by parts, one can show that

$$I_1^p(s) = \int_0^{t_0} e^{-st} f_o^p(t)\, dt = \left(1 - (1 + st_0)\, e^{-st_0}\right) \frac{p_0}{s^2 t_0} \quad . \tag{13.10}$$

In the integrals over samples, I_2^Q and I_2^p, linear interpolations on log-log scale ($f_n(t) = a_n t^{\alpha_n}$) is in general preferred.[3] However, step changes in rates should be represented as such, and the corresponding interpolation of subsequent pressure responses may also be time shifted ($p(t) = a(t - t_s)^\alpha$, where t_s is the time of step rate change) to better reflect the time scale of the response. Numerically, smart reordering of terms in the summation in order to preserve sufficient accuracy is often also required.

[3] M. Onur and A. C. Reynolds. "Well Testing Applications of Numerical Laplace Transformation of Sampled-Data." In: *SPE Reservoir Evaluation & Engineering* 1.3 (June 1, 1998), pp. 268–277. DOI: 10.2118/36554-PA.

The main concern is the extrapolation of the pressure into the future, that is for $t > T$. A reasonably stable rate before the end of the test is preferred, in which case a linear extrapolation similar to slider analysis (see page 47) can be sufficient. Caution is advised, since in particular the late time behavior of the deconvoluted influence function often end up as a reproduction of the imposed extrapolation. In order to trust any results based on spectral deconvolution, it is required to investigate the sensitivity of results on the extrapolation.

The deconvoluted response can be analyzed in the time domain by numerically inverting the transformed response (Eq. (13.5)) using for instance the Stehfest algorithm (page 128). This inversion has its own intrinsic numerical issues that add to the uncertainty in the analysis, and it is thus often better to perform the analysis directly in Laplace space.[4] For instance can a log–log plot of $sF(s)$ vs. $1/s$ be used to identify flow regimes, and corresponding reservoir properties, in much the same way as the log–log derivative diagnostic plot (page 56). Note that, being an integral, the Laplace transformed response is smoother than the response in time, and the separation between flow regimes is less pronounced. This makes it more difficult to identify flow regimes, i.e. a larger separation (in time) is needed.

[4] M. Bourgeois and R. N. Horne. "Well Test Model Recognition Using LaPlace Space Type Curves." In: *SPE Formation Evaluation* 8.1 (Mar. 1, 1993), pp. 17–25. DOI: 10.2118/22682-PA.

13.2 Time domain methods

A major breakthrough was made in the development of time domain methods for deconvolution in the early 2000s when it was proposed that the problem could be cast in the form of a minimization problem.[5] A number of algorithms have subsequently been formulated based on this idea, and we will here only present the main philosophies behind these algorithms without going into any detail.

[5] T. von Schroeter, F. Hollaender, and A.C. Gringarten. "Deconvolution of Well Test Data as a Nonlinear Total Least Squares Problem." In: *SPE Journal* (Dec. 2004), pp. 375–390. DOI: 10.2118/77688-PA.

As we defined $G(\tau) = F'(\tau)$, Eq. 13.3 was written as

$$p_0 - p_w(t) = \int_0^t Q(t - \tau) G(\tau)\, d\tau \quad , \tag{13.11}$$

and the time domain methods solve for the pressure derivative $G(t)$. This is also the most interesting function for the analysis since the

log–log derivative diagnostic plot (page 56) is a plot of $-\frac{dp}{d\ln(t)}$ and we have

$$-\frac{dp}{d\ln(t)} = tG(t) \quad . \tag{13.12}$$

Since the functions $F(t)$ and $G(t)$ are multi scale, and typically vary on a logarithmic time scale, it is common to perform the substitutions $\sigma = \ln\tau$ and $Z(\sigma) = \ln(\tau G(\tau))$, which gives:

$$p_0 - p_w(t) = \int_{-\infty}^{\ln t} Q(t - e^{\sigma}) e^{Z(\sigma)}\, d\sigma \quad , \tag{13.13}$$

and solve for the function $Z(\sigma)$, which is directly related to the diagnostic plot. This also has the added bonus that $tG(t) = e^Z$ is guaranteed to be positive, but the flip side is that the substitution has transformed the linear relation between G and p into a non-linear relation between Z and p.

In order to solve Eq. (13.11) for G it must be discretized. Pressure is a measured quantity that is only available at discrete times $\{t_i\}$, and in general the right hand side is discretized by approximating $Q(t)$ and $G(t)$ in terms of a finite set of basis functions

$$Q(t) = \sum_n q_n \theta_n(t)\,, \text{ and } G(t) = \sum_m g_m \psi_m(t) \quad , \tag{13.14}$$

which gives

$$p_w(t_i) = p_0 - \sum_{mn} q_n g_m A_{nmi} \quad , \tag{13.15}$$

where

$$A_{nmi} = \int_0^{t_i} \theta_n(t_i - \tau)\psi_m(\tau)\, d\tau \quad . \tag{13.16}$$

For the rates, which is a measured quantity, it is natural to use either piecewise constant or interpolating functions as basis. For G, it is most common to use log-linear interpolation between equally spaced points on a logarithmic time scale, while Eq. (13.13) is already on a logarithmic time scale (σ) so linear interpolation[6] is used for Z. In general the basis function need not be local, however selecting basis functions that in some manner are related to an equal spacing on a logarithmic time scale seems to be a important. This may not be surprising, given the form of the infinite acting solution (Eq. (3.29)).

[6] Linear interpolation corresponds to local triangle shaped basis functions.

As mentioned earlier, deconvolution is an ill-posed problem and we have errors both in the measured rates and pressures. As a result the problem must be regularized. This can be done in three ways: Limiting the solution space spanned out by the basis functions $\{\psi_m\}$ so that the solutions is guaranteed to obey known properties, imposing prior beliefs regarding the solution[7] or imposing other restrictions typically relating to the smoothness of the solution.

[7] The Bayesian approach, that is the use of prior beliefs for regularization was discussed on page 131.

For simplicity we will first assume that we have no errors in the rate data. Without regularization the problem is then simply reduced to finding the solution that minimize the difference between the right-hand and left-hand side of Eq. (13.15)

$$E_p(p_0, \{g_m\}) = \frac{1}{N_i}\sum_i \left(p_w(t_i) - p_0 + \sum_{mn} q_n g_m A_{nmi} \right)^2 \quad . \tag{13.17}$$

Without imposing strong restrictions on the solution, this problem is ill-posed, so we must add an extra regularization term $\Omega(\{g_m\})$ to the function that is to be minimized:

$$\min_{p_0,\{g_m\}} \left[E_p(p_0,\{g_m\}) + \alpha\Omega(\{g_m\})\right] \quad . \tag{13.18}$$

A regularization term that limits the second derivative of Z has proven to be a good choice (see Eq. (13.13)):

$$\Omega \propto \int_{-\infty}^{\ln T} \left[Z''(\sigma)\right]^2 \, d\sigma \quad . \tag{13.19}$$

When using the quotient rule and solving for G directly, Eq. (13.19) becomes

$$\Omega \propto \int_0^T \left[\frac{G''(\tau)\tau^2}{G(\tau)} + \frac{G'(\tau)\tau}{G(\tau)} - \left(\frac{G'(\tau)\tau}{G(\tau)}\right)^2\right]^2 \frac{d\tau}{\tau} \quad . \tag{13.20}$$

With a regularization term similar to Eq. (13.19), which falls in the class of Tikhonov regularization, the minimization problem Eq. (13.18) would be of the linear least square type which can be directly solved by standard methods. This form does however not seem to sufficiently restrict on the solution space, and with the form Eq. (13.20) the problem is of the non-linear least square type.

We know that the influence function F will be dominated by the wellbore storage effect (see page 36) for short times, thus the basis functions should be selected such that F is linear for short times. Additional regularization can be obtained by judiciously selecting basis functions ψ_m such that $G(t)$ satisfies at least some of the following known requirerments

$$\begin{aligned} G(t) &> 0 \\ G'(t) &< 0 \\ G''(t) &> 0 \\ &\vdots \end{aligned} \tag{13.21}$$

which holds under quite general conditions.[8] As an example,[9] with exponential basis functions $\psi_m(t) = e^{-\lambda_m t}$, the requirements in Eq. (13.21) are met for all orders of the derivative provided that all $g_m > 0$.

In reality we always have errors in the rate data, so that we need to solve for $\{q_n\}$ in addition to $\{g_m\}$ in Eq. (13.15). The corresponding regression problem is known as a "Total Least Squares" or "Errors In Variables" problem. One way of attacking this problem is to include the rates in the set of unknowns and add a term

$$E_q(\{q_n\}) = \frac{1}{N_j}\sum_j \left(Q(t_j) - \sum_n q_n \theta_n(t_j)\right)^2 \tag{13.22}$$

to the function that is to be minimized:

$$\min_{p_0,\{g_m\},\{q_n\}} \left[E_p(p_0,\{g_m\},\{q_n\}) + \beta E_q(\{q_n\}) + \alpha\Omega(\{g_m\})\right] \quad . \tag{13.23}$$

[8] K. H. Coats et al. "Determination of Aquifer Influence Functions From Field Data." In: *Journal of Petroleum Technology* 16.12 (Dec. 1, 1964), 1 417–1 424. DOI: 10.2118/897-PA.

[9] Georgy G. Skorik, Vladimir V. Vasin, and Fikri Kuchuk. "A new technique for solving pressure–rate deconvolution problem in pressure transient testing." In: *J Eng Math* 101.1 (Dec. 1, 2016), pp. 189–200. DOI: 10.1007/s10665-016-9854-x.

The relative weight put on each of the tree terms in Eq. (13.23) is to a certain extent arbitrary. In a Bayesian context (see page 131) it is however natural to choose

$$\beta = \frac{\sigma_p^2}{\sigma_q^2} \quad , \tag{13.24}$$

where σ_p and σ_q are the standard errors in pressure and rate measurements. The regularization parameter α should be selected to give the best balance between a good fit to data and a regular (smooth) function. An "L-curve" plot, which is α-parameterized log–log plot of $\Xi = E_p + \beta E_q$ vs. Ω (see Fig. 13.1), can be a used as a tool.

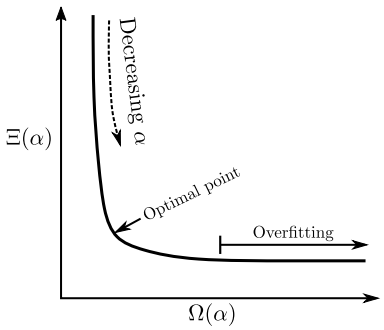


Figure 13.1: The principle behind the L-cuve plot.

14
The role of well testing in reservoir characterization

The title of the course for which these lecture notes have been written contains the phrase: "Reservoir Property Determination by Well Testing". We have seen that well testing is used in many additional contexts, such as reservoir monitoring and well productivity monitoring, but these additional contexts have been touched only briefly. So, what is the role of well testing in property determination, and which properties are measured for what purpose? In this chapter we will try to place well testing in the broader context of reservoir characterization and reservoir modelling.

The simplistic perspective is that well testing gives us reservoir permeability, distance to faults, fault communication, and reservoir volume. A broader perspective is that well testing provides data for reservoir characterization. Reservoir characterization is a multidisciplinary task coordinated by "geo-engineers", that is people with a broad knowledge of reservoir geology and reservoir engineering. The purpose of reservoir characterization is twofold: to provide qualitative data to improve the understanding of the reservoir, and quantitative data in order to model the reservoir. Reservoir models play a major role in current development planning and reservoir management practices.

Reservoir characterization has two levels; the conceptual model, which may include a number of alternative scenarios, and parameterized models, or property models. Reservoir parameters (properties) have no meaning outside an associated conceptual model. A conceptual model is a clearly defined concept of the subsurface in the sense that a geo-scientist could represent it as simple sketches. Scenarios are a set of reasonably plausible conceptual models.

14.1 Scenarios

Scenarios are not incrementally different models based on changes in input data or parameter values, scenarios are a set of reasonably plausible conceptual models. Scenario uncertainty is the main contributor to sub-surface uncertainty in early phase field development, and often remain highly important even after many years of production.

Scenarios are a set of reasonably plausible conceptual models

In order to take into account the uncertainty in a reservoir response, such as the production in a given year, here represented by ω, we represent the response as a probability distribution $p(\omega)$. The probability can be expressed as

$$p(\omega) = \sum_S P(S) p_S(\omega) \tag{14.1}$$

where $P(S)$ is the probability of a scenario member S, and $p_S(\omega)$ is the probability of a a certain response (ω) in scenario S. Well testing can supply data that contribute to falsify a conceptual model, or change the probability associated with (plausibility of) each scenario member.

Well testing can reduce scenario uncertainty.

In exploration, field development planning, and early phase production, when scenario uncertainty is the dominant uncertainty, it is important to obtain overview and understand the full set of possible geological concepts; the scenarios. One should therefore plan for well tests and well placements that can contribute to the reduction of scenario uncertainty. Below we will present two examples of scenario uncertainty. These examples, which are based on real field cases, are not worked out in much detail, and it is up to the reader to apply the knowledge of well testing obtained in previous chapters in order to evaluate to what extent a well test will contribute to reducing the uncertainty.

The first example is a reservoir delineated by two large faults, as shown in Fig. 14.1. The structural interpretation is uncertain, and a

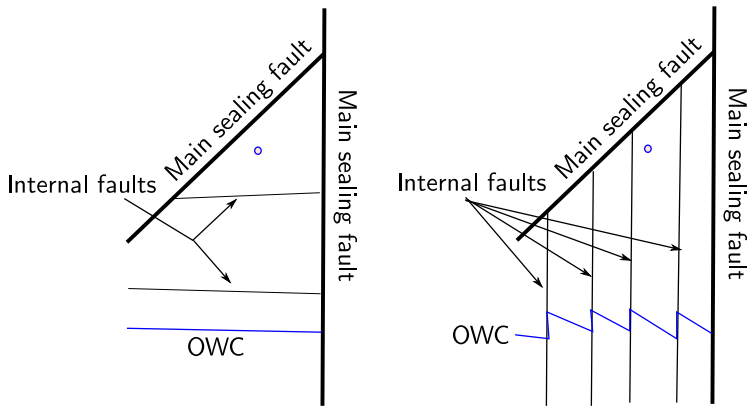


Figure 14.1: Alternative structural conceptual models based on poor seismic.

noisy seismic may be interpreted based on two competing concepts: A few internal faults in the east–west direction, or heavy internal faulting parallel to the eastern main faults. Optimal well placement in a water injection scheme will be very different for the two alternatives.

The second example relates to two different concepts on how the reservoir material has been deposited. The two concepts are illustrated in Fig. 14.2. The first concept implies that the reservoir is deposited in two isolated zones, and that the upper zone pinches out to the west. In the second conceptual model, the boundary layer is heavily eroded so that the two zones are communicating, and the western part of the upper zone is deposited as a thin layer reaching west-

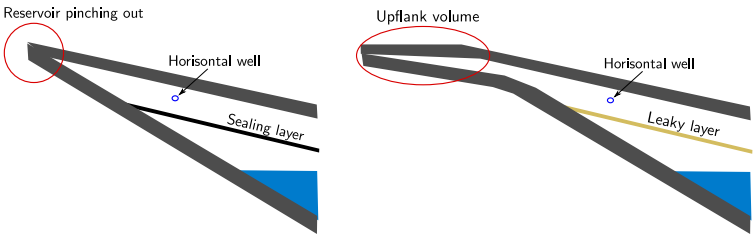


Figure 14.2: Alternative concepts of reservoir pinch-out and vertical communication.

wards. Note that, as far as modelling for well test interpretation or reservoir simulation is concerned, the two concepts can be spanned out in a single model with continuous variables (extent of up-flank volume and sealing capacity of inter-zonal layer). They do, however, represent two different geological concepts, and the concept selection will also possibly influence other aspects of the modelling. This illustrates that the distinction between scenario uncertainty, and uncertainty described by parameter variation is sometimes not clear cut in practice.

14.2 Model elements

A given conceptual model contains model elements. Model elements are rock bodies which are petrophysically and/or geometrically distinct in the context of reservoir fluid flow, and are the building blocks of reservoir models, both conceptually and as realized in a computer. Model elements have properties, i.e. they can be described with a set of parameters. These parameters are geometric properties, such as length, height, direction, and thickness, and volumetric properties (property fields), such as porosity, permeability, clay content, and facies fractions, The property fields of different model elements are associated with a homogeneity scale or representative elementary volume (REV).

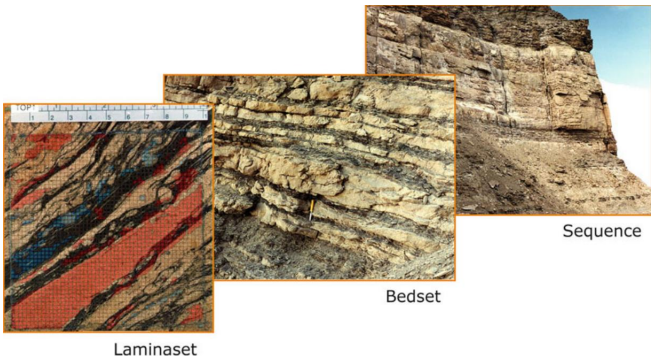


Figure 14.3: Example of geological features represented by model elements at different scales

In general the model elements form a hierarchy, where large scale elements consist of elements at smaller scales (see Fig. 14.3). The property fields of large scale elements are effective properties which represent some form of averaging of the property fields of the constitutive elements. For permeability, which is a tensor field, this aver-

Large scale property fields, such as permeability, are effective properties

aging is non-trivial.

Well testing can provide data related to geometric properties of structural elements, but in terms of property fields a well test can only see permeability and porosity. Since, as described above, permeability is a scale dependent property associated with representative elementary volumes at certain homogeneity scales, the question of *which permeability* the well test is probing has to be answered. In general, the early time data see small-scale properties (and short time scales), while the late time data see large scale properties (and longer time scales). Additionally, in particular important for the short time data, there is always some along-wellbore "averaging" involved. In any case, well testing is the only measurements that measure permeability at real reservoir conditions at scales directly relevant for reservoir simulation.

14.3 Measurements

The main data sources for reservoir characterization are seismic, outcrops and analogues, reservoir cores, well logs, well tests, and production data. All measurements, including well testing results, must be interpreted in the context of the model elements of a relevant conceptual model, and a well test interpretation must be consistent with other relevant data. Each measurement is associated with a measurement scale, or probed volume, and thus measure properties of model elements on different levels of the model-element hierarchy. Note that, since, additionally, the measurement scale associated with a given measurement often do not correspond to any of the homogeneity scales of the model elements we need to characterize, data consistency and consistent data integration is in general non trivial and involve both up- and down-scaling.

Data integration and data consistency involve up- and down-scaling.

14.4 Final words

Well testing does not live in isolation, and a well test must be planned and interpreted in the context of conceptual geological models and their model elements. A key to successful reservoir characterization is that everyone work with shared scenarios in a collective effort, and a planned well test should be performed in order to answer specific predefined questions. Remember also that scenario uncertainty is often the dominant uncertainty. We should always ask ourselves and our colleagues: Have we included all plausible conceptual models?

15
Mathematical notes

The notation that are used in these lecture notes may be unfamiliar to some. The coordinate free notation that is used is more common in physics texts than in engineering books. However, I am convinced that once the basics of the notation is mastered, equations are much easier to read and understand. Darcys law is for instance written as

$$q = -\frac{1}{\mu} K \cdot \nabla p$$

in coordinate free notation, instead of

$$q_i = -\frac{1}{\mu} \sum_{j=1}^{3} K_{ij} \frac{\partial}{\partial x_j} p$$

in the normal engineering type notation.

15.1 Scalars, vectors, and tensors

The fundamental objects in any continium theory, including fluid flow in porous media, are scalar-fields, vector-fields, and tensor-fields. This text folllows the common lazy tradition of using the terms scalar, vector, and tensor for these fields.

All readers should be familiar with the concepts of scalars and vectors, while tensors may be a less familiar object. In the context of the present text, only tensors of order 2 is encountered[1], and the most prominent is the permeability, K. Permeability is a linear operator that operates on a gradient (derivative of pressure) to produce a vector (volumetric flux). Such operators are called (2,0) tensors, or more simply tensors of order 2. The tensor concept can be viewed as a generalization of a vector, and taking the so called tensor product of two vectors create a tensor of order 2 (see Table 15.1).

No special notation is used in order to distiguish between scalars, vecrtors, and tensors. However, lower case letters are typically used for scalars and vectors, and upper case letters for tensors.

Scalars, vectors and tensors can be multipled, either using the dot product or the tensor product as shown in Table 15.1.

[1] The term tensor is usually not used for scalars and vectors, but scalars can be viewed as tensors of order 0 and vectors as tensors of order 1.

Coordinate free notation	Index notation
$v = au$	$v_i = au_i$
$a = u \cdot v$	$a = \sum_i u_i v_i$
$v = K \cdot u$	$v_i = \sum_i K_{ij} u_j$
$v = u \cdot K$	$v_j = \sum_i u_i K_{ij}$
$K = L \cdot M$	$K_{ij} = \sum_n L_{in} M_{nj}$
$K = uv$	$K_{ij} = u_i v_j$

Table 15.1: Multiplication of tensors. a is a scalar, u and v are vectors and K, L, and M are tensors.

15.2 Spatial derivatives and the gradient operator

The operator for spatial derivatives is the nabla, or gradient, operator, ∇. In terms of notation, ∇ behaves like a vector, but it must be remembered that ∇ operates on (takes the derivative of) the expression to the right. Some examples of expressions involving the nabla operator can be found in Table 15.2. The shorthand notation ∇^2 is used for the second derivative operator $\nabla \cdot \nabla$ (the Laplace operator). The derivation takes presedence over multiplication. Paranthesis are used to group.

Coordinate free notation	Index notation
∇	$\frac{\partial}{\partial x_i}$
$\nabla^2 = \nabla \cdot \nabla$	$\frac{\partial^2}{\partial x_i^2}$
$\nabla\nabla$	$\frac{\partial^2}{\partial x_i \partial x_j}$
$v = \nabla a$	$v_i = \frac{\partial}{\partial x_i} a$
$a = \nabla \cdot v$	$a = \sum_i \frac{\partial}{\partial x_i} a_i$
$K = \nabla\nabla a$	$k_{ij} = \frac{\partial^2}{\partial x_i \partial x_j} a$
$b = \nabla^2 a$	$b = \frac{\partial^2}{\partial x_i^2} a$
$c = \nabla a \cdot K \cdot \nabla b$	$c = \sum_{ij} \frac{\partial a}{\partial x_i} K_{ij} \frac{\partial b}{\partial x_j}$
$c = \nabla \cdot (aK \cdot \nabla b)$	$c = \sum_{ij} \frac{\partial}{\partial x_i} \left(aK_{ij} \frac{\partial b}{\partial x_j} \right)$

Table 15.2: Examples of expressions involving the ∇ operator. a, b, and c are a scalars, u and v are vectors and K is a tensor.

We see in particular that the divergence of a vector field $q = (q_x, q_y, q_z)$ is a scalar given by the dot product $\nabla \cdot q = \frac{\partial q_x}{\partial x} + \frac{\partial q_y}{\partial y} + \frac{\partial q_z}{\partial z}$, that the gradient of a scalar field p is a vector field $\nabla p = \left(\frac{\partial p}{\partial x}, \frac{\partial p}{\partial y}, \frac{\partial p}{\partial z} \right)$, and that the Laplace operator ∇^2 sends a scalar to a scalar.

15.3 The Gauss theorem, and the continuity equation

Gauss divergence theorem.

The Gauss divergence theorem:

$$\int \nabla \cdot v \, dV = \int v \cdot dS \quad . \tag{15.1}$$

v is a vector, the left integral is over a volume, and the right integral is over the enclosing surface. Note that dS is an outward pointing *vector*

normal to the surface element.

The continuity equation for some entity involves three quantities:

- ρ: Density, that is the amount per volume.
- j: Flux, that is the amount that flows per area and time (a vector).
- σ: The amount that is created per volume and time.

Continuity equation on integral form.

For any given volume we then have

$$\frac{\partial}{\partial t}\int \rho\, dV = \int \sigma\, dV - \int j \cdot dS \tag{15.2}$$

This is the continuity equation on integral form. Numerical simulation often employ control volume discretisation, and Eq. (15.2) is then applied to the each control volume or grid-block.

If we apply the Gauss theorem to the surface integral in eq. 15.2 we get

$$\frac{\partial}{\partial t}\int \rho\, dV = \int \sigma\, dV - \int \nabla \cdot j\, dV \quad , \tag{15.3}$$

Continuity equation on differential form.

and if we let the volume be an infinitely small differential element, Eq. (15.3) gives

$$\frac{\partial}{\partial t}\rho + \nabla \cdot j = \sigma \quad , \tag{15.4}$$

which is the continuity equation on differential form.

15.4 Laplace transform

The Laplace transform $\mathscr{L} : f \to \widetilde{f}$ is an integral transform, and it is usually applied as a transform in time:

$$\widetilde{f}(s) = \int_0^\infty f(t)e^{-st}\, dt \quad . \tag{15.5}$$

The Laplace transform is a linear operator:

$$\begin{aligned} \mathscr{L}(f+g) &= \mathscr{L}f + \mathscr{L}g = \widetilde{f} + \widetilde{g} \\ \mathscr{L}(cf) &= c\mathscr{L}f = c\widetilde{f} \quad . \end{aligned} \tag{15.6}$$

Calculating the integral, we observe that the Laplace transform of unity and of t are

$$\begin{aligned} \mathscr{L}(1) &= \int_0^\infty e^{-st}\, dt = \left[-\frac{1}{s}e^{-st}\right]_0^\infty = \frac{1}{s} \\ \mathscr{L}(t) &= \int_0^\infty te^{-st}\, dt = \left[-\frac{t}{s}e^{-st}\right]_0^\infty - \int_0^\infty -\frac{1}{s}e^{-st}\, dt = \frac{1}{s}\mathscr{L}(1) = \frac{1}{s^2} \quad , \end{aligned} \tag{15.7}$$

where we are applying integration by parts when solving the transform in time t. We observe that time t and the variable s has an inverse correspondence, hence late times t corresponds to small s.

The transformation of the partial derivatives are

$$\mathscr{L}\left(\frac{\partial f}{\partial x}\right) = \int_0^\infty \frac{\partial f}{\partial x} e^{-st}\, dt = \frac{d\widetilde{f}}{dx}$$
$$\mathscr{L}\left(\frac{\partial f}{\partial t}\right) = \int_0^\infty \frac{\partial f}{\partial t} e^{-st}\, dt = s\widetilde{f}(x,s) - f(x,0) \quad , \tag{15.8}$$

where we use the basic rule $\int \frac{\partial}{\partial x} f(x,y)dy = \frac{\partial}{\partial x} \int f(x,y)dy$ for the first equality and integration by parts for the second equality.

The transformation of a convolution integral is a product:

$$\mathscr{L}\left(\int_0^t f(t-\tau)g(\tau)\, d\tau\right) = \widetilde{f}(s) \cdot \widetilde{g}(s) \quad . \tag{15.9}$$

This can be shown as follows:

$$\begin{gathered}
\int_0^\infty dt \int_0^t d\tau\, e^{-st} f(t-\tau)g(\tau) = \\
\int_{-\infty}^\infty dt \int_{-\infty}^\infty d\tau\, e^{-st} f(t-\tau)g(\tau) = \\
\int_{-\infty}^\infty dt' \int_{-\infty}^\infty d\tau\, e^{-st'} e^{-s\tau} f(t')g(\tau) = \\
\left(\int_0^\infty e^{-st'} f(t')dt'\right)\left(\int_0^\infty e^{-s\tau} g(\tau)d\tau\right)
\end{gathered} \quad . \tag{15.10}$$

The first and third equality follows from the fact that the functions $f(t)$ and $g(t)$ are zero for negative t.

Relevant literature

The following books are highly relevant for the course “Reservoir Property Determination by Core Analysis and Well Testing”.

- George Stewart. *Well test design and analysis*. PennWell Books, 2011. ISBN: 9781593702311
- T.A. Jelmert. *Introductory well testing*. bookboon, 2013. ISBN: 978-87-403-0445-9. URL: http://bookboon.com/en/introductory-well-testing-ebook
- R.W. Zimmerman. *Fluid Flow in Porous Media*. The Imperial College lectures in petroleum engineering. World Scientific Publishing Company Pte Limited, 2018. ISBN: 9781786344991. DOI: 10.1142/q0146
- John P. Spivey and W. John Lee. *Applied Well Test Interpretation*. Society of Petroleum Engineers, 2013. ISBN: 978-1-61399-307-1
- Roland N. Horne. *Modern Well Test Analysis: A Computer-Aided Approach*. Petroway, 1995. ISBN: 978-0962699214

Other material

The following posters from Fekete Associates can serve as “cheat sheets”.

- Fekete poster: Well testing fundamentals (http://www.fekete.ca/SiteCollectionDocuments/Posters/Fekete_WellTest_Fundamentals_5731_0614AA_LOW.png)
- Fekete poster: Well testing applications (http://www.fekete.ca/SiteCollectionDocuments/Posters/Fekete_WellTestApplications_5731_0614AA_LOW.png)

Nomenclature

α	shape factor (fracture systems)
Δp_{ex}	effective pressure difference (by desuperposition)
r_D	dimensionless radius, $r_D = r/r_w$
r_{Do}	dimensionless distance to the outer boundary
η	(hydraulic) diffusivity, $\eta = \frac{k}{\mu\phi c_t}$, SI derived unit: $\mathrm{m^2/s}$
γ	Euler(–Mascheroni) constant, 0.5772 …
λ	inter-porosity flow parameter (dual porosity)
μ	viscosity, SI derived unit: $\mathrm{Pa\,s} = \mathrm{kg/(m\,s)}$
μ_t	effective viscosity (multiphase flow)
ω	storativity ratio (dual porosity)
$\overline{p}$	average reservoir pressure
ϕ	porosity
ϕ_{fb}	bulk fracture porosity
ϕ_{mb}	bulk matrix porosity
ψ	pseudo-pressure (gas or multiphase reservoirs)
ρ	fluid density
σ	matrix–fracture coupling
σ	pseudoskin
σ_{mf}	volume of liquid flowing from matrix to fracture per time and bulk volume
A	(reservoir) area
B	formation volume factor
c	compressibility, SI derived unit: 1/Pa
c_ϕ	formation compressibility, SI derived unit: 1/Pa
C_A	Dietz shape factor
c_l	liquid compressibility
C_s	wellbore storage constant
c_t	Total compressibility

c_{tf} total compressibility of fracture

c_{tm} total compressibility of matrix (in a fracture system)

F influence function (reservoir response to a constant rate drawdown test)

G derivative of influence function (reservoir response to a constant rate drawdown test), $G(\tau) = F'(\tau)$

h perforation (reservoir) height

k permeability, SI derived unit: m^2

k_f fault zone permeability

k_f fracture permeability

k_m permeability of matrix (in a fracture system)

k_o oil permeability at S_{wi}

k_{fb} bulk permeability of the fracture system

k_{mb} volume weighted matrix permeability, $k_{mb} = \frac{V_m}{V_m+V_f} k_m$

k_{ro} relative oil permeability

L_f fault zone thickness

l_W length of horizontal well

p pressure, SI derived unit: $\mathrm{Pa} = \mathrm{kg/(m\,s^2)}$

p' logarithmic derivative $\frac{dp}{d\ln(t)}$

p_c characteristic pressure, $p_c = \frac{Q\mu}{2\pi kh}$

p_D dimensionless pressure

p_f fracture pressure

p_i initial pressure

p_m matrix pressure

p_w well pressure (bottom-hole pressure)

Q down hole (reservoir) well production rate

q volumetric fluid flux (Darcy velocity)

Q_s surface well production rate

r radius

r_e equivalent radius ($p(r_e) = \overline{p}$)

r_o outer reservoir radius

r_p radius of pressure front

r_w wellbore radius

r_{inv} radius of investigation

r_{we} equivalent (effective) wellbore radius

S skin factor, dimensionless

S_{wi} irreducible water saturation

t_a pseudo time (gas or multiphase reservoirs)

t_D dimensionless time

t_e effective time (Agarwal time)

t_p production time

V volume

V_f volume of fracture

V_l liquid volume

V_m volume of matrix

v_p speed of pressure front

V_w total wellbore volume

W channel width

w_f fracture width

x_f fracture half length

m mass

Subscripts

D dimensionless form

h horizontal

i initial

i irreducible

l liquid

o oil

o outer

r relative

v vertical

w water

w well

References

This is a list of papers that are mentioned in the main text.

Articles have only been cited whenever a method or equation has been presented without proper derivation. The articles are cited so that interested readers can find a proper derivation. The selected articles are not necessarily the ones with the earliest derivation, as clarity in presentation has also been a criterion.

— ✻ —

Agarwal R. G. Al-Hussainy, R. and H. J Ramey. "An Investigation of Wellbore Storage and Skin in Unsteady Liquid Flow - I. Analytical Treatment." In: *SPE Journal* 10.3 (Sept. 1970), pp. 279–290. DOI: 10.2118/2466-PA.

Bourgeois, M. and R. N. Horne. "Well Test Model Recognition Using LaPlace Space Type Curves." In: *SPE Formation Evaluation* 8.1 (Mar. 1, 1993), pp. 17–25. DOI: 10.2118/22682-PA.

Cinco-Ley, H. and Samaniego-V. F. "Transient Pressure Analysis for Fractured Wells." In: *Journal of Petroleum Technology* (Sept. 1981), pp. 1749–1766. DOI: 10.2118/7490-PA.

Coats, K. H. et al. "Determination of Aquifer Influence Functions From Field Data." In: *Journal of Petroleum Technology* 16.12 (Dec. 1, 1964), 1 417–1 424. DOI: 10.2118/897-PA.

Everdingen, A. F. Van and W. Hurst. "The Application of the Laplace Transformation to Flow Problems in Reservoirs." In: *Petroleum Transactions, AIME* (Dec. 1949), pp. 305–324. DOI: 10.2118/949305-G.

Gringarten, Alain C. "Interpretation of Tests in Fissured and Multilayered Reservoirs With Double-Porosity Behavior: Theory and Practice." In: *Journal of Petroleum Technology* (Apr. 1984), pp. 549–564. DOI: 10.2118/10044-PA.

Hantush, M. S. and C. E. Jacob. "Non-steady green's functions for an infinite strip of leaky aquifer." In: *Eos, Transactions American Geophysical Union* 36.1 (1955), pp. 101–112. DOI: 10.1029/TR036i001p00101.

Hantush, Madhi S. "Hydraulics of wells." In: *Advances in hydroscience* 1 (1964), pp. 281–432.

Jones, J.R. and R. Raghavan. "Interpretation of Flowing Well Response in Gas-Condensate Wells." In: *SPE Formation Evaluation* (Sept. 1988), pp. 578–594. DOI: 10.2118/14204-PA.

Onur, M. and A. C. Reynolds. "Well Testing Applications of Numerical Laplace Transformation of Sampled-Data." In: *SPE Reservoir Evaluation & Engineering* 1.3 (June 1, 1998), pp. 268–277. DOI: 10.2118/36554-PA.

Peaceman, D. W. "Interpretation of Well-Block Pressures in Numerical Reservoir Simulation." In: *Society of Petroleum Engineers Journal* 18.03 (June 1978), pp. 183–194. DOI: 10.2118/6893-PA.

Schroeter, T. von, F. Hollaender, and A.C. Gringarten. "Deconvolution of Well Test Data as a Nonlinear Total Least Squares Problem." In: *SPE Journal* (Dec. 2004), pp. 375–390. DOI: 10.2118/77688-PA.

Skorik, Georgy G., Vladimir V. Vasin, and Fikri Kuchuk. "A new technique for solving pressure–rate deconvolution problem in pressure transient testing." In: *J Eng Math* 101.1 (Dec. 1, 2016), pp. 189–200. DOI: 10.1007/s10665-016-9854-x.

Valkó, P.P. and J. Abate. "Comparison of Sequence Accelrators for the Gaver Method of Numerical Laplace Transform Inversion." In: *Computers and Mathematics with Applications* 48 (2004), pp. 629–636. DOI: 10.1016/j.camwa.2002.10.017.

Yaxley, L.M. “Effect of a Partially Communicating fault on Transient Pressure Behavior.” In: *SPE Formation Evaluation* (Dec. 1987), pp. 590–598. DOI: 10.2118/14311-PA.